EXPERIMENTAL INVESTIGATION OF CAVITY INDUCED TWO PHASE FLOW IN SILICON MICROCHANNELS

Except where reference is made to the work of others, the work described in this thesis is my own or was done in collaboration with my advisory committee. This thesis does not include proprietary or classified information.

Daniel Thomas Pate

Certificate of Approval:

Daniel Mackowski
Associate Professor
Mechanical Engineering

Sushil H. Bhavnani, Chair
Professor
Mechanical Engineering

Roy W. Knight
Assistant Professor
Mechanical Engineering

Stephen L. McFarland
Dean
Graduate School

EXPERIMENTAL INVESTIGATION OF CAVITY INDUCED TWO PHASE FLOW IN SILICON MICROCHANNELS

Daniel Thomas Pate

A Thesis
Submitted to
the Graduate Faculty of
Auburn University
in Partial Fulfillment of
the Requirements for the
Degree of
Master of Science

Auburn, Alabama
December 15, 2006

EXPERIMENTAL INVESTIGATION OF CAVITY INDUCED TWO PHASE FLOW IN SILICON MICROCHANNELS

Daniel Thomas Pate

Signature of Author

Date of Graduation

VITA

Daniel Pate, son of Joey and Elsie Pate, was born on July 31, 1980, in Brewton, Alabama. He obtained his Bachelor of Science in Mechanical Engineering at Auburn University, Auburn, Alabama, in December 2003. He then entered the Graduate School of Auburn University in January 2004 to pursue a Masters in Mechanical Engineering.

THESIS ABSTRACT

EXPERIMENTAL INVESTIGATION OF CAVITY INDUCED TWO PHASE FLOW IN SILICON MICROCHANNELS

Daniel Thomas Pate

Master of Science, December 15, 2006
(B.S.M.E., Auburn University, 2003)

188 Typed Pages

Directed by Sushil H. Bhavnani

Modern developments in microelectronics manufacturing and architecture continue to lead to reductions in feature sizes on microprocessor chips. The demand for faster and more powerful systems has approached the limits of conventional passive and active electronics cooling schemes. Future high-powered electronics require new and innovative heat removal methods. The research study presented in this thesis is conducted in order to better understand two-phase heat transfer in a microchannel heat sink using FC-72 as the test fluid.

This study will cover the design, fabrication and testing of several silicon microchannel test sections. The test section consists of an (1cm x 1cm) array of nineteen parallel microchannels etched into silicon with the following hydraulic diameters: 253 and 356μm. The base of each channel contains two arrangements of re-entrant type cavities spaced evenly along the length. One arrangement has been fabricated with 2 cavities per channel and the other with 6 cavities per channel. Each cavity, measuring 20 microns in mouth size, is used to promote controlled nucleation activity in the base of the channels.

The experimental results presented include the bulk fluid temperature and pressure at the inlet and outlet, axial in-channel temperature measurements, and flow visualization taken through high-speed imaging. The results also include the comparison of several existing heat transfer correlations with the current studies data and evaluation of transient two-phase instabilities. It was found that the two-phase heat transfer coefficients reaching values of 10,000 W/m^2-k, that were calculated in this study, agreed well with macrochannel scale heat transfer correlations. Cavities were used to successfully eliminate instabilities during saturated exit conditions. Also the dominant frequencies of the two-phase instabilities were found to range from 8-14 Hz causing the in-channel temperatures to fluctuate as much as 4^oC.

ACKNOWLEDGEMENTS

The author would like to express his sincere thanks to Dr. Sushil Bhavnani, Dr. Roy W. Knight and Dr. Daniel Mackowski for serving on the comity for this study and their guidance throughout. The equipment and supplies provided by the Alabama Microelectronics Science and Technology Center is greatly appreciated. This study could not have been conducted without the guidance and aid of Charles Ellis. To my colleague Rory Jones, a special thanks is given for his contribution to this study. Thanks are also extended to Dr. Thomas Burch and Hugh Fellows for their help and moral support. The author would like to extend a personal thank you to his parents Joey and Elsie Pate, his brother Bryan Pate, his sister Amy Gibbins, his best friend Donnie Beckham and his fiancé Michelle for their belief and encouragement.

Style manual or journal used: American Society of Mechanical Engineers, Journal of Heat Transfer

Computer Software used: MS Office XP, Matlab 7.0.4, Solid Edge

TABLE OF CONTENTS

LIST OF TABLES

LIST OF FIGURES

NOMENCLATURE

A_{array}	Channel array base area, (m^2)
A_{cb-sb}	Channel base area for subcooled region, (m^2)
A_{fb-sb}	Fin base area for subcooled region, (m^2)
b_c	Y-intercept for T_h=f(R_h) calibration
b_l	Y-intercept for q_{loss}=f(T_h-T_{amb})
Bo	Boiling number
C_p	Specific heat, (J/kg-K)
Co	Convection number or the modified Martinelli parameter
D_h	Hydraulic diameter (m)
F_{fl}	Fluid dependent coefficient proposed by Kandlikar
G	Mass flux, (kg/m^2-s)
H_c	Channel height, (m)
h_{avg}	Average heat transfer coefficient for the entire channel, (W/m^2-K)
h_{fg}	Heat of vaporization, (J/kg)
h_{sb}	Average heat transfer coefficient for the sub-cooled region, (W/m^2-K)
h_{sp-FD}	Single phase fully developed heat transfer coefficient (W/m^2-K)
h_{tp}	Average heat transfer coefficient for the saturated region, (W/m^2-K)
h_{tp-cbd}	Convective boiling dominated heat transfer coefficient (W/m^2-K)
h_{tp-nbd}	Nucleate boiling dominated heat transfer coefficient (W/m^2-K)

I	Current supplied to the heaters, (Amp)
k_f	Thermal conductivity of the fluid, (W/m-K)
k_p	Thermal conductivity of the Pyrex, (W/m-K)
k_{si}	Thermal conductivity of the silicon, (W/m-K)
L_{array}	Channel array Length, (m)
L_{sb}	Sub-cooled length of channel, (m)
L_{tp}	Saturated length of the channel, (m)
M	Combination of terms $\sqrt{hPkA_c} \cdot \Theta_b$ in fin equation derivation
m^2	Combination of terms $\frac{hP}{kA_c}$ in fin equation derivation
m_c	Slope for T_h=f(R_h) calibration
m_l	Slope for q_{loss}=f(T_h-T_{amb})
$\dot{m}$	Mass flow rate, (kg/s)
N	Number of channels and fins, (m)
Nu	Nusselt number
Nu_3	Nusselt number for three heated side geometry
Nu_4	Nusselt number for four heated side geometry
NCF	Nusselt correction factor for correlations Nu_3/Nu_4
P_{in}	Power supplied to the heater pad, (W)
P_{sb}	Fin perimeter for subcooled region, (m)
q”	Heat flux (W/m^2)
q_{in}	Adjusted q_{wall} for saturated or sub-cooled regions, (m)
q_{loss}	Heat loss to ambient, (W)

q_{loss-1}	Heat loss to ambient by mode #1, (W)
q_{loss-2}	Heat loss to ambient by mode #2, (W)
q_{loss-3}	Heat loss to ambient by mode #3, (W)
$q_{loss-total}$	The total heat loss to ambient, (W)
q_{out}	Heat transferred from the channels based on fin equation, (W)
q_{sp}	Single phase heat transfer, (W)
q_{wall}	Effective heat applied, (W)
R_h	Electrical resistance of heaters, (Ω)
R_o	Heater electrical resistance taken at some known value of temperature, (Ω)
Re	Reynolds number
T_{amb}	Ambient temperature, (^{o}C)
T_h	Heater temperature, (^{o}C)
T_{in}	Inlet thermocouple temperature, (^{o}C)
T_o	Base line temperature at which R_o is measured, (^{o}C)
T_{out}	Outlet thermocouple temperature, (^{o}C)
T_{sat}	Saturation temperature, (^{o}C)
T_{wall}	Extrapolated silicon surface temperature, (^{o}C)
t_p	Thickness of the Pyrex, (m)
t_{si}	Thickness of the silicon, (m)
W_{array}	Channel array width, (m)
W_c	Channel width, (m)
We_l	Weber number of the liquid
W_f	Fin width, (m)

X_k	Magnitude of Fast Fourier Transform Coefficient
x_e	Exit Quality

Greek Symbols

α	Resistance to temperature coefficient, ($\Omega/(\Omega\text{-}^{o}C)$)
β	Channel aspect ratio W_c/H_c
ΔT_h	Difference of heater temperature and ambient temperature, (^{o}C)
ΔT_f	Difference of inlet and outlet thermocouple temperature, (^{o}C)
ΔT_{in}	Difference of inlet thermocouple and ambient temperature, (^{o}C)
Θ_{b-sb}	Difference of wall temperature and mean fluid temperature, (^{o}C)
μ_l	Viscosity of the liquid (N-s/m^2)
ρ_l	Density of the liquid (kg/m^3)
ρ_v	Density of the vapor (kg/m^3)
σ	Surface tension (N/m)

INTRODUCTION

Current demands for consumer electronics as well as specific high power computing applications have kept designers at the drawing board on several fronts. These demands have driven drastic progress in microfabrication techniques yielding smaller transistor feature sizes and increased levels of circuit integration. As a result, this has caused a dramatic increase in power densities on today's microprocessor chips. These trends have continued for decades and show no sign of slowing down. This growth pattern that has continued a typical trend of doubling every two years is often referred to as Moore's Law. The number of transistors per processor plotted against time is seen in Figure 1. This information has served as a guideline for industry road maps and remains a predictable pattern in growth trends.

The trends of faster and more powerful electronics have overwhelmed the heat removal capabilities of conventional techniques used to cool the electronics. Due to cost reasons and reliability issues, the predominant techniques used today consist of air cooling whether by passive or active means. An example of this is that many servers today are cooled by natural convection for reliability purposes and almost all PC's are cooled by a fan/heat sink configuration due to cost issues. The continued growth of modern electronics depends greatly on the development of new and creative forms of heat removal.

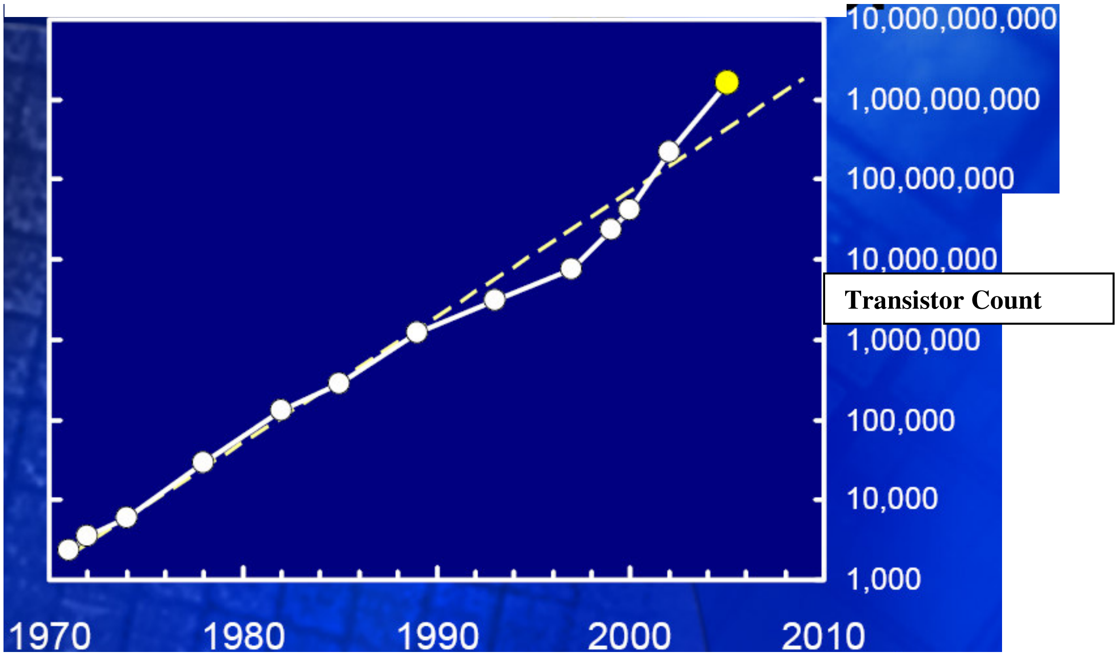

Moore's Law

Figure 1: Moore's Law stretched over 3 decades showing the trend of transistor count increase versus time, Prasher, et al.[2006].

Over the years several promising heat removal techniques have been proposed and some are currently in their industrial infancy. Peltier devices or thermoelectric coolers are one such example. Another general area of interest is liquid cooling. Due to the enormous increase in thermal capacitance and heat transfer properties of liquid cooling over air makes it an enticing choice. Some principal approaches are heat pipes, pool boiling, direct jet impingement, and microchannels.

Liquid-cooling techniques being proposed range from indirect methods where the heat is dissipated from the electronics into a heat spreader that is then cooled by conventional liquid-cooling schemes, to direct methods wherein a dielectric liquid physically contacts the electronics. Within each of these broad classes of techniques, both single-phase cooling methods and phase-change cooling methods are being evaluated in the search for a means to cool the next generation of high-powered electronics.

A liquid-cooling technique that is the subject of much attention is the use of coolant flowing in microchannels. This configuration leads to very high heat dissipation capability because the cooling characteristics scale inversely on the size (hydraulic diameter) of the flow passages. When the high heat removal capability of microchannels is coupled with the inherently better physics of heat removal in the presence of phase-change (convective boiling), it makes for a very potent combination indeed.

The study of phase-change heat transfer in microchannels is in its infancy primarily because fluid behavior in such a confined space is vastly different from that found in more conventional macroscopic geometries. Firstly, dielectric fluids used in electronics thermal management have extremely poor thermal characteristics necessitating the use of structured surfaces in order to achieve the desired thermal performance. The development of a fundamental understanding of this flow situation requires the measurement of local temperature and flow information to supplement semi-empirical analyses that are being developed. One of the more vexing problems is the appearance of flow instabilities. Flow instabilities in two-phase systems are more severe than those in single-phase systems. They can lead to large-scale temperature and pressure excursions.

In an effort to provide answers to some of these issues, test devices have been fabricated in a range of microchannel sizes. These test devices have been equipped with custom-fabricated temperature sensors, fluid delivery systems, two-phase promoting features in the base of the channels and simulated heat sources. The current work describes the fabrication of the heat sinks and concludes with a description of successful acquisition of practical information that will lead to implementation of this thermal management technique in high-powered electronics.

CHAPTER 1: LITERATURE REVIEW

This review starts out with a conceptual introduction to the microchannels followed by a brief discussion of the general characteristics of flow boiling. Many researchers have developed a wide array of fabrication techniques for research purposes which will also be covered along with different types of flow delivery systems and working fluids of choice. A strong inhibiting factor in microchannel research is the presence of flow instabilities during two phase heat transfer. A hand full of the leading researcher and their work will be discussed as well as a few local surface enhancements developed to combat them.

1.1 **Introduction to microchannels:**

Microchannel theory and research has been at the forefront of high heat flux heat removal research for close to three decades. It has picked up momentum in recent years and continues to be a hot topic of research for many groups of interest. Microchannel research has seen several changes over the years that are attributed to the development of microfabrication techniques. This is because both the IC industry and microchannel research have length scales and feature sizes that are difficult to work with and that many of the microchannel devices that have been developed are constructed using derivatives of IC technology.

The first major introduction of the concept and testing of microchannels were conducted by David Tuckerman in a research group out of Stanford University in the early 80's. Tuckerman and Pease [1981] researched the applicability for single phase heat transfer of microchannels for IC cooling purposes. For fully developed internal laminar flow, the Nusselt number is a constant value for boundary conditions of constant heat flux and constant wall temperature. By definition, if the Nusselt number is constant then there is an inverse relationship between heat transfer coefficient (h) and the hydraulic diameter (D_h) as seen in Equation 1. An example of this effect is for water flowing in a 200μm square channel under constant heat flux boundary condition the heat transfer coefficient exceeds 12000W/m^2-K.

$$h = \frac{Nu \cdot k}{D_h} \tag{1}$$

Many have argued over the laminar boundary condition of microchannels. Due to the inherently small hydraulic diameters it is difficult to reach Reynolds numbers greater than the accepted transition point of 2300. This is a debate that is ongoing due to the controversy about the threshold at which transition occurs. Many have also debated over the definition of a microchannel in terms of size. An excellent summery of microchannel history and general characteristics has been laid out by Kandlikar and Grande [2003]. In this review, a size definition is presented as seen in Table 1.

Conventional Channels:	$\mathbf{D_h > 3mm}$
Minichannels:	$\mathbf{3mm \geq D_h > 200\mu m}$
Microchannels:	$\mathbf{200\mu m \geq D_h > 10\mu m}$
Transitional Channels:	$\mathbf{10\mu m \geq D_h > 0.1\mu m}$
Molecular Nanochannels:	$\mathbf{0.1\mu m \geq D_h}$

Table 1: Channel size definition from Kandlikar and Grande [2003].

Microchannel research has gained in value in past years. Strong interest in microchannel applications have grown in areas such as electronics cooling, fuel cell development, biomedical research, as well as space and fusion power research. This burst of demand is a call to arms for more experimental and analytical work in this area.

1.2 **Introduction to flow boiling:**

Flow boiling has been extensively researched since the early 1900's. The enormous heat transfer potential of phase change as been harnessed time and again for high heat flux applications. Flow boiling is predominantly practiced in industrial processing and power generation but the electronics community is looking to harness it as well. Due to the complexity and randomness of the two-phase flow, most correlations to describe such things as heat transfer and pressure drop are typically empirical in nature.

Figure 2 is a typical depiction of the flow boiling curve for highly wetting fluids, such as the one used in the current study. This is done by plotting heat flux (q") against wall superheat (the difference between wall temperature (T_w) and saturation temperature (T_{sat})) under constant heat flux conditions. The first of the four dominant regions of the curve is the Single Phase Forced Convection portion which extends from points (a-b). At point (b) the boiling initiates in what is commonly referred to as ONB or Onset of Nucleate Boiling where by the increased heat transfer coefficient induced by the phase change causes the temperature to drop to point (c). This path from (b-c) is referred to as boiling curve hysteresis or Temperature Overshoot.

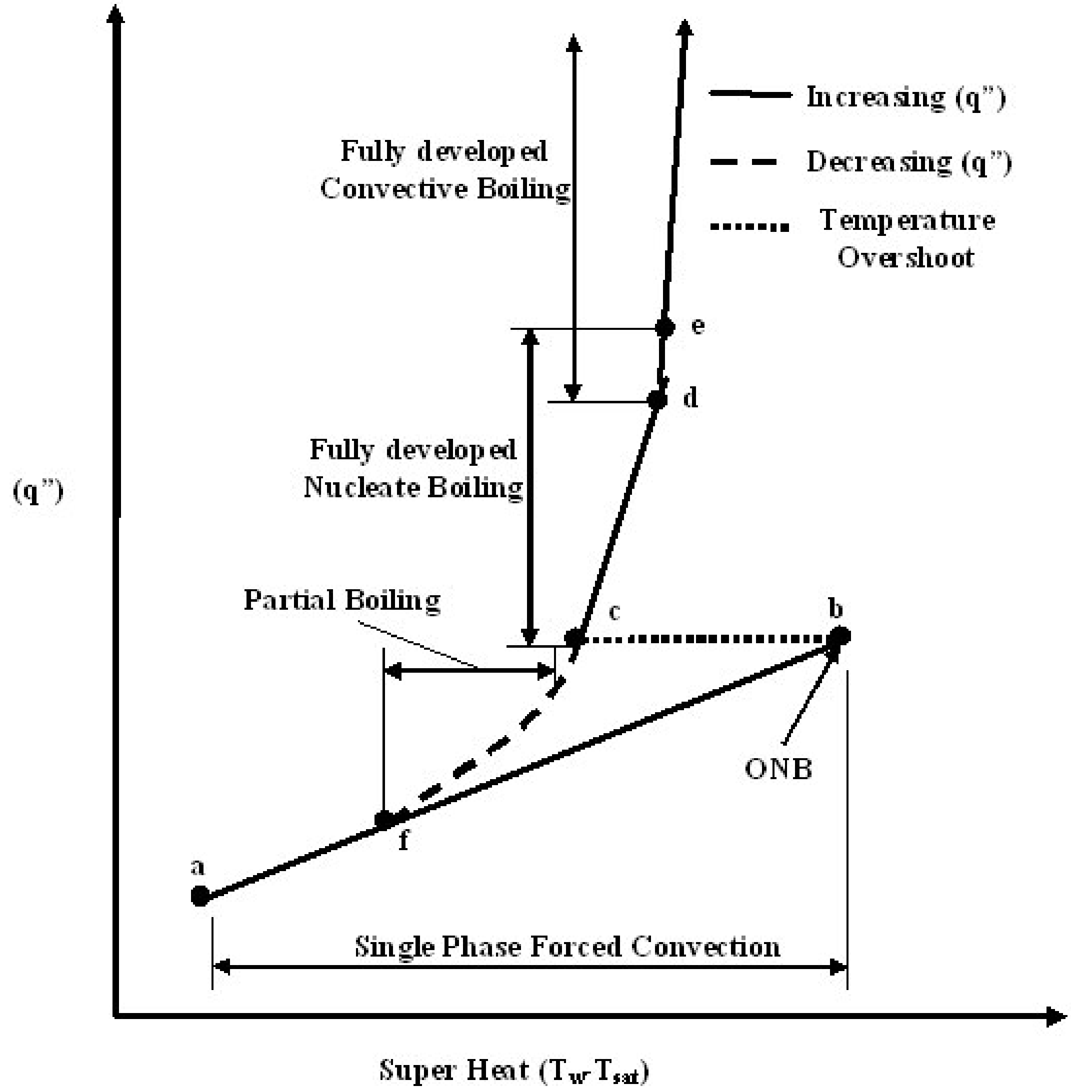

Figure 2: Generic flow boiling curve for constant heat flux conditions.

A further increase in heat flux from points (c-d) leads to the region of fully developed nucleate boiling. This region is characterized by all vapor generating activity coming from scratches or imperfections in the heated surface. As heat flux continues to increase from point (d-e) a transition region is encountered from nucleate boiling to convective boiling. Beyond point (e), the flow is dominated by fully developed convective boiling. This region is characterized by a large vapor core surrounded by a thin film of saturated liquid in contact with the surface, with phase change occurring at the interface of the liquid and vapor by thin film evaporation rather than at surface imperfections. As you traverse back down in heat flux, the region commonly described as Partial Boiling is encountered. Defined by points (c-f), this region makes a smooth transition back in to single phase as heat flux is lowered. Also, it should be understood that the regions of this curve are apt to variation by system conditions and is qualitative in nature.

As previously mentioned the electronics community is seeking to capitalize on the enormous heat transfer potential of flow boiling. By utilizing flow boiling in microchannels, the IC industry hopes to develop active cooling schemes for tomorrow's high powered electronics.

1.3 **Microchannel fabrication and design:**

1.3.1 **Heat sink fabrication**

Due to the inherently small feature sizes, it is easily seen that the fabrication of microchannels can be a bit cumbersome. Advances in materials, precision machining, and microfabrication techniques have greatly improved the applicability and practicality of microchannels.

Past researchers have tested a wide variety of materials, geometries and fluids. With the exception of a few, all the designs contained a handful of similar characteristics. A few of the common traits of microchannel work are a high thermal conductivity substrate with the tops of the channels open, an optically clear cover plate that seals the channel and allows for flow visualization, and a quasi-uniform heat flux source.

Micro machining processes such as laser cutting, micromilling, and EDM machines have made materials such as copper and aluminum the test materials of choice for many researchers. Warrier, et al. [2002] machined 5 parallel channels with a D_h=750μm into aluminum and used another aluminum plate to cover the channels. This negated the ability of flow visualization but this was not the object of the study. The researchers used Inconel heater strips applied symmetrically at the top and bottom of the test section.

Copper is a very popular material of choice. Liu, et al. [2005] machined 25 parallel channels with a D_h=384μm into a copper array and used a G7 fiberglass cover plate which allowed for flow visualization and insulation. Cartridge heaters were placed in the copper block for asymmetric heat flux application. Qu and Mudawar [2003 a,b,c] machined 21 parallel channels with a D_h=348μm into copper and used a lexan cover plate for viewing of the channels. Cartridge heaters were also used in this research and placed in the copper block for asymmetric heat flux application.

Future hopes of physically integrating the microchannel heat sink into the inactive side of a microprocessor have propelled several researchers to use silicon substrates for their channel fabrication. This desire has been fueled by increased bulk heat densities as well as localized hot spots that are present on today's integrated circuits. It is believed that by integrating the coolant flow passages into the processor itself that the conduction resistances of common heat removal schemes will be reduced and the active management of localized hot spots, as those seen in Figure 3, can be achieved.

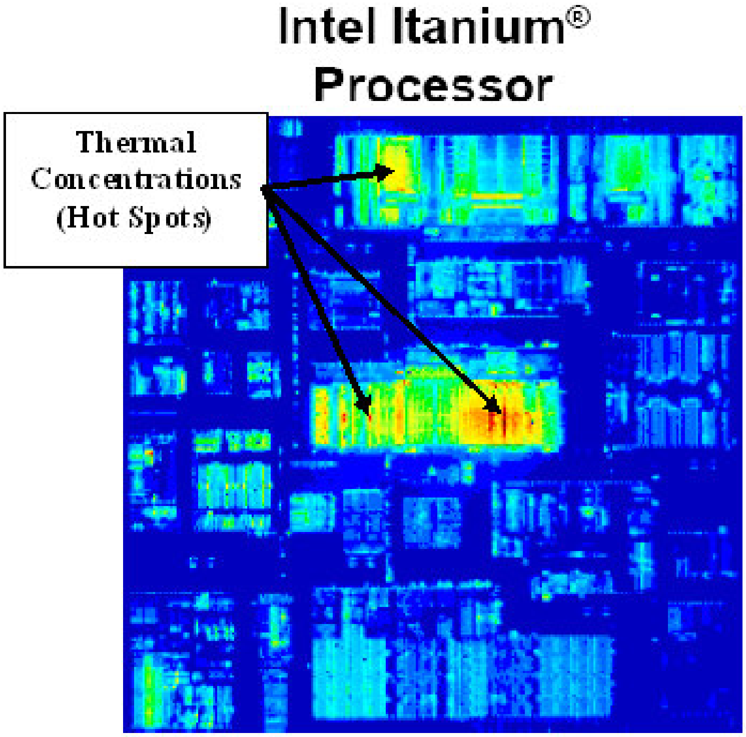

Figure 3: Thermal imaging of Intel's Itanium Processor, Prasher, et al.[2006].

These types of test sections are typically constructed using IC and MEMS processes. Zhang, et al. [2004] constructed single channel and multi-channel test sections using silicon as a substrate. Reactive Ion Etching (RIE) was employed to create a series of specimens with hydraulic diameters ranging from 25-65μm. The tops of the channels are sealed by anodically bonding a piece of Pyrex glass to the silicon. Boron doped resistors are implanted on the back side of the silicon microchannel array for heating purposes. Hetsroni, et al. [2001 & 2002] constructed multi-channel test sections using silicon as a substrate. A crystalline plane specific chemical etch was employed to create a series triangular shaped channels with hydraulic diameters of 151µm. The tops of the channels are sealed by anodically bonding a piece of Pyrex glass to the silicon which allows for flow visualization. Metallic thin film resistors are deposited on the back side of the silicon microchannel array for heating purposes.

One must be careful in designing the inlet and outlet plenum areas of silicon test sections. Due to the high thermal conductivity of the silicon it is prone to thermal spreading. Kramer, et al. [2004] etched a single 100µm × 100µm channel in silicon bonded to a Pyrex 7740 cover to allow for sealing and visualization. As in the previous reference to Zhang, et al. [2004], the heat source was provided by a series of boron doped resistors in the base of the silicon. The inlet and outlet plenum areas were formed into the silicon. Some issues were reported in pre- and post-heating of the fluid due to conduction.

Varying geometries of all types have staked their claim in the microchannel arena. This very often makes comparing heat transfer data difficult and assumption filled. Table 2 gives a few of the microchannel designs from previous work.

Steinke and Kandlikar [2003] –(Rectangular)-(D_h=207µm)	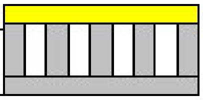
Hetsroni, et al. [2003] –(Triangular)—(D_h=151µm)	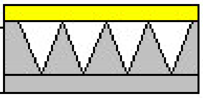
Bowers and Mudawar [1994] –(Circular)—(D_h=510µm)	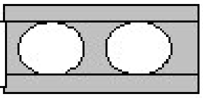
Wu and Cheng [2003 a,b] –(Trapazoidal)—(D_h=158µm)	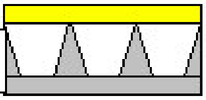

Table 2: Comparison of channel geometries explored by various researchers.

1.3.2 Temperature sensing

Definitive heat transfer data is hard to ascertain in microchannels due to the extreme difficulty of gathering local surface and fluid temperature measurements within the channels. This is due to the small feature sizes involved which expressed in a research review posed by Bergles and Kandlikar [2005]. With every attempt made, assumptions have been imposed or only a part of the total picture has been captured. A few of the attempts at temperature mapping are as follows.

The previously mentioned work by Qu and Mudawar [2003 a,b,c] and Liu, et al. [2005] were both microchannel arrays fabricated out of copper blocks. Both sets of researchers embedded thermocouples into the base of the copper microchannel arrays to obtain axial conduction data within the heat sink. These are not true surface temperatures so 1-D conduction is employed to extract these values.

Kosar, et al. [2005 a,b] and Kuo, et al. [2005] have constructed silicon microchannels that are anodically bonded to Pyrex. Heat supplied to the test section by a set of aluminum thin film heaters deposited on the back side of the silicon microchannel array. The resistance of these aluminum heaters is also calibrated against temperature for average heat source temperature data. A similar method of temperature data retrieval is conducted by Jiang, et al. [1999], Zhang, et al. [2004], and Kramer, et al. [2004]. This method also consists of using the heat source as the temperature sensor. Boron is implanted into the back side of the silicon microchannel array and then the resistance is calibrated against temperature.

Hetsroni, et al. [2002] took a different approach by using an infrared camera that is zoomed in on the area of the heater pad. This approach is unique in the since that it could gather axial, channel to channel as well as average heater temperature. As previously mentioned, all of these methods are external to the microchannels themselves and involve the assumption of 1-D conduction to attain the channel surface temperature.

A unique effort has been made by Park, et al. [2003] to place RTD sensors inside the channel. This single channel study was conducted in a silicon substrate with a channel width of 200μm. The platinum RTD sensors were deposited onto a Pyrex glass wafer which was then anodically bonded to the silicon. The RTD's ran the axial length of the channel and were very close in appearance to those portrayed in Figure 4.

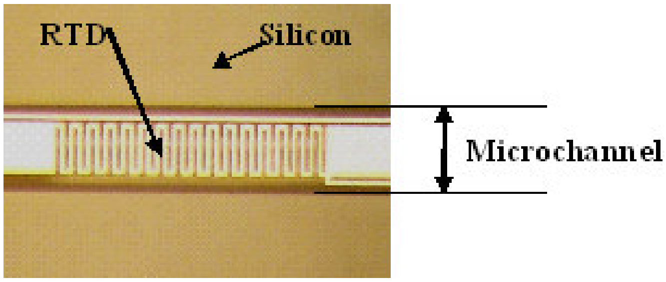

Figure 4: RTD inside microchannel passage.

1.4 **Flow loop systems for microchannel study**

Flow loops for the testing of microchannels vary as much as the microchannel designs themselves. This can also have a drastic outcome in terms of data comparison. Some researchers have based their design on practical application, but most do not. Most systems are formulated to maintain desired conditions while data is collected with little to no transients. There are typically two types of testing loops, an open loop and a closed loop. An open loop system usually consists of two reservoirs, one on either end of the loop. The first reservoir contains the working fluid at some predetermined set of conditions which is forced through the test specimen for data collection where it then empties into the second reservoir. A closed loop system is a continuously fed loop with the use of condensers, heat exchangers and heaters to maintain the working fluid at a desired set of condition before entering the test section.

Wu and Cheng [2003 a,b] took and interesting approach to the open loop system by pressurizing the inlet side reservoir tank, which was filled with water, by means of a high pressure nitrogen supply. This inlet reservoir was maintained with a regulator at a constant pressure. This set up negated the use of a pump due to the exit reservoir being open to ambient conditions. A similar design was tested by Steinke and Kandlikar [2003] which used an externally heated pressure cooker for the inlet reservoir. The pressure was maintained with this system by application of a constant heat input and a variable pressure relief valve. Neither study used a pump. This is a constant pressure drop system as opposed to constant flow rate. This system works quite well under single phase conditions but when boiling is introduced it can lead to large scale flow disruptions.

Zhang, et al [2004] and Park, et al. [2003] both designed a constant flow rate open loop system. These systems used a syringe pump which serves as the inlet reservoir. Syringe pumps are excellent at providing a constant flow rate for experiments but the do have their drawbacks. This type system makes adjusting inlet conditions difficult in terms of degassing the working fluid and for large flow rate situations may not store enough volume.

A good example of the alternative to the open loop systems previously described is a closed loop test system used by Liu and Garimella [2005]. This loop is a continuous feed system driven by a variable speed gear pump. A precision gear pump curve is pretty flat, and this means that at a given rpm, the pump will deliver a continuous amount of fluid over a wide range of pressure drops. This system results in a constant flow rate condition but without the intermittent stopping to recharge the pump as with the syringe type.

These systems previously described are very well suited for testing applications but practical implementation is a whole other issue. A liquid cooling system for a PC will have to be compact, reliable, quiet and conservative in power consumption. Pump types are a major source of debate when it comes to physical implementation. Singhal, et al. [2003] gives a good review of pumping requirements for microchannel systems. One type of pump that has caught the attention of the electronics cooling community is the electroosmotic pump. This style of pump has no moving parts and is virtually silent. The performance of one of these pumps in conjunction with a microchannel system is explained in Jiang, et al. [2002]. With these things in mind, the design of reliable microchannel cooling systems for electronics applications requires the further development of reliable fluid delivery systems.

1.5 **Working Fluids for boiling applications**

A wide range of working fluids have been used in microchannel research. Most single phase studies have rightly chosen water for its excellent heat transfer properties but water poses a problem during two-phase boiling for electronics applications. The atmospheric boiling point of water is too high for reliable electronics cooling. This is why the IC cooling community has turned its attention to Fluorinert coolants and refrigerants for their low boiling point and dielectric characteristics. Also, bubble sizes in dielectric fluids are an order of magnitude smaller and therefore lead to bubbly flow and/or slug flow patterns over the flow passage which is reported by Mukherjee and Mudawar [2003].

Some of the drawbacks of dielectric coolants are the very poor heat transfer properties as well as an extremely low surface tension. ONB is typically triggered by a scratch or imperfection in the heated surface that trap existing vapor. Bergles and Kandlikar [2005] suggest that by having a low surface tension as dielectrics do, these vapor triggering sites have a tendency to be flooded out postponing ONB and causing large temperature overshoots as seen in Figure 2. This phenomenon is portrayed in the flow boiling data presented by Bowers and Mudawar [1994] that used R-113 as their working fluid.

Any convective boiling study must pay careful attention to the control and measurement of dissolved gases. This is especially true when experimenting with dielectric fluids like FC-72 that can contain as much as 49% dissolved gas by volume. A recent paper (Steinke and Kandlikar [2003]) attempted to quantify the effect of three levels of dissolved air in water on flow boiling in microchannels. These three cases were reported using the dissolved oxygen concentrations of 8.0 ppm, 5.4 ppm, and 1.8 ppm. During this work, six, parallel 207μm hydraulic diameter microchannels were fabricated in a copper substrate, covered by a Lexan sheet. The higher dissolved gas content resulted in earlier nucleation incipience, as expected. However, a decrease in heat transfer coefficient was observed just after incipience occurred, which had not been previously reported in larger microchannel studies and did not occur at lower dissolved gas concentrations. This phenomenon was attributed to the formation of an insulating layer of dissolved gas bubbles on the channel surface.

1.6 **Flow instabilities in microchannels**

Flow instabilities in two-phase systems are more severe than those in single-phase systems. They can lead to large-scale temperature and pressure excursions. Instabilities can be due to a single mechanism (fundamental instability) or a combination of mechanisms (compound instability). Relaxation-type instabilities occur at the transition between flow regimes wherein one hydrodynamically compatible set of conditions drives the flow to make a transition towards the other set of compatible conditions and back again.

The stability of two-phase flow in microchannels, essential to reliable cooling of microelectronics, is considered to be a function of the transition between bubbly flow and the elongated slug flow regime. Several studies on flow boiling in microchannels report two types of instabilities. The first type of instability is associated with excursions of flow and is sometimes referred to as the Ledinegg instability. This is a fundamental static instability that manifests itself as a low frequency but high amplitude variation of the amount of vapor generated in each channel in a microchannel array. This leads to very large-scale fluctuations in pressure drop and consequently flow reversals as seen in Figure 5, which under some combinations of heat flux and system pressure, can become self-sustaining.

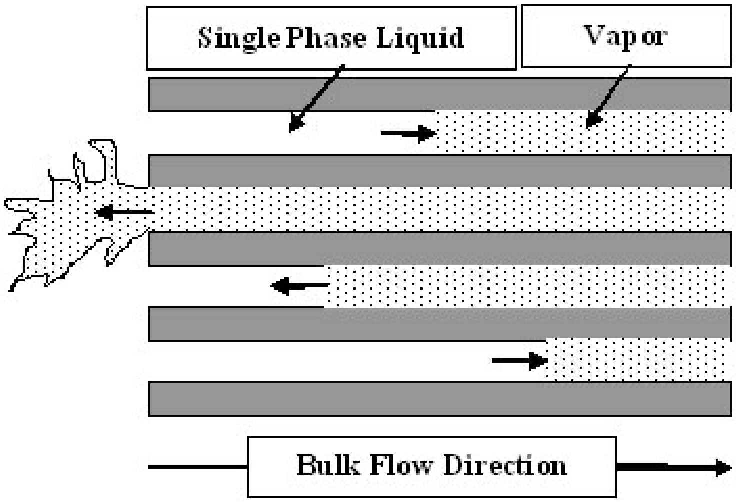

Figure 5: Flow reversal encountered during two-phase boiling.

The second type of instability manifests itself in the form of smaller yet still substantial, random fluctuations in system parameters. These instabilities lead to variations in surface temperature as high as 20°C (Hetsroni, et al. [2001], and Hetsroni, et al. [2003]). Some researchers have reported that these fluctuations have extremely long periods lasting several tens of seconds (Wu and Cheng, [2003a, 2003b]). Existing theories on reasons for the instabilities are based on the formation of randomly sized vapor slugs in specific microchannels leading to increased pressure drops in those channels, and a consequent reduction of flowrate. The reduction of flowrate in some channels precipitates an increase in flow through the other channels reducing the likelihood of formation of vapor due to an increase in single phase heat transfer. These patterns oscillate as local temperatures fluctuate. Another theory attributes these instabilities to conduction interactions between microchannels due to a non-linear coupling of this conduction with the convective boiling. Both theories point towards a compound instability mechanism. An excellent overview of the reduction of the critical heat flux during flow boiling in microchannels is provided by Bergles and Kandlikar [2005]. It is suggested that instabilities caused by both the Ledinegg mechanism and those due to upstream compressible volumes can be overcome by incorporating an orifice at the mouth of each individual microchannel.

When the growth of a departing bubble is constrained by heated walls such as in a microchannel geometry, several additional issues arise. For one, the absence of lateral neighboring nucleating sites changes the bubble dynamics. This is the regime that the current test surface is designed to address by developing a means to reliably produce stable nucleating bubbles at controlled spatial and temporal intervals. The presence of controlled nucleation sites should serve to alleviate issues associated with unstable flow boiling such as those observed by (Zhang, et al. [2004]) in studies on microchannels etched in silicon.

1.7 **Boiling surface enhancements**

As previously mentioned the thermal characteristics of most dielectric fluids are pore in nature which calls for the use of surface enhancements to aid in the feasibility of their use. Surface enhancements such as re-entrant type cavities (man made cavities that trap vapor in-between heating cycles) are desired in boiling applications due to there ability to induce premature ONB and serve as stable vapor generating sites. This is specifically of interest for low surface tension fluids as previously mentioned having delayed states of ONB and large temperature overshoots. Most of the work performed in this area has been predominantly centered on pool boiling type applications.

An experimental study by Nimkar, et al. [2004b], used anisotropic etching techniques to produce pyramidal shaped re-entrant cavity clusters in silicon. Using an anodic bonding procedure allowed the acquisition of pure one-dimensional data for the passive pool boiling heat-dissipation mechanism using dielectric FC-72. The study led to an understanding of the desired spacing between microscopic vapor-trapping surface features.

A recent study (Murthy, et al. [2004]) describes attempts to induce an early onset of boiling in a two-phase heat spreader using micro-enhancement copper structures. Several different fluids, including FC-87, FC-84, and PF5060, were tested. The enhancement structures themselves consisted of a 0.71mm thick copper plate with 0.55mm deep channels cut into both sides of the structure in a crisscross pattern. This configuration leaves a re-entrant type cavity between layers stacked on one-another and bonded using a high conductivity solder. The size and geometry of the enhancement features were found to influence the bubble formation, release mechanisms, and bubble transport. At high heat flux, the outer surfaces of the 3-D enhancement structure seemed to be more effective than the inner channels that were apparently starved of fluid.

The recent work by Kuo, et al. [2005] and Kosar, et al. [2005 a,b] employs two of the previously mentioned enhancements. 200 inter-connected re-entrant type cavities are cut into the side wall of each channel and channel inlet orifices are constructed into a silicon base. The microchannel array is anodically bonded to a Pyrex cover to permit visualization. This study reports a high frequency nucleation turnover from the large quantity of cavities which in turn reduces the thermal transient energy stored in the silicon during bubble nucleation and typical two phase transients. This study also reported the absence or suppression of flow reversals which can't be attributed entirely to either of the surface augmentation features due to no comparison test section lacking one of the two.

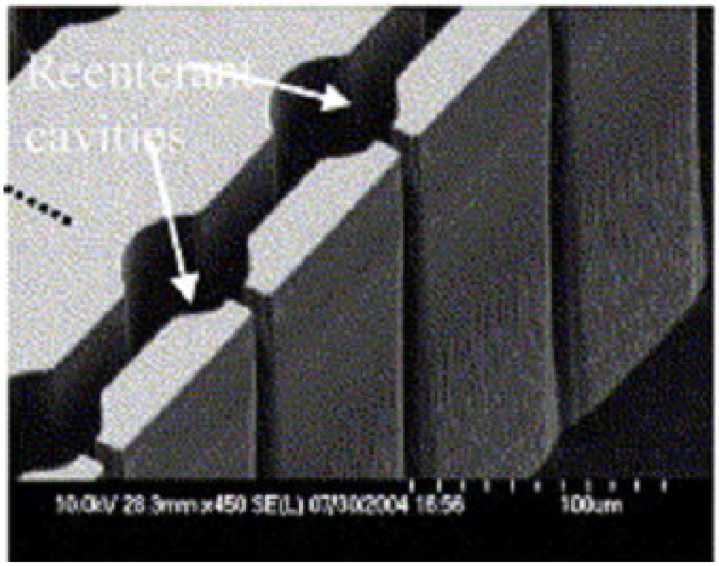

Figure 6: Re-entrant type cavities on microchannel wall Kuo, et al. [2005] and Kosar, et al. [2005 a,b]

1.8 **Literature review summary**

In light of the current literature review, it can easily be proposed that two-phase heat transfer from microchannel heat sinks are a viable heat removal solution for tomorrow's electronics community. The testing of microchannels constructed into silicon like Hetsroni, et al. [2001] and Zhang, et al. [2004], will tend to reduce thermal conduction resistances and serve to actively approach problems such as hot spots. As previously mentioned, local measurements of pressure, surface and fluid temperatures are difficult in microchannel work due to the small feature sizes involved. The need for these abilities for proper development of heat transfer correlations is expressed by Bergles and Kandlikar [2005].

Water has no competitor for extremely high heat flux removal, as shown by Qu and Mudawar [2003 a,b,c]. However, current IC's can't handle the relatively high temperature involved for this process. This is why more attention is paid to dielectric refrigerants for their low boiling points such as R-113 used by Bowers and Mudawar [1994]. Instabilities in microchannel two-phase heat transfer are also a troubling issue seen by current researcher such as Wu and Cheng, [2003a, 2003b]. To overcome these issues such as the poor thermal characteristics of dielectrics and two phase instabilities, an active approach using structured surfaces could be utilized. An example of this is the re-entrant type cavities seen in Kosar, et al. [2005 a,b].

1.9 **Objectives of this study**

- Design and fabrication of a silicon based microchannel test device.
- The integration of in-channel temperature sensors for axial measurements.
- The use of a transparent, non heated side of the test device for high speed visualization.
- The integration of pyramidal re-entrant cavities in the heated base of the microchannels.
- Fabrication of eight test devices that vary in hydraulic diameter, number of channels and number of re-entrant cavities per channel.
- Perform successful acquisition of data for heat transfer performance comparisons between test devices as well as correlation comparisons.

CHAPTER 2: DESIGN AND FABRICATION

2.1 General design overview

The heat sinks discussed in this paper consist of two types of channel configurations. The first configuration consists of 1cm x 1cm arrays of nineteen parallel microchannels and the second is a single channel geometry that is intended to help identify the different instability mechanisms by eliminating the channel-to-channel interaction that is believed to trigger one of the instabilities.

Each test section fabricated in the present study has varying channel dimensions ranging from a hydraulic diameter (D_h) of 155μm to 356 μm. This range of sizes was chosen for reasons of comparison with others work and ease of visualization.

A feature that is not exclusive to but defines the current work is the implementation of re-entrant type cavities. These cavities are located in the base of each channel, spaced equally along the length. The cavities are pyramidal in shape and have square mouth sizes of 20μm. A schematic of the cavity-enhanced microchannel geometry is depicted in Figure 7. Two different cavity configurations exist. One configuration contains two cavities per channel and the other contains six per channel. These features were placed in the base of the channels because it is closest to the heat source. From a design view, they are used to create consistent, stable two-phase vapor generating sites.

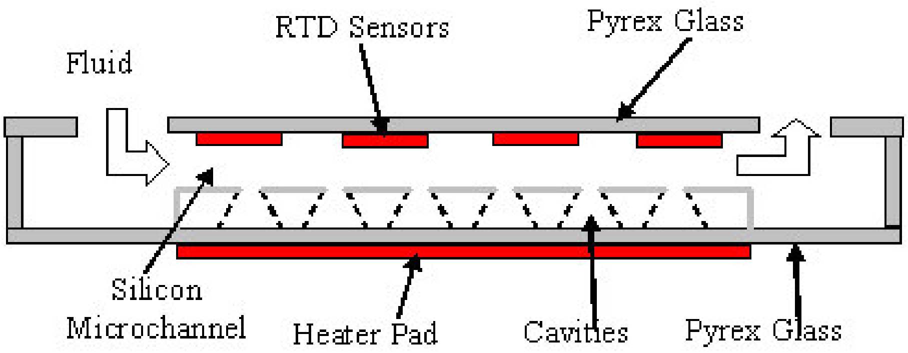

Figure 7: Schematic of microchannel geometry indicating relative position of cavity enhancements (not to scale).

There are many complexities and questions that develop in a study such as this one that can be solved through simply having the ability of visualization. Questions such as two phase confirmation during sub cooled boiling, cavity contribution to two-phase activity, flow regime transition, and magnitudes of instabilities can all be observed by different means of flow visualization. This was attained in the current study by capping the channels and plenums with a piece of Pyrex glass. This same piece of glass is also drilled for flow inlet and outlet ports which can be seen in Figure 8.

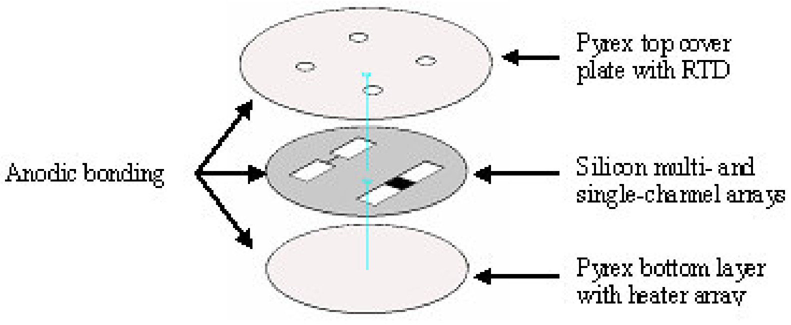

Figure 8: Exploded view of the bonded layers indicating the location of the heater pad, microchannels, and inlet/outlet plenums.

Heat is generated on the back of the test section with an array of serpentine heaters that are deposited onto another piece of Pyrex glass. This leads to another defining feature of these test sections. The current IC industry has particular interest in localized concentrations of heat generation or hot spots. The current design incorporates a series of thin film heaters that cover the backside of the test section. Using a low conductivity material such as Pyrex to transmit the heat causes a large temperature gradient across the heated layer. This has the benefit of reducing thermal spreading into the plenums to reduce pre- and post-heating of the fluid and makes heat flow closer to a 1-D scenario. Figure 8 shows an exploded view of the three layers that comprise the sandwich construction indicating the relative positioning of the microchannels, cavities, and plenums.

Due to the inherently small feature sizes that are associated with microchannel work, sensing of local fluid and surface temperatures are difficult by nature. The current study has incorporated miniature RTD's inside the channel path. Additionally the serpentine heaters themselves were calibrated for use as temperature sensors.

Reduction and quantification of heat losses are always difficult for heat transfer studies such as this. An active effort by this study to reduce these effects were to implement isolation trenches, or air gaps, that are etched on both sides of the microchannel array to reduce thermal spreading into the rest of the silicon mass. These trenches depicted in Figure 9 are implemented to obtain true 1-D data.

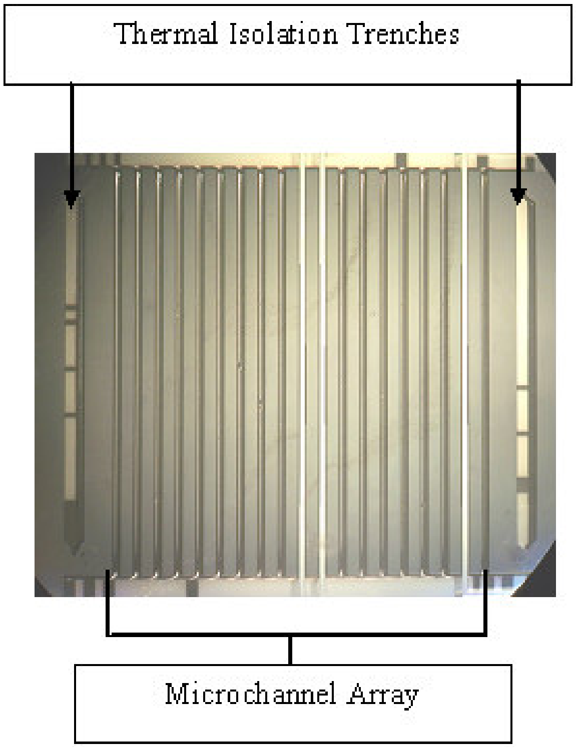

Figure 9: Depiction of microchannel array and isolation trenches.

2.2 Overall flexibility and test section characteristics

Microfabrication techniques are used to produce a total of eight microchannel test sections. Each of the test sections vary by parameters such as number of cavities per channel, number of channels, channel dimensions, heater configuration and the number of temperature sensors in the flow. Some of the unique characteristics of the eight test sections are displayed in Table 3 and the nomenclature is explained in Figure 10.

Specimen Wafer	Series 400-6		Series 400-2		Series 200-6		Series 200-2	
Individual Specimen	Single Channel	Multi Channel	Single Channel	Multi Channel	Single Channel	Multi Channel	Single Channel	Multi Channel
D_h (μm)	356	356	353	356	156	253	155	253
W_c (μm)	400	400	400	400	100	200	100	200
H_c (μm)	321	322	317	321	356	347	347	347
W_f (μm)	NA	120	NA	120	NA	320	NA	320
L_c (μm)	10000	10000	10000	10000	10000	10000	10000	10000
# Cavities Per Channel	6	6	2	2	6	6	2	2

Table 3: Matrix display of test sections and their characteristics.

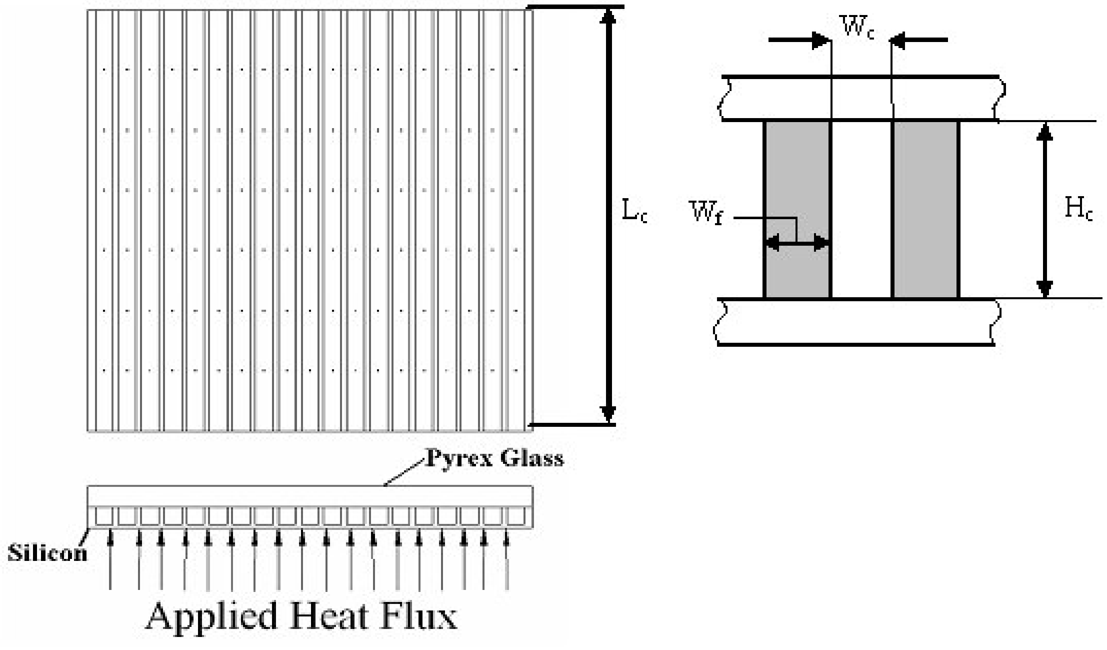

Figure 10: Symbolic Dimensions of Microchannel.

In an effort to incorporate desired input variables such as uniform heat flux as well as non-uniform, the current test sections are outfitted with two different heater configurations which can be seen in Figure 11, one for single channel test sections and the other for multichannel test sections. The single channel heat source is comprised of a single thin-film aluminum heater that is positioned directly under the channel and spans approximately the entire length. Voltage leads are attached at seven locations which split the heater into six equal increments. The multichannel test section heat source is comprised of five independent thin-film aluminum heaters that are positioned under the channel array. These five heaters can be powered differently in any number of configurations for hot spot experiments or can be hooked in series for uniform heating experiments. Voltage leads are attached at eleven locations which split the heater into six equal increments in the axial direction.

By partitioning the heaters in this manner, each individual section of both the multichannel and the single channel heater pads can then be used as a single temperature sensor. The resistance of these sensors will be calibrated as a function of temperature (R=f(T)) which will be covered thoroughly in a later section.

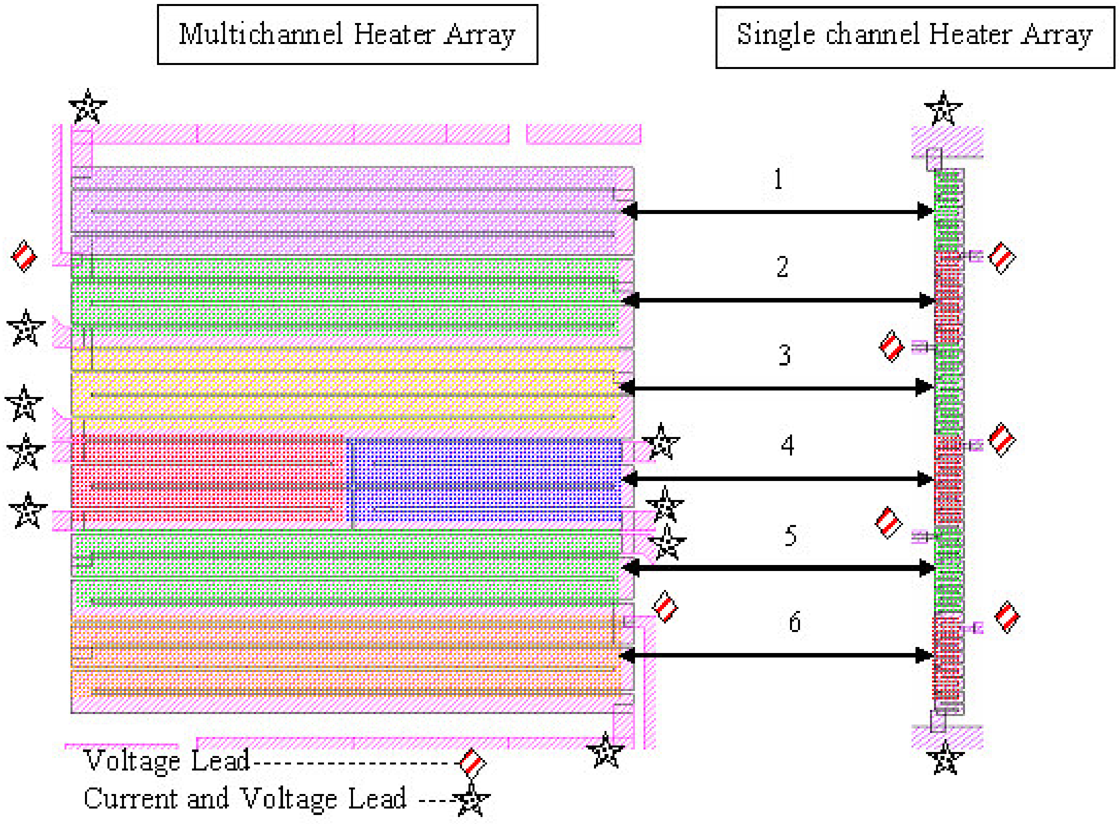

Figure 11: Heater Layout for Single and Multi Channel test sections.

As previously mentioned, due to the inherently small feature sizes that are associated with microchannel work, sensing of local fluid and surface temperatures are difficult. The current study has placed thin-film aluminum RTD's inside the channels for temperature mapping purposes. The signal retrieval of the RTD's was made possible by using FC-72 (a dielectric refrigerant) as the working fluid.

The temperature sensing configurations for the multichannel differs from that for the single channel. The multi-channel test sections contain twelve sensors each. These sensors are split into three groups of four, meaning that four sensors are aligned in series in the flow direction and spaced evenly along the length of three specific channels. The single channel test sections contain five sensors each. These five sensors are aligned individually, not in series in the flow direction and spaced evenly along the length of the channel. The discrepancy of the single channel sensors not being in series as opposed to the multichannel sensors will be explained in a later section. Figure 12 shows a good depiction of the spatial location of the sensors.

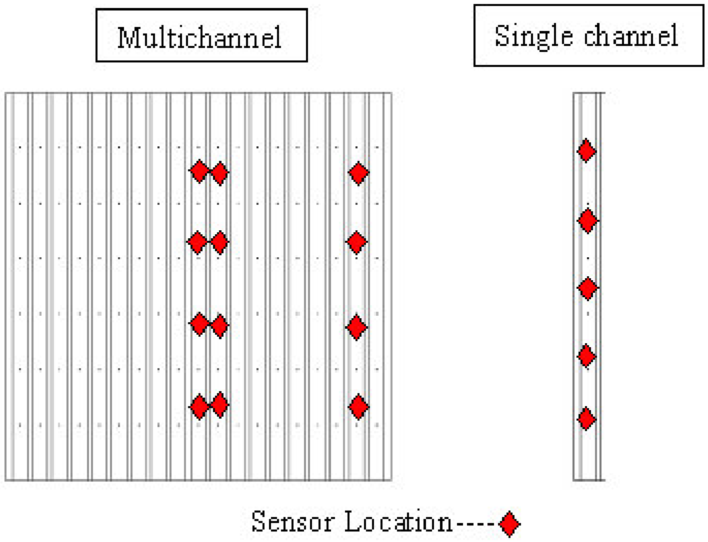

Figure 12: Temperature Sensor Layout for Single and Multi Channel test sections.

2.3 Fabrication

2.3.1 Silicon etching

The silicon portion of the test section was fabricated using a 100-mm, double side polished, n-type silicon with a crystal orientation of <100>. A 0.8μm thick layer of oxide is grown over the entire wafer for an etching buffer and general surface protection. This is achieved by placing the specimen in an Oxidation furnace for approximately 2 hours.

Photolithography is a term that will be used several times through the following fabrication portion of this thesis. This term describes the process of conveying a particular pattern onto a desired surface where the pattern feature sizes that are typically on the order of microns. This is done by spinning a liquid substance called photo-resist (that by nature is either broken down or hardened by exposure to ultra-violet light) on to the glass or silicon wafer. It is then placed in an oven to cure at some prescribed temperature and time depending on the nature of the photo-resist. Once this is complete, a mask or patterned image is place directly on top of the specimen and it is exposed to high intensity ultra-violet light for some prescribed time. After the specimen has been exposed, it is placed in a solution to develop leaving only the desired pattern behind in photo-resist. This photo-resist that is left behind is used as a buffer for particular etches and processes.

Masks are designed using a CAD package called LASI and play a very important role in the fabrication process. Each specific etch or feature added to the design requires a new mask for that process. The current specimens were designed to attain two test sections out of a single fabricated wafer, one single channel test section and a multichannel test section. Four of these wafers are produced which give a total of eight test sections as seen previously in Table 3. Once fabrication is complete they are separated. This was to insure comparability between the two in case dimensions and tolerances were not the same from wafer to wafer.

The current design uses only 5 masks, one for heaters, one for temperature sensors, one for cavities, one for sensor signal retrieval, and one for the channels. The channel dimensions and number of cavities per channel is the only thing changing from wafer to wafer, so these two masks are designed in an alternative manner. All four configurations of cavities or channels are placed on their particular mask in a square shape. By taping off the two unwanted configurations with a black UV blocking material and rotating the mask 90°, a new specimen configuration can be constructed. This is depicted in Figure 13 with the cavity mask. The masks for heaters, temperature sensors, and sensor signal retrieval are standard and do not have to be altered or tweaked between specimens.

Using photolithography and a BOE (Buffered Oxide Etch), the cavities and plenums are patterned into the oxide on the rear side of the wafer. TMAH (Tetra Methyl Ammonium Hydroxide), a directional etch based on the orientation of the silicon, is used to create the pyramidal shaped cavities. The TMAH is mixed with water and heated to 80°C. Under these conditions the oxide layer left on the wafer serves as a buffer and only those areas where silicon was exposed by the BOE are etched. The rate of etching can be accelerated or decelerated by the temperature of the solution, but under these conditions the etch rate is approximately 50µm per hour. The cavity etching procedure followed in this study, though slightly altered, came from a previous study by Nimkar, et al. [2004a].

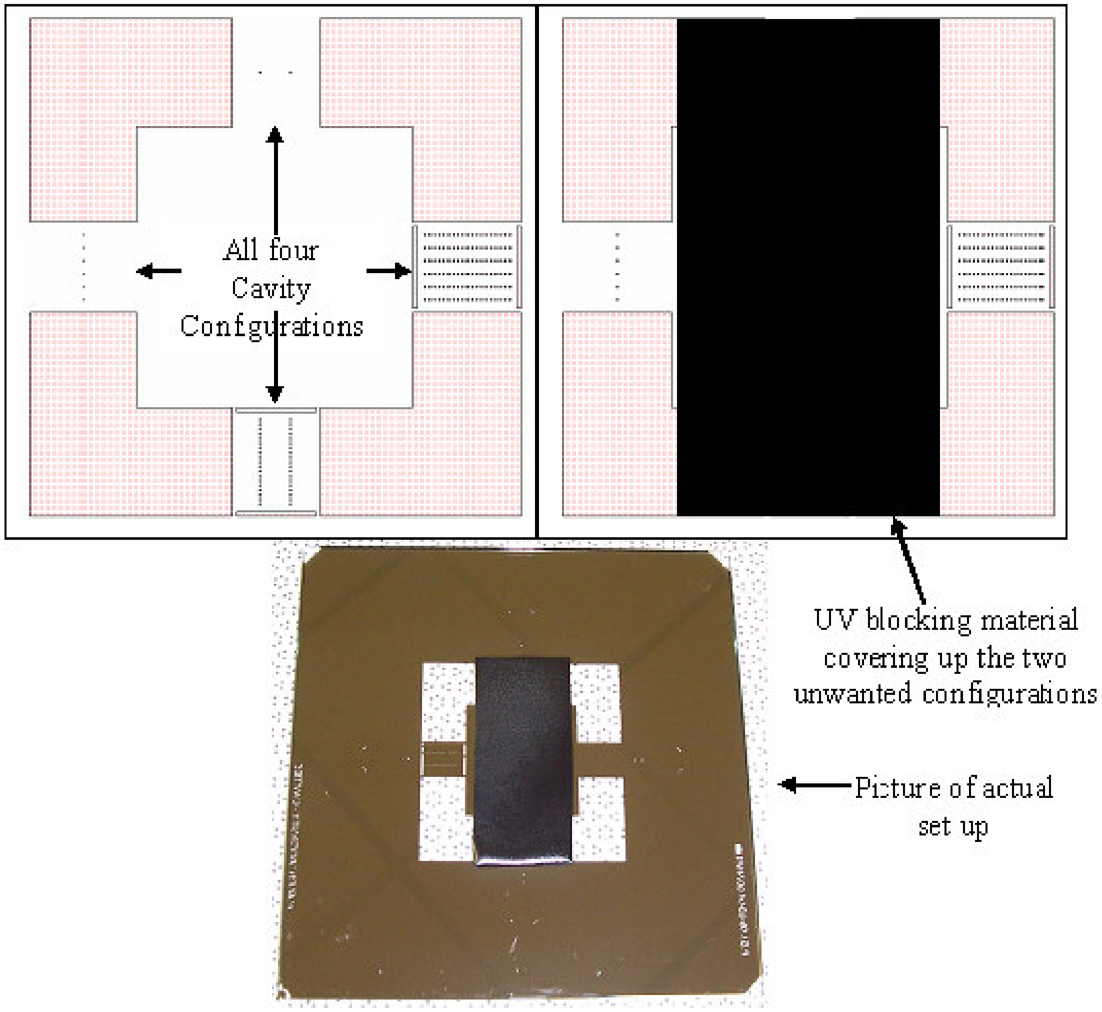

Figure 13: Mask rotation design.

The results of this etch can be seen in Figures 14(a) and (b). Figure 14(b) depicts the base of the pyramidal structure on a multi-channel test section that has two cavities per channel and Figure 14(a) shows the peak of the cavity breaching through the bottom of the channel. Also the mask design and basic features are depicted in Figure 15 along with a completed test section for visual comparison.

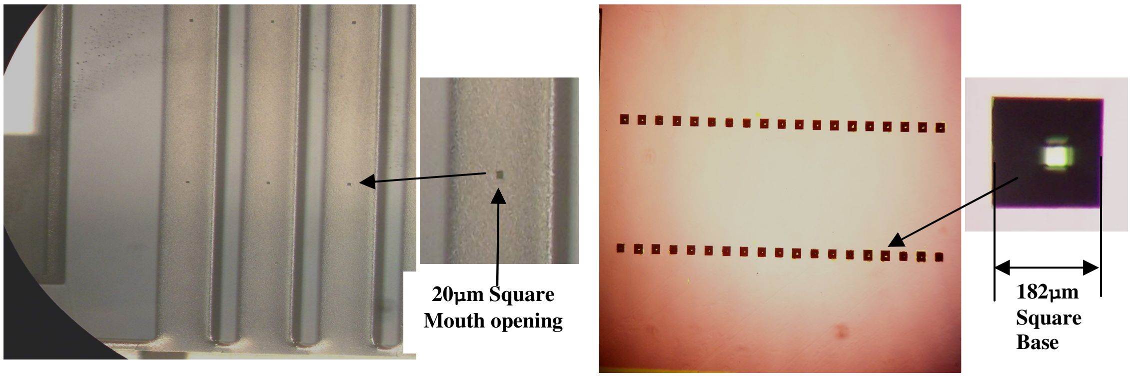

Figure 14: a) Image of reentrant cavities in the base of channels b) Cavity base on the rear of test section

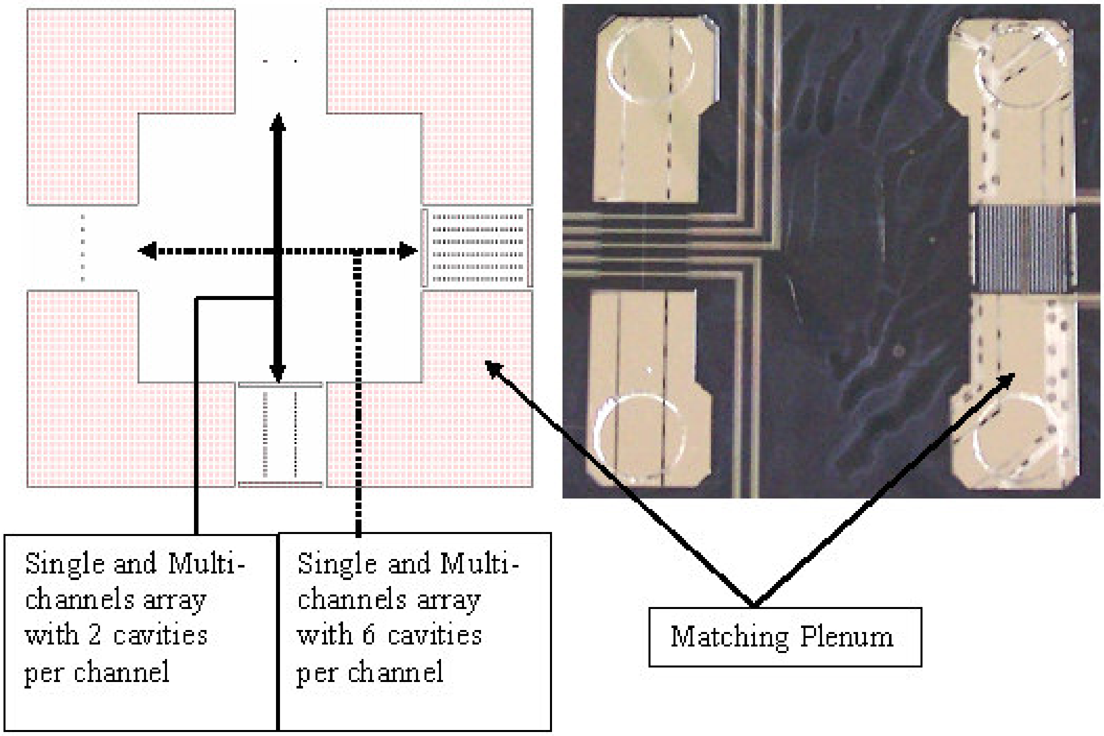

Figure 15: Mask design for cavity configuration.

After the cavities are etched and the wafer is cleaned, photolithography and a BOE (Buffered Oxide Etch) are used to pattern a series of shallow trenches on the topside of the wafer. The wafer is placed in a DRIE (Deep Reactive Ion Etcher) where the photoresist itself is used as the buffer and not the oxide layer. The DRIE machine's etch rate is dependant on the surface area that you are trying to etch or the amount of silicon area exposed to the plasma field. Under the conditions used, the etch rate was approximately 1µm per minute. A 5µm etch is conducted and then measured in a profile meter for confirmation of depth.

Besides the small feature sizes involved in trying to place temperature sensors inside the channels is the question of how to get the signal out of a sealed system. These trenches are used to carry the temperature sensor leads from the channels to the contact pads outside of the sealed test section as seen in Figure 16. The mask design and basic features are depicted in Figure 17 along with a completed test section for visual comparison.

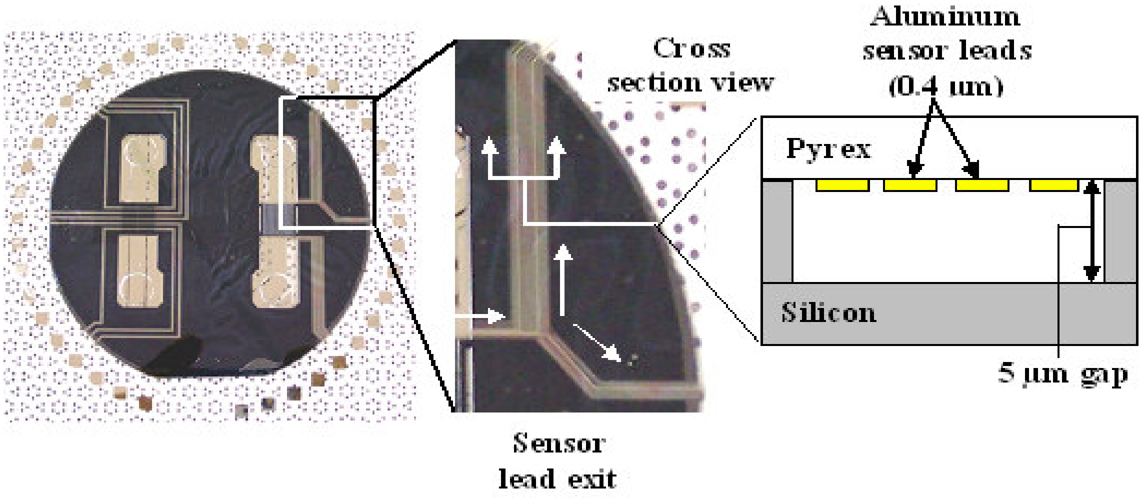

Figure 16: Image of shallow trenches for temperature sensor signal retrieval.

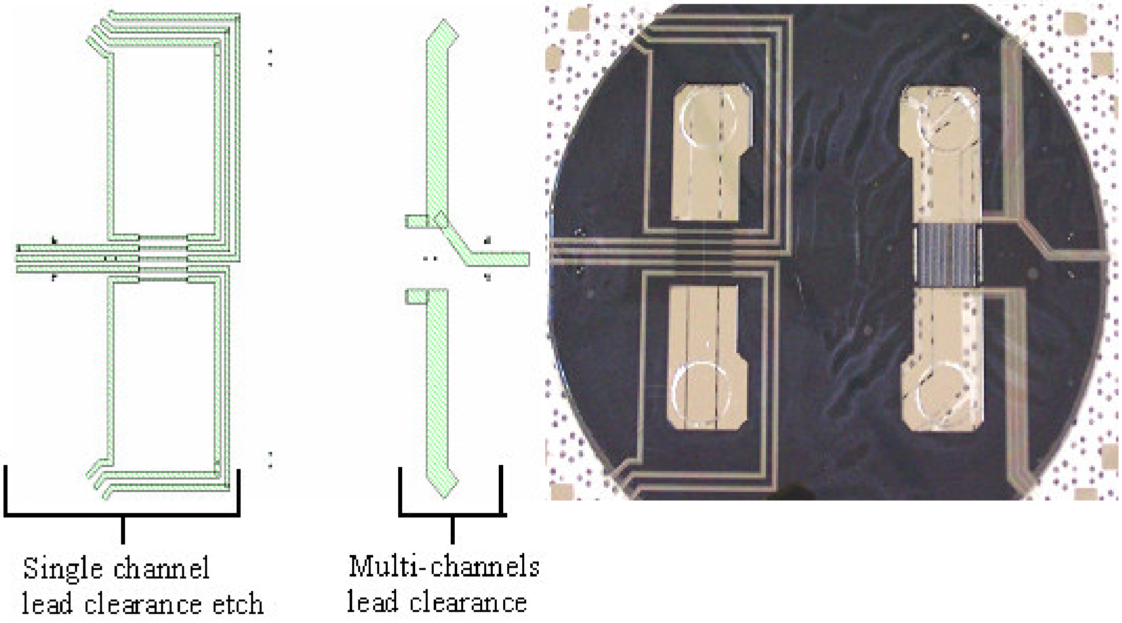

Figure 17: Mask design for lead clearance etch configuration.

The final major operation conducted on the silicon is the etching of the channels in conjunction with the inlet and outlet plenums. The silicon is cleaned and the top surface of the silicon is patterned once again in preparation. Once this is complete the wafer is placed back inside the DRIE where the channels are etched to a desired depth. Once the peaks of the cavities are breached (meaning the base of the channel is deep enough that the peak of the pyramidal cavity has breached the surface and a square opening is visible through a microscope), an iterative process of measuring cavity opening size and returning the specimen to the DRIE continues until the square cavity openings fall within a tolerance of 20µm +/- 4.5µm (Appendix C) as seen in Figure 14(a). At this point the channel array is masked off by simply painting over the channels with photo-resist. This leaves only the plenums exposed and the specimen is placed in the DRIE for etching. This is continued until both of the plenums are etched through the entire wafer thickness as seen in Figure 8. The mask design and basic features are depicted in Figure 18 along with a completed test section for visual comparison.

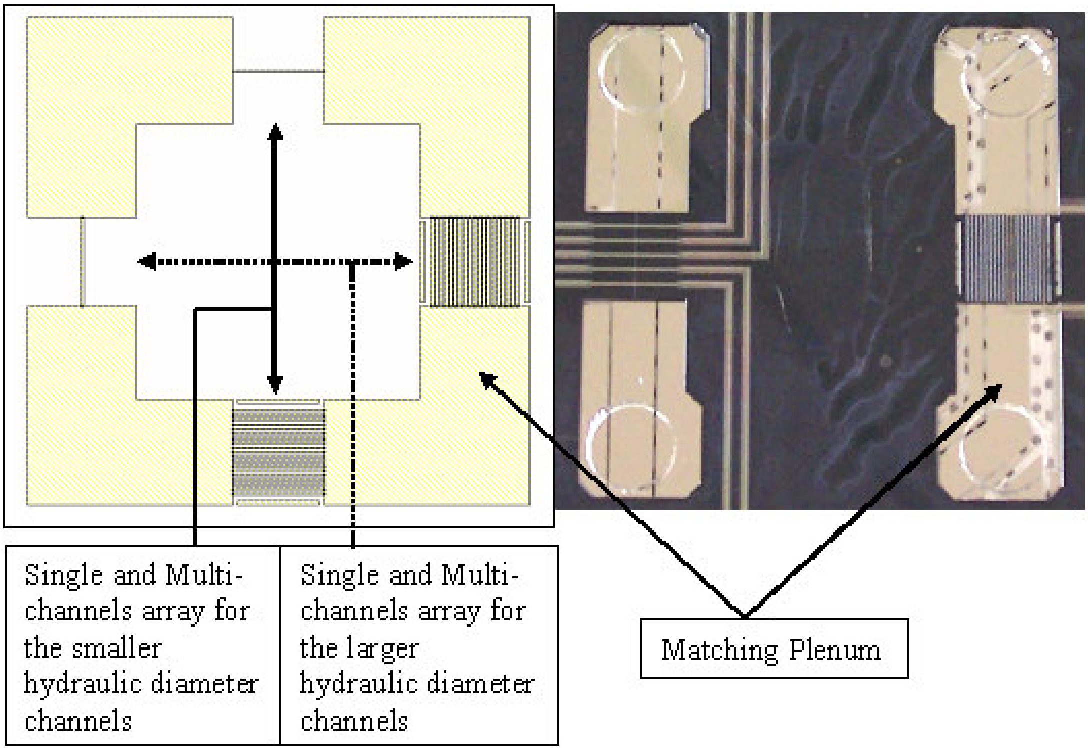

Figure 18: Mask design for channel etch configuration.

Table 4 shown below, gives a step by step account of the major processes involved in the silicon wafer fabrication of the cavities, channels and plenums. This is a tabulation of the creation of the image shown in Figure 19. Figure 19 (not to scale) is a channel centerline cut away view, and does not show the 5µm etch for temperature sensor signal retrieval.

1	Start with a 4” silicon wafer, crystal orientation <100>.
2	A 0.8µm thick layer of oxide is grown over the entire wafer.
3	Photolithography patterning of cavities and plenums on bottom side.
4	BOE (Buffer Oxide Etch) exposing silicon for cavity and plenum etch.
5	Photo-resists striped off and wafer etched in TMAH.
6	Photolithography patterning of channels and plenums on top side.
7	BOE (Buffer Oxide Etch) exposing silicon for channel and plenum etch.
8	Channels and plenums etched in the DRIE machine.
9	Wafer cleaned and all oxide removed

Table 4: Flow chart description for silicon fabrication.

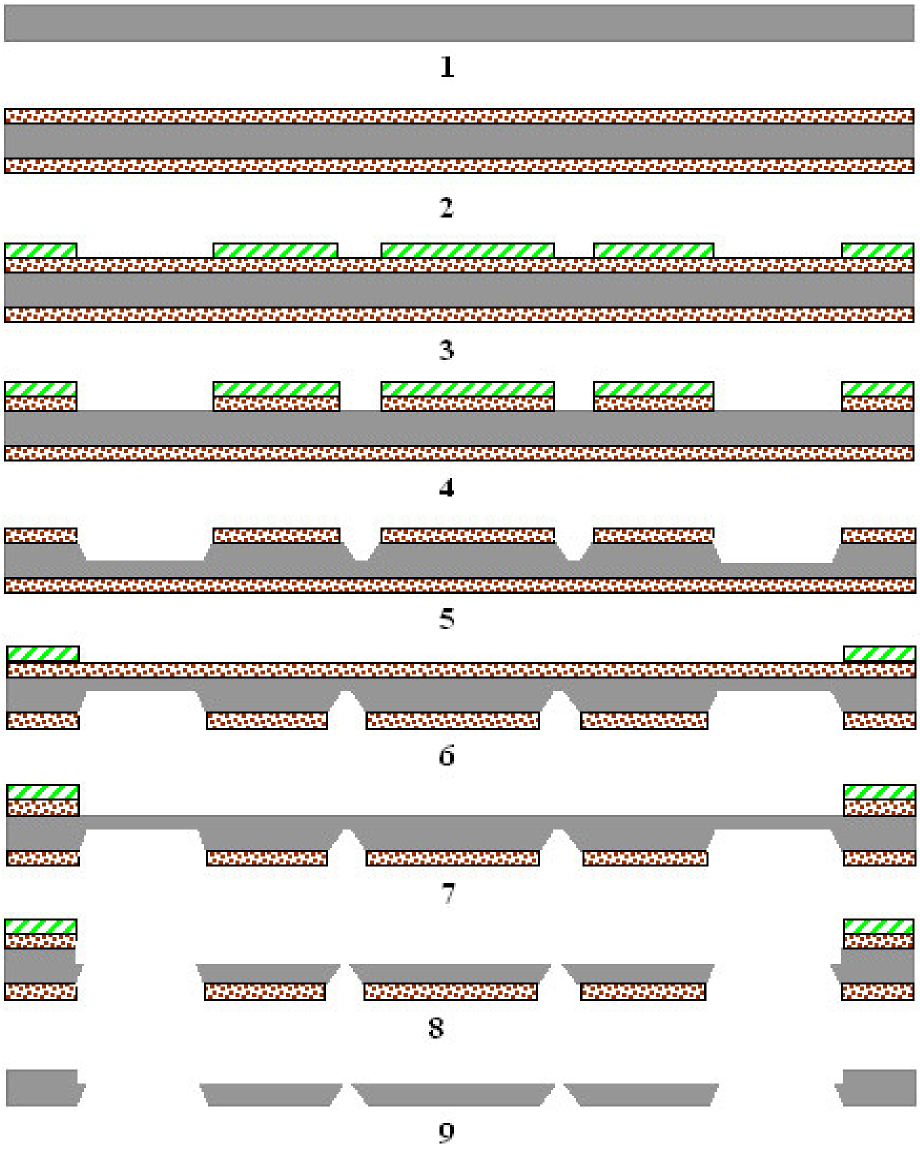

Figure 19: Silicon fabrication flow diagram**.**

2.3.2 Top Pyrex and temperature sensor array fabrication

An attempt has been made by this study to gain some insight into fluid temperature variation along the length of the microchannel by locating microthermometers on the inside (flow side) of the top Pyrex cap as depicted in Figure 20. The ability to use sensors of this type on the inside surface and in contact with the flow is made possible as previously mentioned by the dielectric properties of the working fluid FC72. This style of sensor was also used by Park, et al. [2003] for a single phase, single channel study. The multi-channel test devices contained twelve sensors each and the single channel contained five each as mentioned in the design section. Figure 20 and Figure 21 show the layout of the sensor configuration and dimensions for a multi-channel and single channel device.

Both figures depict a simple serpentine resistor configuration with traces that are 10µm wide. The Nominal Resistances for the single channel and multichannel temperature sensors are 35Ω and 42Ω respectively. As previously mentioned the single channel sensors are not laid out in the same pattern as the multichannel sensors. This is because it was feared that if the sensors were designed in the same manner, running in series along the length of the channel, that all visualization ability would be knocked out. So to combat this problem, the current crossing configuration was designed allowing for ample line of sight.

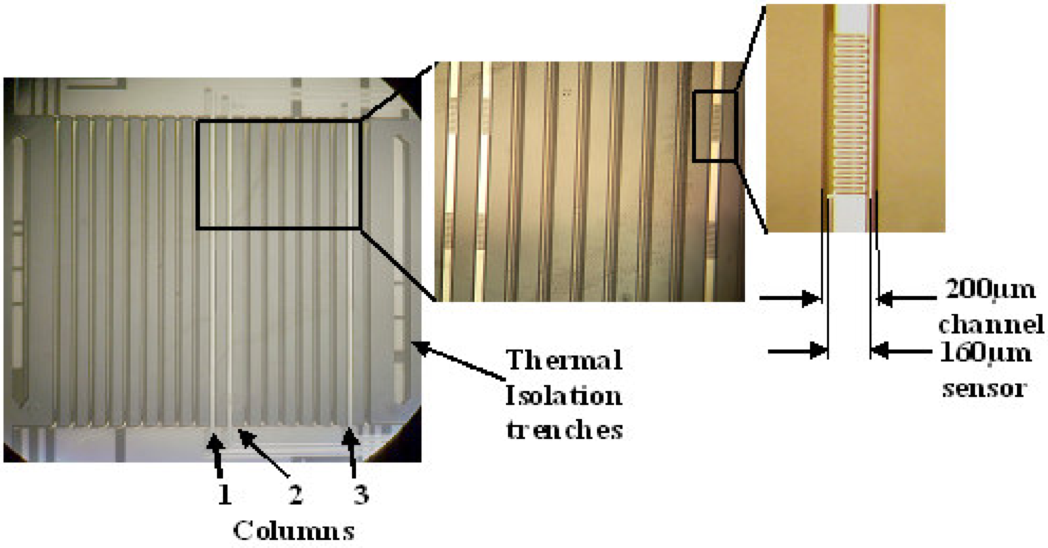

Figure 20: Temperature sensors in a multichannel test device.

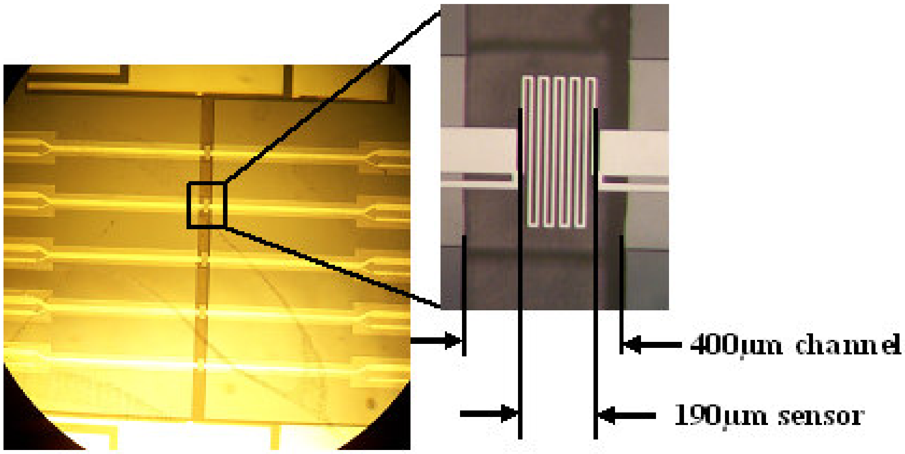

Figure 21: Temperature sensors in a single channel test device.

The platform for the temperature sensor fabrication was a 5-inch piece of Pyrex 7740 measuring 0.5mm thick. The sensors were fabricated by first using a photolithographic procedure to pattern the 10μm serpentine sensors directly onto the Pyrex surface. Next, a 0.4μm thick layer of pure aluminum is sputtered on top of the photo-resist pattern in the E-beam machine. Next a lift-off procedure is performed by submerging the specimen in a solvent that will eat the underlying photo-resist. The excess aluminum tears away from the intended pattern leaving the sensors and contact pads.

This top Pyrex cover plate is additionally outfitted with four holes for the inlet and outlet flow ports as can be seen in Figure 22 which is drilled after the sensor fabrication is complete. The 0.953-cm (0.375”) holes were drilled with a diamond tipped whole saw drill bit. To prevent breakage the Pyrex, the wafer is glued to a very large glass slab for rigidity. This was done by spinning photo resist on the back side of the Pyrex wafer. While the photo-resist is still wet, gently press the wafer against the glass slab and place in the oven to cure the photo-resist. After the drilling was complete the glass slab and wafer are set in a solvent solution used to break down the resist and the wafer was cleaned and prepped for bonding. The mask design and basic features are depicted in Figure 22 along with a completed test section for visual comparison.

Since the sensors are only 0.4μm thick, this gave considerable clearance for the sensor leads to exit the test section and would not cause any interference with the bonding process. The sensor lead routing and cutaway schematic are depicted in Figure 16.

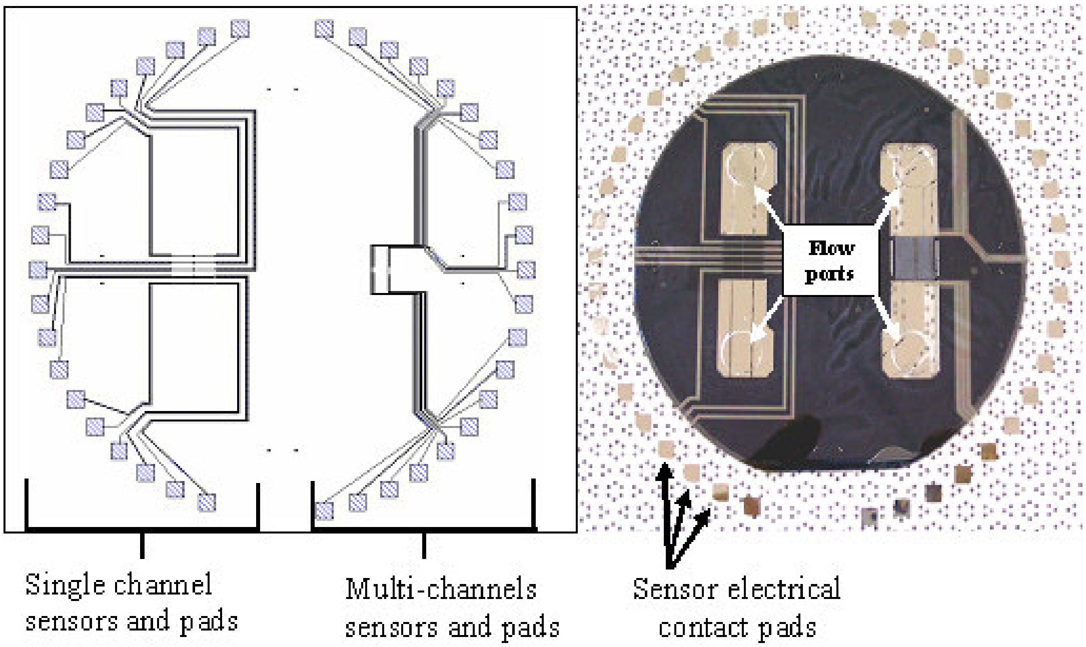

Figure 22: Mask design for temperature sensor configuration.

Following in Table 5, gives a step-by-step account of the major processes involved in the fabrication of the temperature sensors, leads and contact pads. This tabulation is a sequence that is pictured in Figure 23. Figure 23 (not to scale), is depicted from a general stand point and the features have no significance other than procedural interpretation.

1	Start with a 5” Pyrex 7740 wafer.
2	Photo-resist is deposited onto the wafer.
3	Photolithography patterning of sensors, leads and contact pads.
4	E-beam, sputter deposition of 0.4μm of pure aluminum.
5	Lift off procedure by soaking in solvent and removing the photo-resists underneath the unwanted areas of aluminum.

Table 5: Flow chart description for top Pyrex and sensor fabrication.

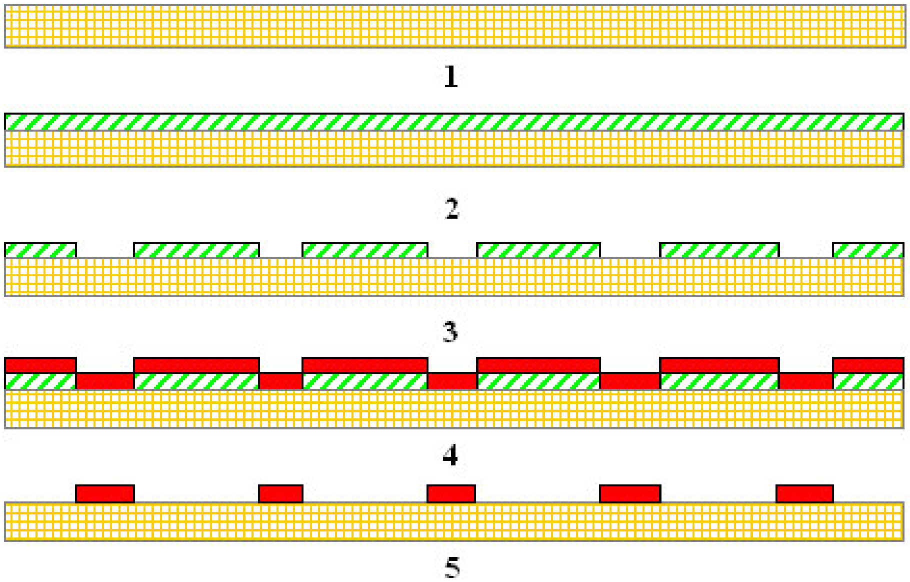

Figure 23: Temperature sensor fabrication flow diagram.

2.3.3 Bottom Pyrex and heater fabrication

The heaters used to simulate heat-generating electronics were fabricated on a 4-inch piece of Pyrex 7740, 0.5mm thick. This is achieved by first sputtering a 1μm layer of pure aluminum onto the Pyrex by placing it in the E-beam machine. Standard photolithographic procedures were used to pattern the serpentine heaters and contact pads on top of the deposited aluminum. The aluminum was etched using a PAE (Phosphoric Aluminum Etch) solution. This type of procedure as opposed to the lift off performed on the temperature sensors is less cumbersome. The PAE etch is very easy to perform but tends to undercut the aluminum a slight amount as most chemical etches do. This does not affect the design because of the large feature sizes involved and the small degree of undercut. Lift offs are typically performed on thin materials and very small feature sizes as seen in the temperature sensor fabrication.

Once the heaters were fabricated, a thin slice was cut off of each side of the wafer as seen at the top and bottom of Figure 24 using a dicing saw as to allow access to the silicon during the bonding process. The mask design and basic features are depicted in Figure 24 also, along with a completed test section for visual comparison.

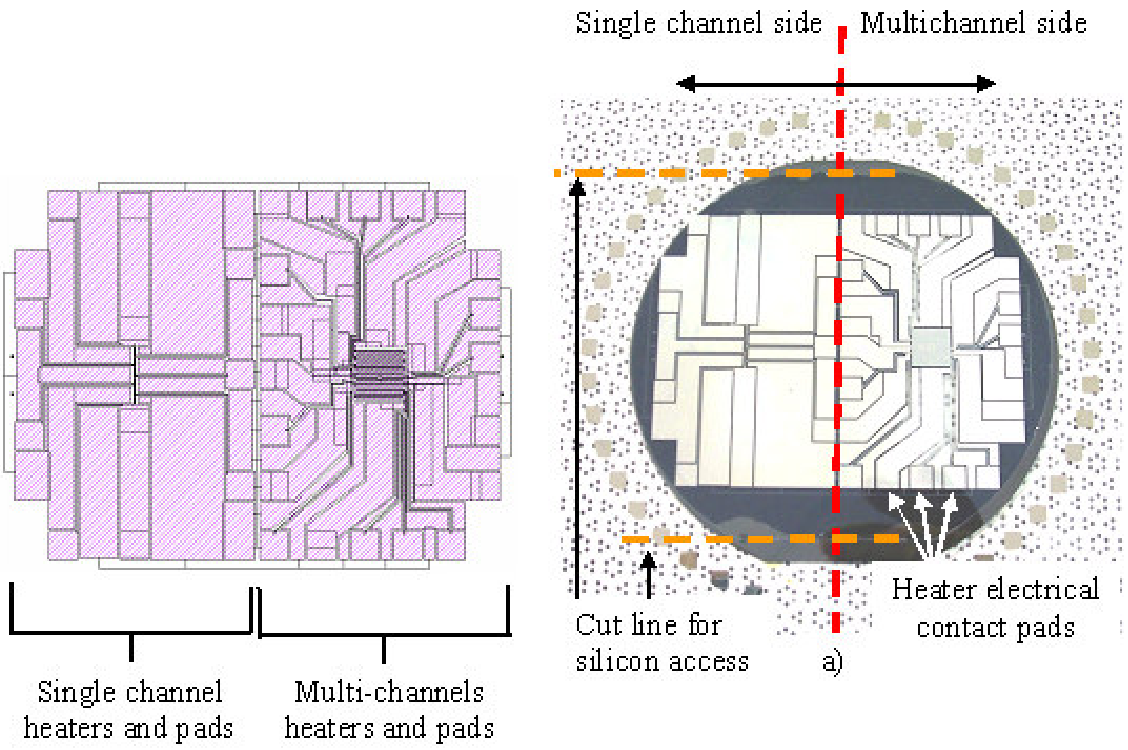

Figure 24: Mask design for heater configurations.

Following in Table 6, gives a step-by-step account of the major processes involved in the fabrication of the heaters and contact pads. This tabulation is a sequence that is pictured in Figure 25. Figure 25 (not to scale), is depicted from a general stand point and the features have no significance other than procedural interpretation.

1	Start with a 4” Pyrex 7740 wafer.
2	E-beam, sputter deposition of 1µm of pure aluminum.
3	Photolithography patterning of heaters, leads and contact pads.
4	PAE (Phosphoric Aluminum Etch) to remove unwanted aluminum
5	Pyrex wafer cleaned of photo-resist and PAE solution.

Table 6: Flow chart description for bottom Pyrex and heater fabrication.

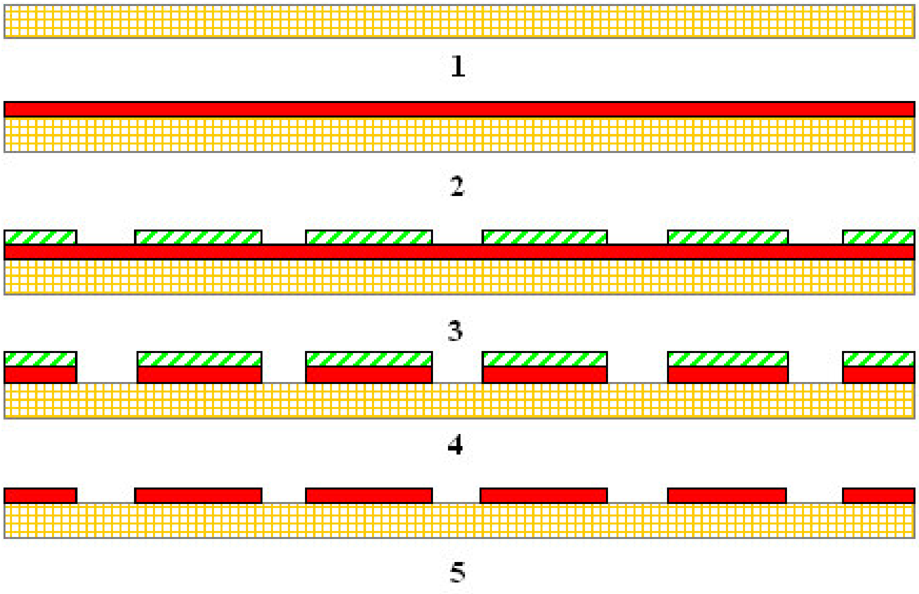

Figure 25: Heater fabrication flow diagram.

2.3.4 Alignment of specimens and anodic silicon-to-glass bonding

The bonding portion is one of the most critical stages of the fabrication. Bonding the two Pyrex pieces to either side of the silicon creates the sandwich structure shown in Figure 8. This configuration serves three major functions. The first is to seal the single channel and multi-channel configurations from the top and allow for channel flow visualization. The second is to seal the cavities from the bottom and third, since the silicon is etched all the way through on the inlet and outlet plenum areas, as previously mentioned, this bond serves to seal those regions from the top and bottom. Due to the low thermal conductivity of the glass, this design minimizes post- and pre- heating of the fluid in the test section, thereby permitting acquisition of more accurate data.

Before bonding the wafers together a rigorous cleaning process is conducted to remove all particles from the surfaces. Anodic bonding requires as perfect a surface as can be attained. After several chemical cleaning procedures to remove residues and organics, the wafers are set under a microscope and physically scanned for particles to remove. Figure 26 shows what happens when some particles are left on the bonding interface. As can be seen, the discolored or light circular areas are signature traits when a particle is trapped between the interfaces.

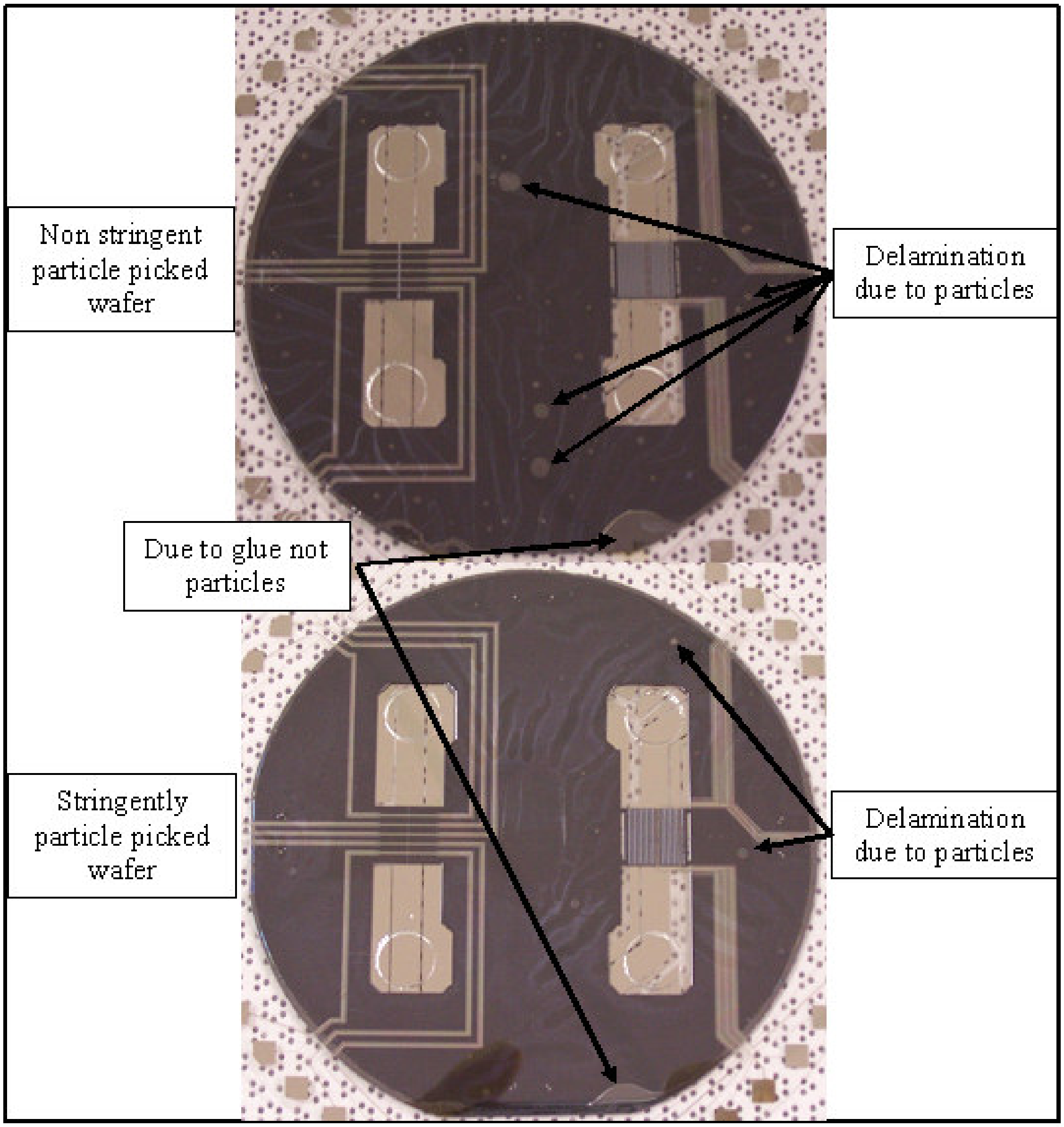

Figure 26: Delaminating silicon/glass due to particles left on bonding interface.

The wafers are then placed in a specifically fashioned jig as seen in Figure 27, which uses vacuum to hold the wafers in position. The jig is equipped with X,Y,Z translation as well as rotation in the Y plane. The top of the fixture is stationary and holds the Pyrex inverted by vacuum. This allows for viewing of the silicon through the transparent Pyrex by means of an overhead microscope. The bottom portion of the jig consists of an aluminum disk outfitted with vacuum ports to hold the silicon in place. This disk has translation as well as rotation that is made possible by the precision screws in the base of the fixture.

Once the Pyrex and silicon are mounted in position the vacuum valve is turned on. At the start of the process there is approximately a ½ inch gap between the interfaces. By looking through the microscope and using fabricated alignment marks (seen in Figure 28), the wafers are aligned to the intended configuration.

The alignment marks are very crucial when dealing with such tolerances. As seen in Figure 20, the alignment of the temperature sensors to the channel configuration had a tolerance of less than +/- 20μm. Each mask contains a series of squares and crosses as seen in the top of Figure 28. This is actually an image of all the alignment marks layered on top of one another. A pair of these marks was placed at the four corners of the design. Each set containing marks for bulk alignment and fine tuning.

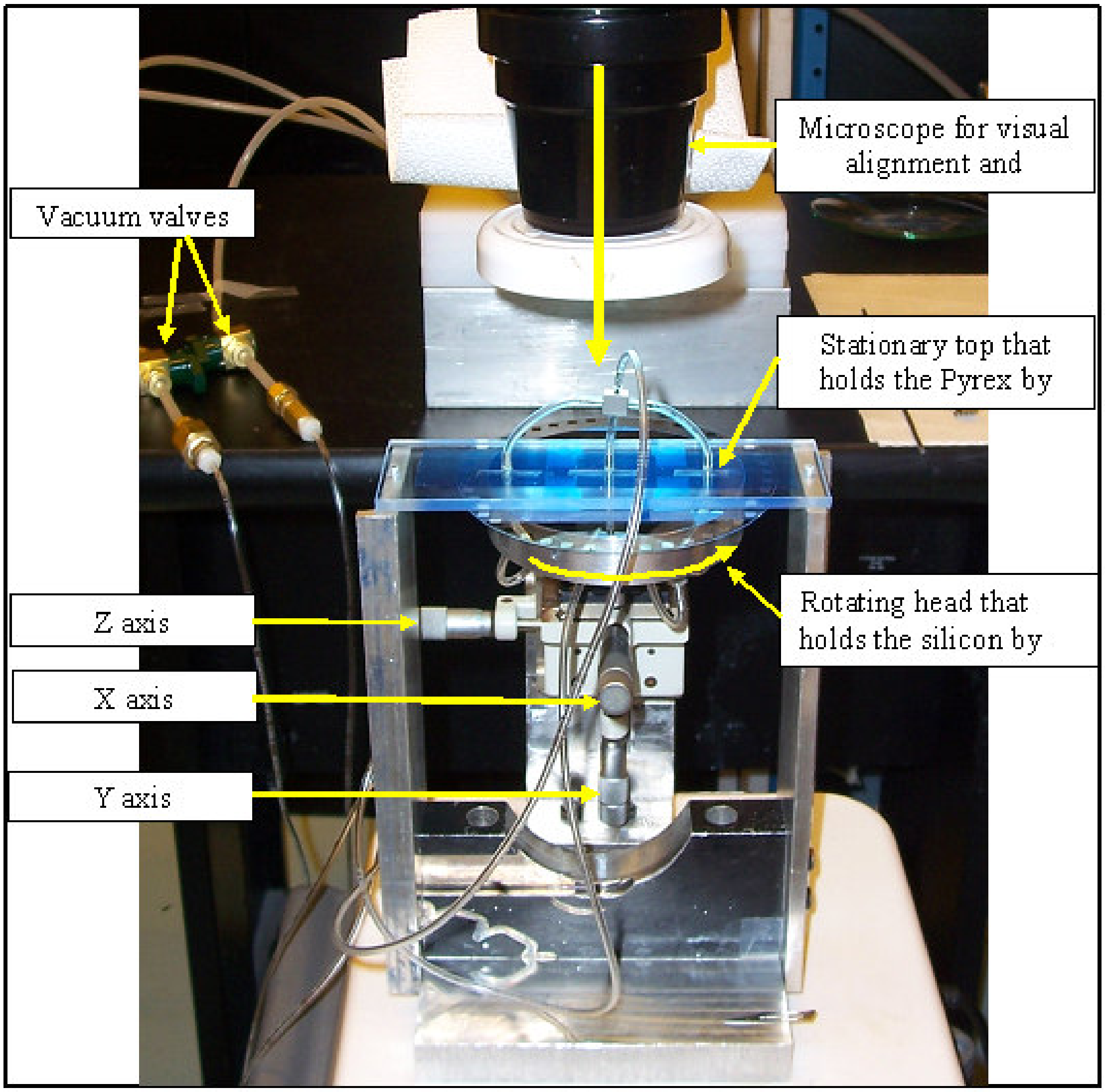

Figure 27: Wafer alignment jig and set up for alignment process.

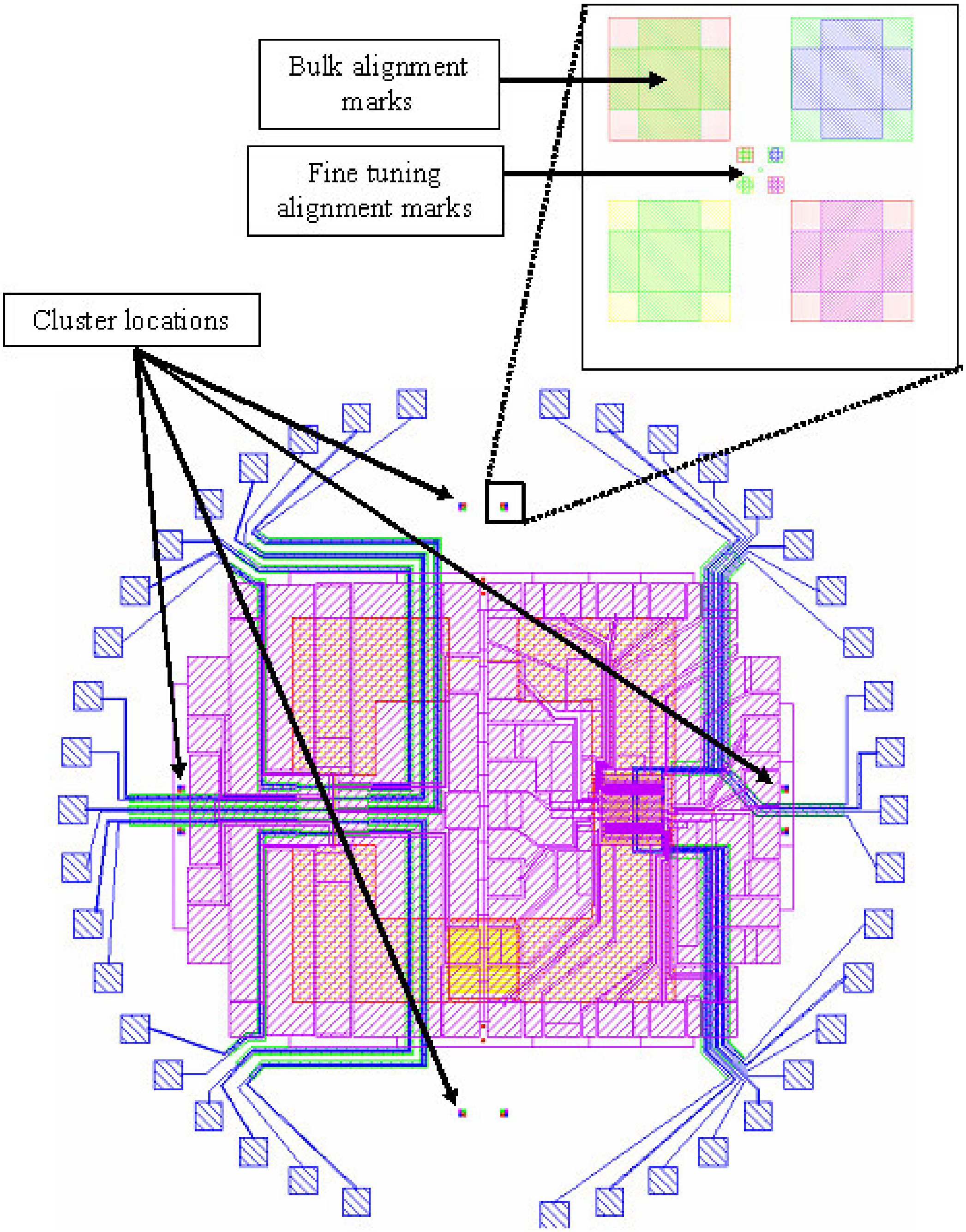

Figure 28: Specimen alignment mark configuration.

When the alignment of the specimen is complete and the Pyrex and silicon surface are physically mated, the wafers are glued at multiple corners for rigidity until the bonding process takes place. This glue is an optical adhesive meaning that once applied it must be subjected to intense ultraviolet light to cure. The glue is dabbed at the seam of the glass/silicon interface and allowed to wick its way in a small distance. A small intense UV light source is used to cure the glue by exposure through the Pyrex on top. Bonding effects of the glue can be seen as previously shown in Figure 26 by the curved delamination in the bottom right hand corner of both test sections. This glue is also used after the bonding procedure to seal the 5μm deep trenches used to get the temperature sensor signal leads out of the test section. A small portion of the adhesive is placed at the sensor lead exit of the test section and allowed to wick its way up the trench approximately 1/4”. It is then exposed to UV light for hardening thereby sealing the test section.

The bonding set up seen in Figure 29(a) consists of a hot plate, two ceramic plates (one wrapped in aluminum for the bottom cathode and the other used for an electrical insulator), the specimen sandwich structure, and an aluminum weight. This aluminum weight, machined smooth on the bottom surface, serves the purpose of a top cathode and to apply a mild amount of pressure during the bond. As mentioned previously the glass wafer containing the heaters had sections removed from its perimeter for access to the silicon during bonding. These allow the silicon to be positively charged by voltage probes.

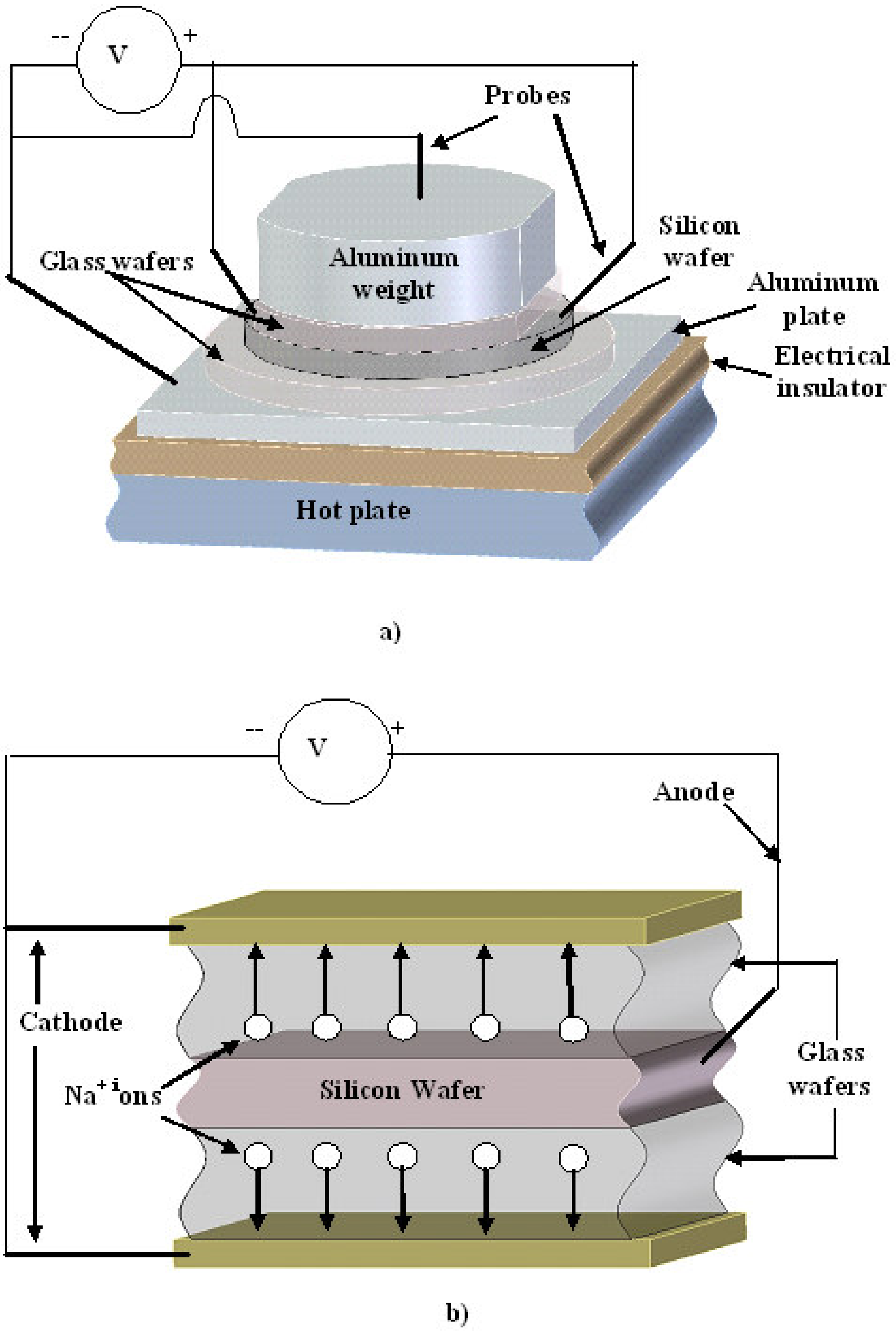

a)

b)

Figure 29: a) Schematic for anodic bonding layers and probe placement b) Detailed view of Na+ ion migration during bonding process.

The bonding procedure followed in this study, though slightly altered, came from a previous study by Nimkar, et al. [2004a]. This procedure began by heating the set up to 350°C which causes the Na+ ions in the glass to mobilize. The bond can easily take place at a range of temperatures from 300-400°C. Slow warming of the test section is important to prevent thermal shock to the glass or silicon. Once this state is achieved, a voltage of 650V is applied instantaneously. This voltage is held for 1 to 4 min. The applied voltage drives the Na+ in the Pyrex toward the negatively charged cathode as illustrated in Figure 29(b). This migration of the sodium away from the silicon to glass interface induced by the applied voltage causes a large bonding force between the two interfaces. A product of the bonding action is a visual measure of fringe lines in the glass. These fringe lines propagate away from the bonding area and continue doing so until the entire surface is bonded. As previously mentioned the test section is under these conditions for 1 to 4 minutes or until the fringe lines have ceased to move. It was found that the time it took to perform the bond was a strong function of how clean the wafer was. On a very clean wafer as depicted at the bottom of Figure 26, the bond happens almost instantaneously. Once the bond is complete the voltage is cut off and the test section is allowed to cool slowly.

2.3.5 Contact pads and device separation

After the bonding procedure is complete, the test section is covered with a shadow mask with is a rigid version of the lift off process performed on the temperature sensors. The shadow mask was constructed out of a thin copper sheet with holes punched in it that coincided with the spatial locations of the heater and sensor contact pads. This mask as depicted in Figure 30, is then taped to the bonded test section and placed in the E-beam where 5000A of aluminum, 6000A of nickel, and 500A of gold are deposited on all the contact pads for the heaters and temperature sensors. This process allows for wires to be soldered to the aluminum pads. The sandwich is then sawed in half as shown by the cut lines in Figure 24(a), separating the single channel device from the multi-channel device.

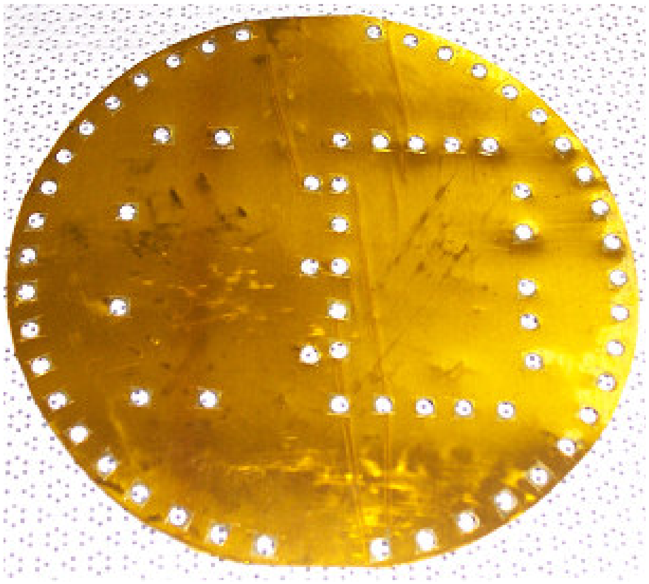

Figure 30: Shadow mask for contact pad deposition.

2.3.6 Wire soldering and gluing

After sawing the test sections into two different test sections the test sections are outfitted with wires soldered to the contact pads. These wires are aligned in a radial fashion as seen in Figure 31 for reasons of clamping that will be discussed later. Due to the stresses induced by the wires on the contact pads and their propensity for breakage, the wires are reinforced further by covering the joints with a nonconductive epoxy as seen in Figure 31. The final preparation of the test section before it is ready for testing is the attachment of the inlet and outlet ports. To avoid the stresses induced by hard mounting, the inlet and outlet ports are glued on as well using a urethane adhesive.

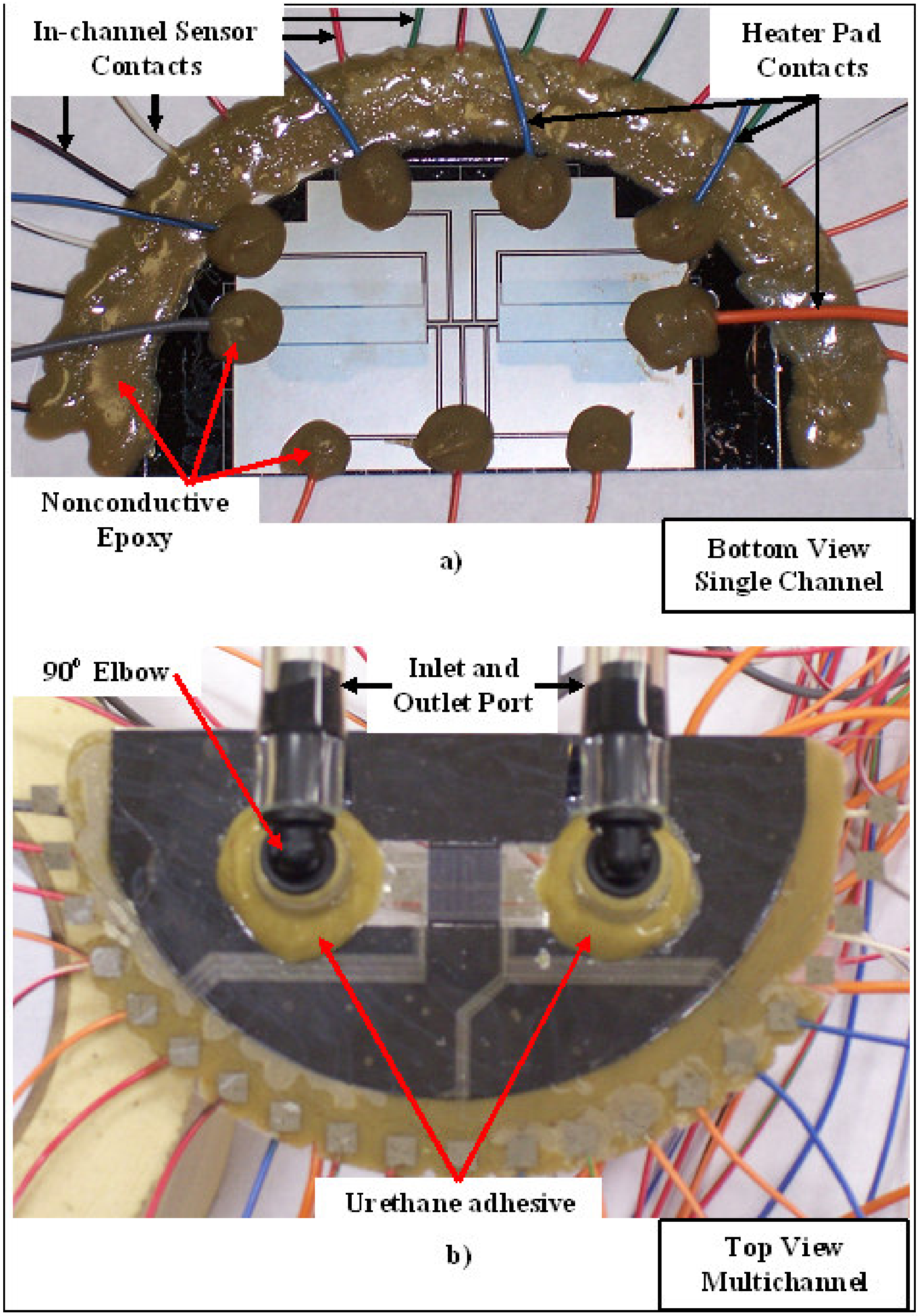

Figure 31: Gluing of wires and flow ports and relative position on test sections.

CHAPTER 3: FLOW LOOP AND CALIBRATION

3.1 Flow loop

3.1.1 Component description

All experiments in the current study were conducted using FC-72 at atmospheric exit pressure. The flow loop, as indicated in Figure 32, has the flexibility to permit experimentation over a range of pressures, heat flux, and inlet subcooling (degrees below saturation temperature). A MicroPump gear pump model# EW-07002 was used to achieve a controlled flow rate of between 25-100ml/min. The loop includes equipment such as thermocouples and pressure transducers placed at the inlet and outlet of the specimen flow. For visualization purposes, images of the flow were obtained with a Kodak Motioncorder model# 1000 high-speed camera. Fiberglass blankets were used to insulate the test section from the surroundings so as to reduce errors due to heat losses to the ambient. Upon completion of the data collection procedures, this blanket was removed to allow for visualization with the high-speed camera.

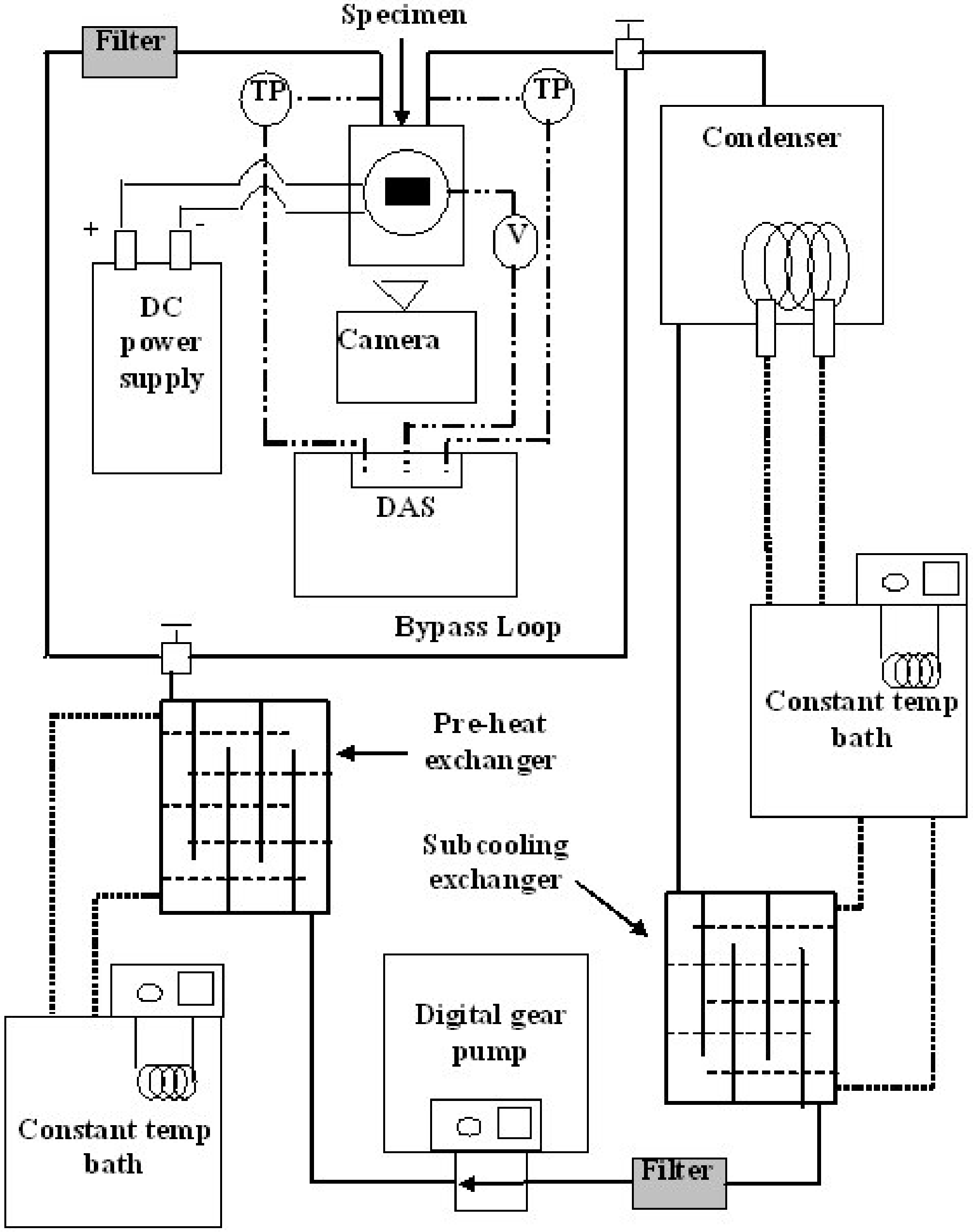

Figure 32: Flow loop showing instrumentation, flow visualization arrangement, and data acquisition equipment.

The condenser vessel was used for latent heat removal, degassing the liquid, and control of the system pressure. The pre-heater, a shell and tube heat exchanger, allows for precise control of the inlet temperature of the test specimen. The subcooling heat exchanger was used to remove sensible energy from the system, prevent the pump from cavitating, and allow experiments to be conducted for subcooled inlet conditions. The test section heaters are powered by a DC power supply with current measured by a digital multimeter. The voltage drop and current of the device heaters, the temperature sensor outputs, and the thermocouple and pressure transducer signals are all logged by a data acquisition system at 45 to 60 Hz for post-processing. Additional details on the flow loop can be obtained from a comparison thesis (Jones, 2006).

3.1.2 Wafer Jig

Due to the cumbersome task of handling the specimens themselves a specifically designed jig was fashioned. This jig had to incorporate the firm, but not rigid, constraint of the 30 some odd wires protruding from the specimen as well as access to those wires, allow the tubing access of the inlet and outlet ports, the firm, but not rigid, constraint of the tubing leaving the specimen to prevent stress on the ports, not interrupt visibility, and allow for the specimen to be insulated from both sides. Figure 33 depicts the design with a specimen in the jig. It is constructed out of Plexi glass for ease of machining and visibility.

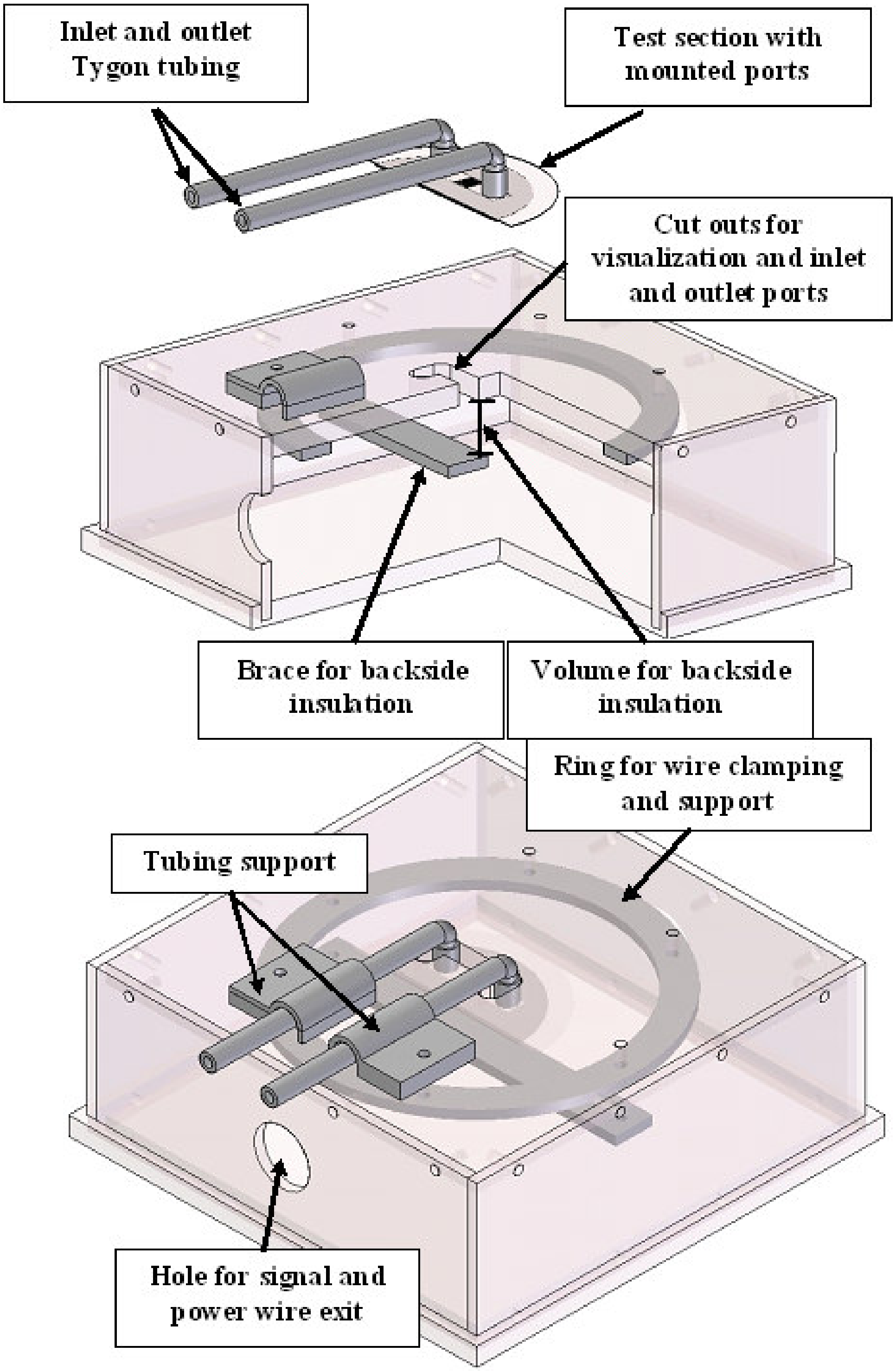

Figure 33: Cut away view of Specimen Jig and relative supports.

3.2 Calibration of equipment

Sensors requiring calibration are the inlet and outlet thermocouples, inlet and outlet pressure transducers, gear pump, temperature sensors inside the channel flow, and the heaters on the backside of the specimen. All these sensors were calibrated using standard procedures, except for the heaters due to a series of mishaps and failures. The following is a chronological layout of the events and measures taken to successfully calibrate the heaters.

3.2.1 Calibration Fixture

The initial attempt was an effort to calibrate both the in-channel sensors and the heaters at the same time. Heaters on the current tests sections are expected to exceed 400°C based on design calculations. This poses a large problem in calibration due to the fact that the solder, glue and wire insulation will not stand up to these extreme temperatures for calibration to take place.

With these factors in mind the current study attempted to calibrate the heaters and sensors locally up to 400°C while leaving the rest of the test section exposed to ambient conditions. Figure 34 depicts the basic concept. By imposing a symmetric, equal temperature on both sides of the test section with a foot print marginally larger than the heater pad and sensor array, it is inferred and verified by FEA that the three dimensional temperature gradients within that foot print area are negligible and the sensors can be assumed to be the same as the two outside imposed temperatures.

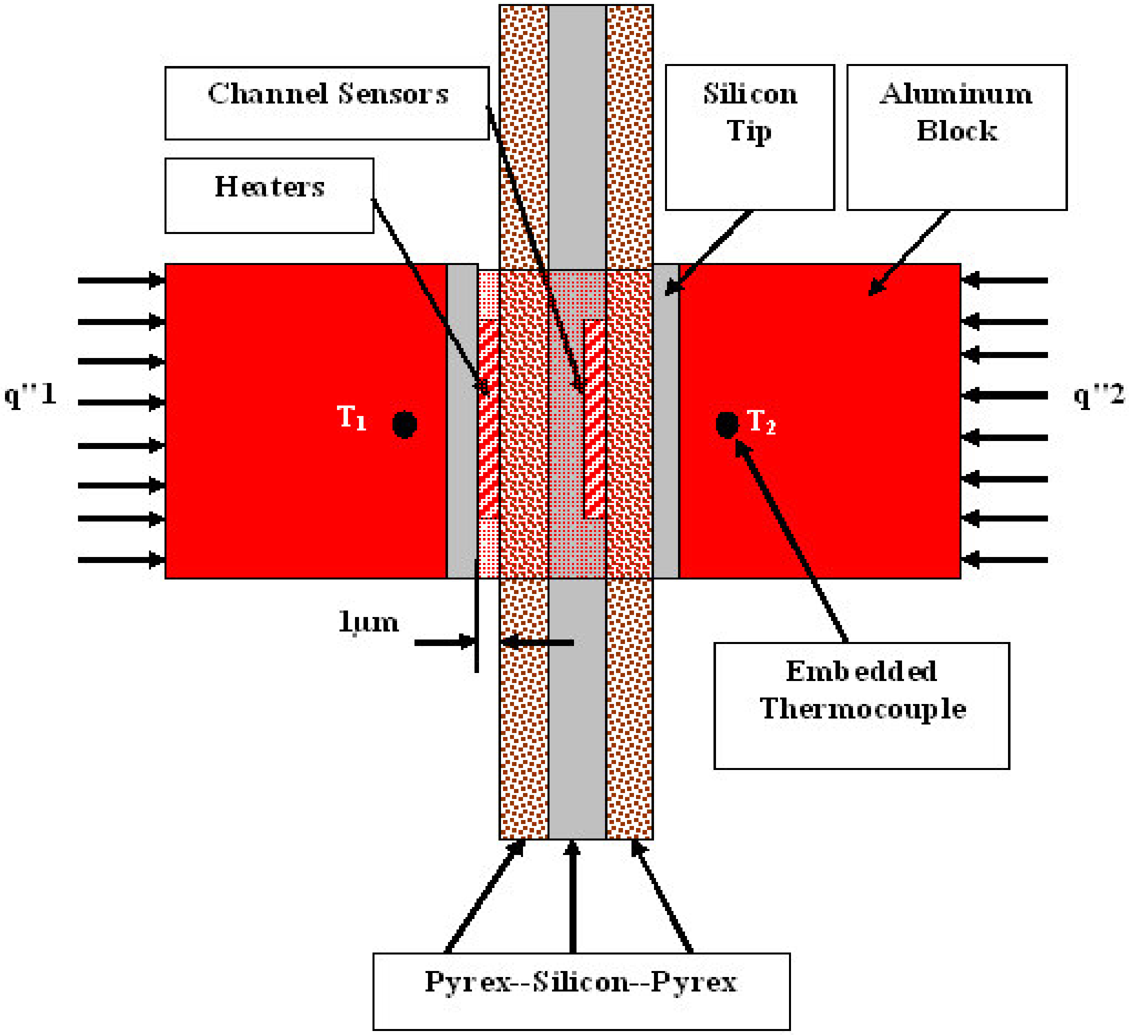

Figure 34: Schematic of Calibration Fixture principle.

This is made possible by the extremely low thermal conductivity of the Pyrex that sandwiches the silicon. With an imposed temperature at the center of the test section, the radial temperature gradient is large enough to keep the wires, solder joints, and glue at an acceptable temperature.

The two aluminum blocks on either side of the test section contain a cartridge heater in each to modulate q"1 and q"2. These are varied until T1 and T2 thermocouple outputs are the same. Prier to calibration the thermocouples are themselves calibrated against a thermistor in a constant temperature bath. The tips of the aluminum blocks are also outfitted with a square silicon chip with a polished surface as seen in Figure 34. The silicon is attached to the aluminum using a high thermal conductive epoxy. This serves two purposes, to reduce contact resistance by using a polished surface and to serve as an electrical insulator between the heaters and the aluminum block. This procedure is repeated from 25-400^{o}C. A picture of the setup is displayed in Figure 35 and is followed by data collected from multiple tests.

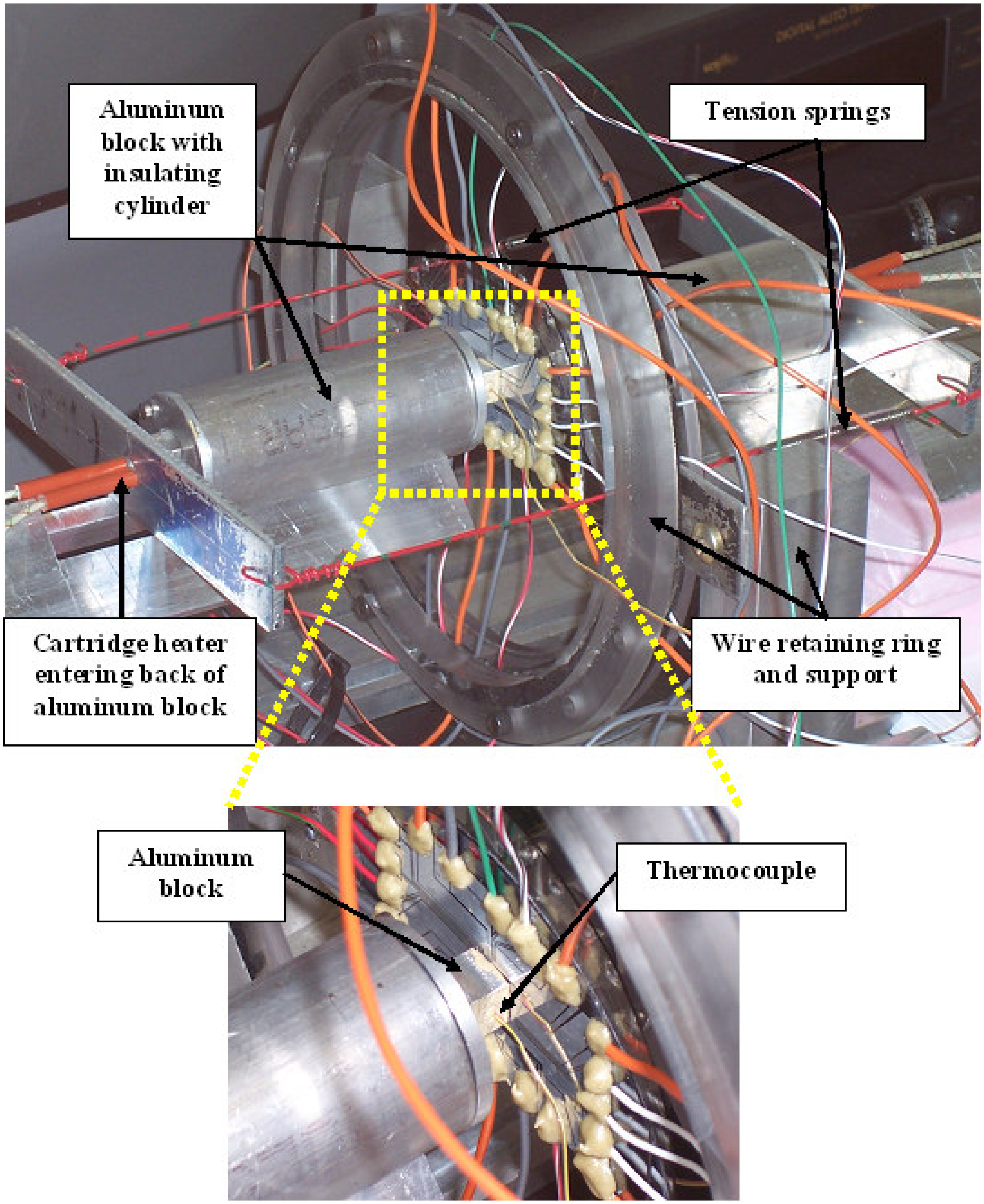

Figure 35: Calibration Fixture.

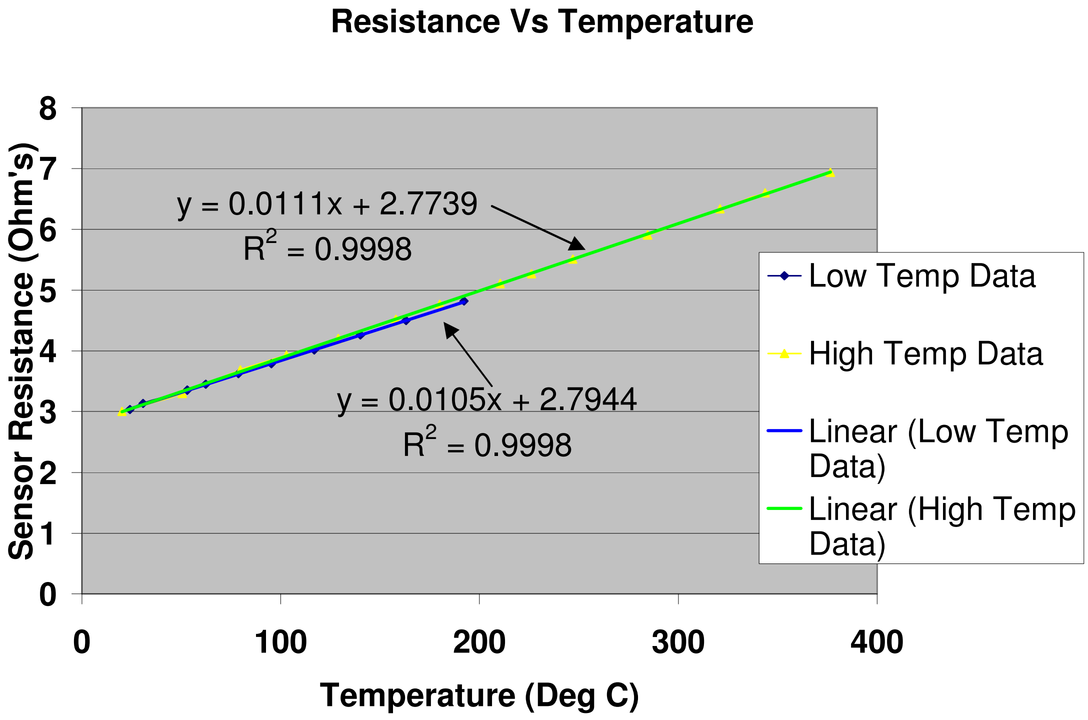

Figure 36: Plot of data collected from the Calibration Fixture.

Figure 36 shows the data curve for a single heater/sensor on two different calibration tests. The slight deviation of the curves was typical of all the sensors and is attributed to misalignment of the heaters with the test section. This problem was overcome by placing tension on the two heaters using two springs as seen in Figure 35. After several tests were conducted on a preliminary test section (not one of the eight good test sections), it was decided to abandon this calibration method due to no repeatable results and fear of scratching the test sections aluminum heaters while setting up the calibration fixture.

This method did however provide confirmation that the aluminum resistance-to-temperature relationship is quite linear over a large range. With this in mind a lower temperature method is sought with the intent of defining a lower range curve and extrapolating past the calibrated range.

3.2.2 Calibration by constant temperature bath

The second attempt was also an effort to calibrate both the in-channel sensors and the heaters at the same time. This was done by placing the specimens in a zip-lock bag, placing a calibrated thermistor inside the bag next to the test section and submerging them into a constant temperature bath. The resistance of the heaters and sensors are correlated against thermistor temperature over a range of 20 to 85^{o}C. This range is sufficient for the channel sensors since the atmospheric boiling point of FC-72 is 56.6^{o}C, but for the heaters that are expected to exceed 400^{o}C, extrapolation of the curve will be necessary. Following is a listing of calibrations performed and problems encountered.

- [Single Channel, 100µm wide, 2 cavities per channel]: all inflow sensors damaged during fabrication except for one of the five, heaters calibrated successfully. Single channel sensor lost signal during calibration.
- [Single Channel, 100µm wide, 6cavities per channel]: all inflow sensors are working prior to calibration. Halfway through calibration, all channel sensors lose signal. After removing the specimen, a thorough examination revealed a crack that propagated along the silicon to sensor glass interface as portrayed in Figure 37. This crack was over looked on the initially tested specimen. It was believed the stirring mechanism on the constant temperature bath was inducing a hydrodynamic stress on the specimen. The bath was altered to redirect the flow before any further calibration is conducted.

- [Multichannel, 200µm wide, 6cavities per channel]: all inflow sensors are working prior to calibration. Half way through calibration all channel sensors loose signal. Having removed the possibility of hydrodynamic induced stress, the cause is now pointed to thermal stress of the joint possibly caused by the nonconductive epoxy placed in a radial application around this joint as seen previously in Figure 31.

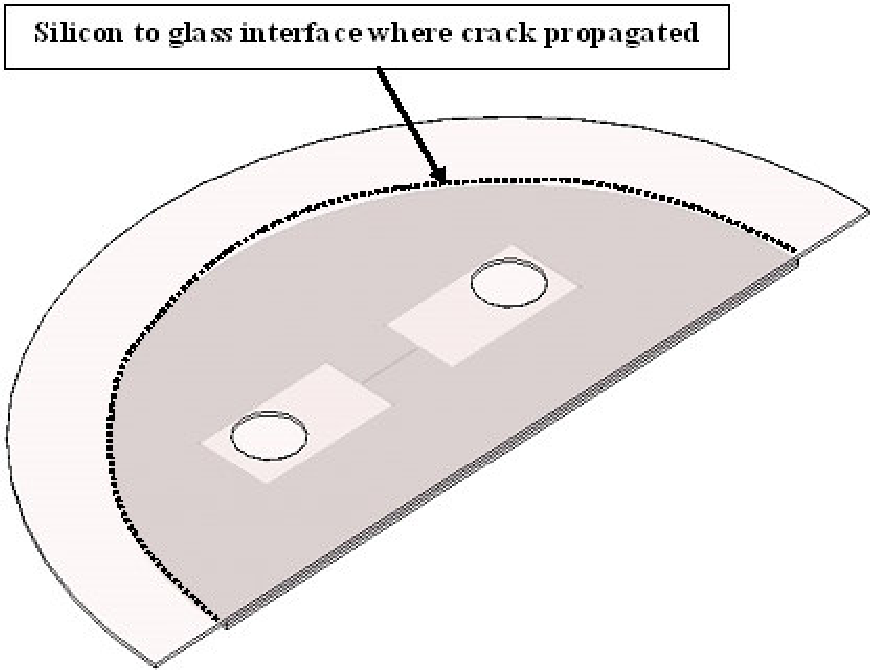

Figure 37: Display of Crack propagation on test sections.

To clarify the situation, the three test sections just mentioned are still functional. The heaters and the rest of the test section is unscathed by the damage imposed. Only the in-channel temperature sensors were damaged. At that point, due to all eight of the test sections having been wired up and glued in the same fashion, alternative means of calibration were sought.

3.2.3 Calibration by material constant alpha

The method of calibration proposed in this section is what was ultimately used for the test section heaters. The method of calibration for the in-channel sensors will be discussed following this section. With previous failures in mind, a method of calibration was developed based on a material property and the linearity of the materials resistance change with temperature. This method, along with calibration data from the three damaged specimens and the one trial specimen allows calibration of the heaters without exposing them to harmful conditions.

Figliola and Beasley [2000] proposes Equation 2 which is a linear equation solving for resistance by knowing the values of R_o, T_o, T_h, and α. R_o and T_o are pre-selected values recorded under controlled conditions and A is the material dependent temperature coefficient. As can be seen, this equation can easily be re-arranged to solve for T=f(R).

$$R_h(T) = R_o\left[1+\alpha(T_h - T_o)\right] \tag{2}$$

This relationship can be solved by taking the linear equation as seen below and combining the boundary condition of (R_h=Ro, then T_h=To).

$$T_h = m_c \cdot R_h + b_c \tag{3}$$

After boundary condition application and algebraic manipulation the equation takes the form of the following.

$$R_h = R_o\left[1 + \frac{(T_h - T_o)}{m_c \cdot R_o}\right] \tag{4}$$

This implies that the value of (α) can be solved by the following.

$$\alpha = \left[\frac{1}{m_c \cdot R_o} \right] \tag{5}$$

The heaters from the three damaged specimens and the one trial specimen are then calibrated in the constant temperature bath using a thermistor as the standard. This data is then plotted in the form of Equation 3 and the slope (m_c), R_o, and T_o values recorded. The value of (α) is found for every heater and averaged to a value of 0.0036039. Several texts had a standard value for pure aluminum of 0.0042. The differences between these values are attributed to things such as oxidation of the aluminum which is accelerated at high temperatures, impurities imbedded during aluminum deposition, and experimental error. All the test section underwent similar if not the same fabrication procedures so it is inferred that the averaged value of (α) is applicable to the rest of the test sections that did not go into the formulation of (α).

This method allows the current study to place a given specimen that has not been calibrated into a constant temperature bath, where the values of Ro and To are recorded for every given heater. Using these values, Equation 2 solved for (T) and the value of (α) gathered experimentally from the four test sections, the temperature of the heaters can be gathered as a function of resistance.

3.2.4 Calibration of in-channel sensors

The calibration of the in-channel sensors is started by first connecting the test section up to the flow loop. The inlet and outlet thermocouples were calibrated in a constant temperature bath against a thermistor. The flow was initiated and the sensors were connected to the data acquisition system. The pre-heat exchanger, as seen in Figure 32, is used to modulate the fluid temperature. Every increment in temperature is followed by a generous amount of time to allow any transients to die out before the resistance of the sensor is recorded. Since the sensors are in direct contact with the fluid, the average of the two thermocouples is used as the sensor temperature at that given point. This procedure is continued over a range of 25-60°C. It was felt that this range was adequate due to the low boiling point of the working fluid.

3.2.5 Uncertainty of equipment and sensors

A detailed uncertainty analysis is in Appendix D. The uncertainty of the current and voltage measurements is ±1.1mA and ±4.3mV respectively based on manufacturers specifications. The combination of these two components yields a power uncertainty of ±0.404% at maximum power output. The K-type thermocouples employed were calibrated to an uncertainty of ±0.65°C using a constant temperature bath and a thermistor as the standard. The pressure transducers were calibrated using a piston type dead weight tester to an uncertainty of ±0.33% of full scale. The gear pump was calibrated to a maximum error of ±1.47% of the total flow. The fluid, which has a strong affinity for non-condensable gases, was de-gassed extensively and the dissolved gas content was monitored using an Aireometer, yielding gas contents at were less than 1% by volume. The value of heater temperature (T_h), is calculated by using the average heater resistance as a function of temperature. This relationship was calibrated to an uncertainty of ± 5.64°C. The in-channel sensors are calibrated as previously explained to an uncertainty of ± 1.03, 0.81, 1.15, and 2.63°C respectively.

3.3 Heat Loss Calculations

To quantify the heat loss during the experiments the following procedure was fallowed. It should be noted that the current study developed two different methods of calculating heat loss. The first will be referred to as Method 1 and is a more conservative approach. The second will be referred to as Method 2 and is believed to be more accurate but less conservative. The effect of which method is used in data analysis greatly affects the results of silicon temperature profile, heat transfer coefficient, and quality calculations. These differences will be discussed in the results chapter of this thesis.

3.3.1 Major modes of heat loss

Generally speaking, there are three major modes of heat loss associated with the current design configuration. Quantification of them individually would be very difficult due to geometry and varying parameters such as flow and heat flux. These modes are laid out as follows.

1. Losses directly from the back side of the specimen into the insulation which eventually reaches ambient by convection.
2. Losses from the inlet and outlet tubes due to the inlet fluid temperature being higher than ambient. This is a fixed value for a fixed flow rate.
3. Additional losses in the exit line due to an increase in exit fluid temperature resulting from the input heat at the test section.

3.3.2 Heat loss quantification

The following portion of the calculations is used in both methods of heat loss analysis. The overall power supplied to the test specimen is calculated by:

$$P_{in} = I^2 R_h \tag{6}$$

Heat loss is quantified by first taking the sensible heat transfer data from each tested flow rate. While in the single-phase portion of the experiment this is calculated by:

$$q_{sp} = \dot{m} C_p \left(T_{out} - T_{in} \right) \tag{7}$$

Properties are taken at the average between the inlet and outlet thermocouple readings. The heat loss to the ambient air is calculated by taking the difference between Equation 6 and Equation 7.

$$q_{loss} = P_{in} - q_{sp} \tag{8}$$

3.3.3 Heat Loss Method #1

As previously mentioned, Method #1 is a more conservative approach. It assumes that all three modes of heat loss that are quantified by Equation 8 are lost from the back side and that none of the lost heat travels through the Pyrex to the silicon. This basically implies that heat loss mode #1 is the dominant of the three modes. Once this assumption is made the losses are plotted as a function of the difference between heater temperature and ambient temperature (T_h-T_{amb}). Figure 38 displays a resistance network for Method #1's heat flow.

$$q_{loss} = m_l \left(T_h - T_{amb} \right) + b_l \tag{9}$$

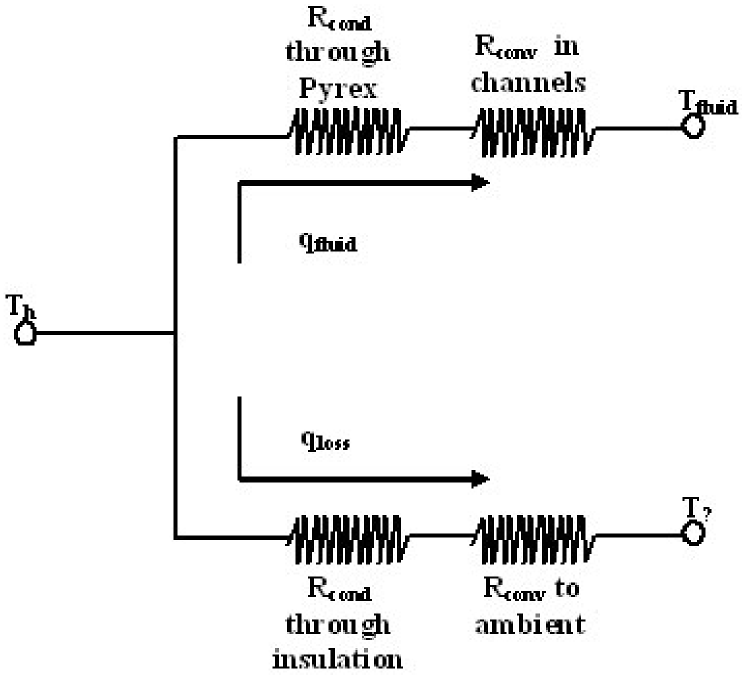

Figure 38: Thermal resistance network for Heat Loss Method #1.

3.3.4 Heat Loss Method #2

Calculation of heat losses in small geometries is an extremely difficult task. Studies reported in the literature seem to either use HLM1 or some similar approximate method. The following paragraphs are an effort to improve on existing efforts. As previously mentioned, Method #2 is a less conservative approach. It assumes that all three modes of heat loss that are quantified by equation 8 are lost from the system at their own specific locations unlike Method #1. Results from this method imply that heat loss modes #2 and #3 are the dominant modes and that mode #1 is present but minor in magnitude. Figure 39 displays a conceptual diagram for Method #2's heat flow where $q_{loss\text{-}1}$= mode #1, $q_{loss\text{-}2}$= mode #2, and $q_{loss\text{-}3}$= mode #3.

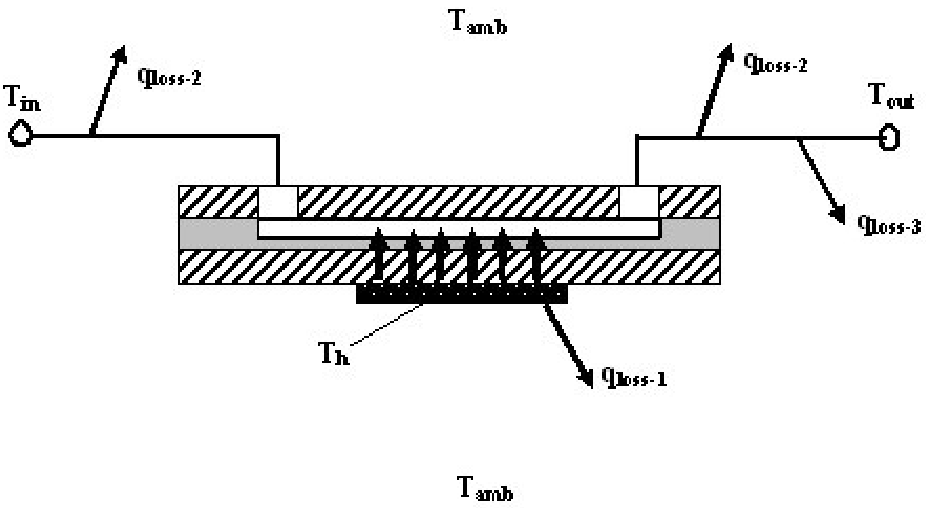

Figure 39: Heat loss paths for Heat Loss Method #2.

Method #2's concept is built around the value of q_{loss} that is quantified in Equation 8 being a function of three separate temperature differences and being weighted accordingly [$q_{loss} = f(\Delta T_h, \Delta T_f, \Delta T_{in})$]. The values of ΔT_h, ΔT_f, and ΔT_{in} are quantified as follows.

$$\Delta T_h = T_h - T_{amb} \;:\; \Delta T_f = T_{out} - T_{in} \;:\; \Delta T_{in} = T_{in} - T_{amb} \tag{10}$$

The overall function for the loss takes the form of Equation 11 and can be broken up into its individual components as seen below.

$$q_{loss} = a\Delta T_h + b\Delta T_f + c\Delta T_{in} \tag{11}$$

$$q_{loss-1} = a\Delta T_h \;:\; q_{loss-3} = b\Delta T_f \;:\; q_{loss-2} = c\Delta T_{in} \tag{12}$$

The first step in solving for the coefficients a, b, and c are developing relationships such as $\Delta T_f = f(\Delta T_h)$ and $\Delta T_{in} = f(\Delta T_h)$ as seen in Equations 13 and 14. These relations are linearly fit to obtain the values of d, e, f, and g. These relations are then substituted into Equation 11 to produce Equation 15. At this point, ΔT_h is plotted against q_{loss} from Equation 8 and linearly fit to produce the slope and y-intercept values of q and r which are represented in Equations 16 and 17.

$$\Delta T_f = d\Delta T_h + e \tag{13}$$

$$\Delta T_{in} = f\Delta T_h + g \tag{14}$$

$$q_{loss} = \Delta T_h \left(a + bd + cf\right) + \left(be + cg\right) \tag{15}$$

$$q = \left(a + bd + cf\right) \tag{16}$$

$$r = \left(be + cg\right) \tag{17}$$

This procedure is repeated in Equations 18-27 for $q_{loss}= f(\Delta T_f)$ and $q_{loss}= f(\Delta T_{in})$.

$$\Delta T_h = h\Delta T_f + i \tag{18}$$

$$\Delta T_{in} = j\Delta T_f + k \tag{19}$$

$$q_{loss} = \Delta T_f \left(ah + b + cj\right) + \left(ah + ck\right) \tag{20}$$

$$s = (ah + b + cj) \tag{21}$$

$$t = (ah + ck) \tag{22}$$

$$\Delta T_h = l\Delta T_{in} + m \tag{23}$$

$$\Delta T_f = n\Delta T_{in} + p \tag{24}$$

$$q_{loss} = \Delta T_{in}(al + bn + c) + (am + bp) \tag{25}$$

$$u = (al + bn + c) \tag{26}$$

$$v = (am + bp) \tag{27}$$

Once this portion of the analysis is done it renders the system with six equations and three unknowns. Equations 16, 17, 21, 22, 26, and 27 are the six equation and a, b, and c are the three unknowns. A system of equations such as this can render a total of twenty mathematically possible solutions but as the current research found, only one of them made logical sense. The values of a, b, and c should all be non-zero and positive. With these two criterions in mind, the coefficient sets of a, b, and c are selected from one of the twenty mathematical possibilities.

As previously mentioned Method #2 says that most of the heat is lost from mode #2 and #3 which indicates that the dominant heat flow path is through the Pyrex and into the fluid as it should. This makes a significant difference in the calculated silicon base temperature due to the extremely low thermal conductivity of the Pyrex. Once the heat loss curves were generated for the single-phase data, extrapolation past the plotted range of the linear fit was necessary to quantify losses for the two-phase portion of the experiments.

CHAPTER 4: RESULTS AND DISCUSSION

3.4 Introduction

The present study attempts to quantify the heat transfer characteristics of two out of the eight microchannel test sections produced. The selection of the two test sections was due to the failure of the in-channel temperature sensors on the 200-6 test section during calibration and a heater failure on the 400-2 test section during the first test run. The test section notation of 200-6 and 400-2 is explained in Table 3 shown earlier in section 2.2 and represents [nominal channel width]-[# of cavities per channel]. Therefore, the two specimens discussed in detail in this chapter are the 200-2 and the 400-6 test sections. Initially the quantitative differences between Heat Loss Method #1 (HLM1) and Heat Loss Method #2 (HLM2) will be detailed for these test sections in a variety of ways. Eventually results will only be displayed using HLM2 after presenting information supporting its use. This approach will be backed up by an FEA analysis in Section 4.5.

The independent variables in this study were heat flux, flow rate, channel size, gas content of the inlet fluid, and the number of cavities per channel. Several other independent variables such as subcooling will be described in a companion thesis (Jones, [2006]). All experiments discussed in this study use FC72 as the working fluid and have a constant inlet temperature of 47^{o}C (10^{o} of subcooling) which is based on the ambient saturation temperature of FC72. Also the exit pressure of the test section for every experiment was maintained at atmospheric.

The dependent variables presented in this study are heater temperature, in-channel sensor temperature, fluid outlet temperature, pressure drop, and single-phase and two-phase heat transfer coefficients. This chapter presents qualitative as well as quantitative effects.

3.5 Discussion of Boiling Curve Results

The boiling curve is a typical graphical measure of boiling activity. The general characteristics of these curves are described in Section 1.2 and Figure 2. The components seen in most of the plots in this section are the inlet and outlet thermocouple measurements and T_{wall}, the calculated base temperature of the channels. The calculation of T_{wall} depends on the heat loss method used. As will be seen in the next section, this decision of which heat loss method to use will cause a significant difference in the values of T_{wall} and the overall shape of the boiling curve.

T_{wall} is calculated by subtracting some value of heat loss from the overall power input as seen below in Equations 28 and 29. Equation 28 is for HLM1 and Equation 29 is for HLM2.

$$q_{wall} = P_{in} - q_{loss-total} \tag{28}$$

$$q_{wall} = P_{in} - q_{loss-1} \tag{29}$$

1-D conduction is used as shown in Equation 30 to quantify the value of T_{wall}.

$$T_{wall} = T_h - \left[\frac{t_p}{k_p} + \frac{t_{si}}{k_{si}} \right] \frac{q_{wall}}{A_{array}} \qquad (30)$$

Due to the extremely low thermal conductivity of the Pyrex glass that the heat must conduct through, the value of q_{wall} and the method by which it is calculated will greatly affect the value of T_{wall}.

4.2.1 Effect of flow rate on boiling curves

The test sections and flow loop of the current study were designed to accommodate a wide range of heat input and flow rates. Figures 40-44 show the effect of flow rate on the boiling curve for three different values of mass flux. Figures 40-42 also individually show the difference between HLM1 and HLM2 for those flow rates and the inlet and outlet thermocouple data. As previously mentioned all the experiments discussed were conducted at 10°C sub-cooling which is displayed in Figures 40-42 by the vertical data on the left hand side of each plot. The outlet thermocouple is also displayed to give indication of reaching the saturation point illustrated by a sloped increase, then settling on a vertical path. Increasing the flow rate results in a higher heat input to attain a saturated exit; this is also displayed by a steeper curve for the outlet thermocouple data over all three figures.

The boiling curves displayed in Figures 43 and 44 show only the values of T_w for all three flow rates for HLM1 and HLM2. Both these plots show the quantitative effect of an increase in flow rate by the leftward shifting of the curves. This is especially evident in the linear single phase portion of the curves. It is also quite evident that the flow has an effect on the two-phase portion of the curves, specifically shown in Figure 44 by the case for 535 kg/m^2-s and its deviation from the other two sets of data.

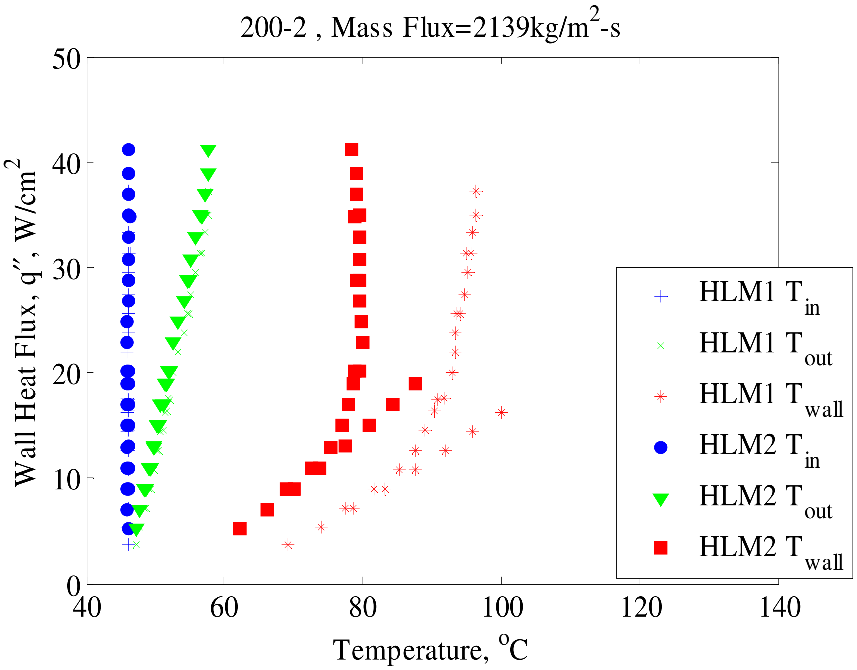

Figure 40: Flow boiling curve for specimen 200-2 at a mass flux of 2139 kg/m^2-s displaying the difference between HLM 1 and 2.

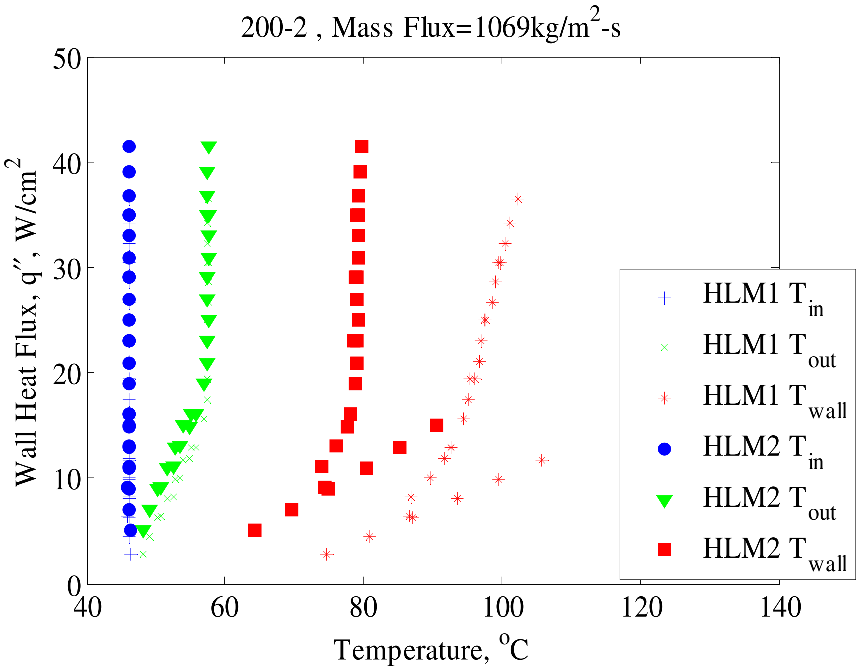

Figure 41: Flow boiling curve for specimen 200-2 at a mass flux of 1069 kg/m^2-s displaying the difference between HLM 1 and 2.

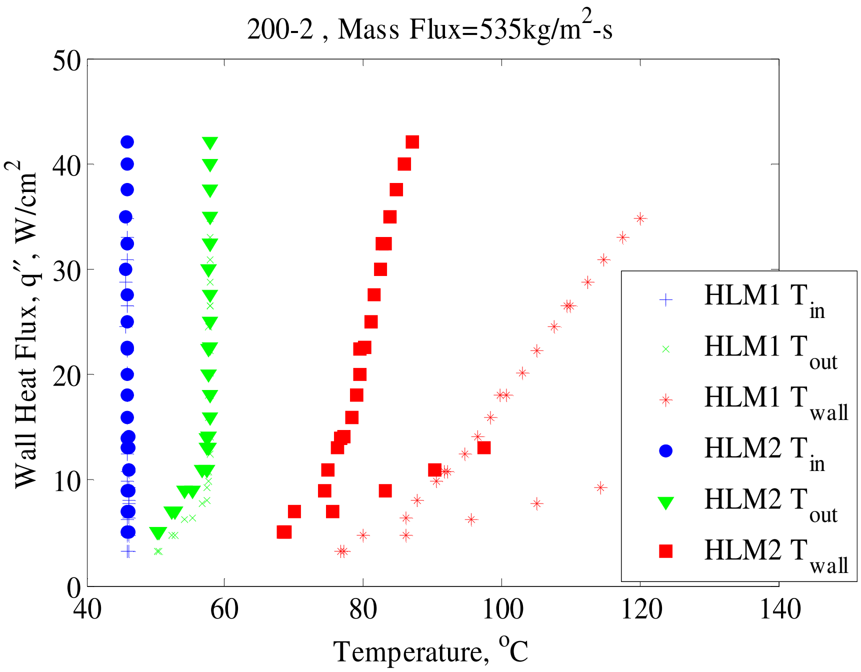

Figure 42: Flow boiling curve for specimen 200-2 at a mass flux of 535 kg/m^2-s displaying the difference between HLM 1 and 2.

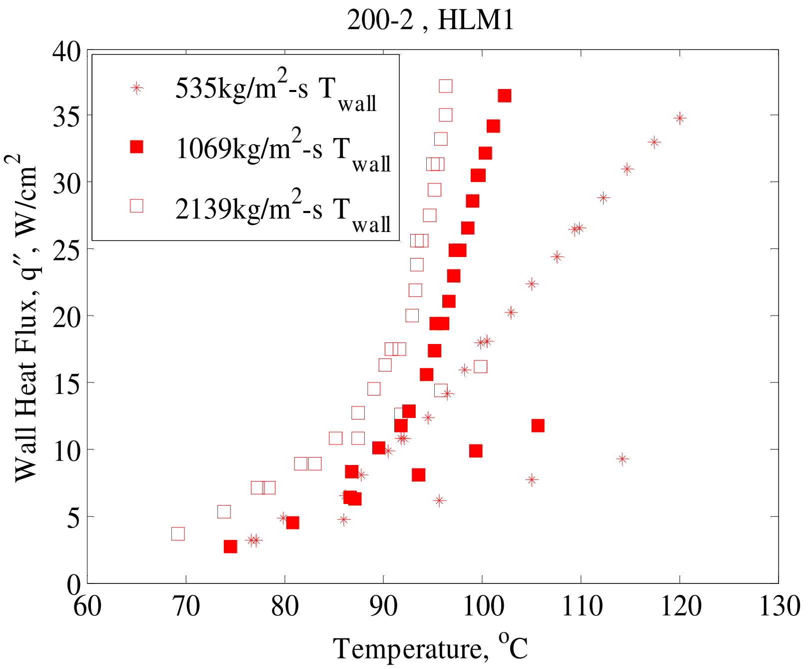

Figure 43: Flow boiling curves for specimen 200-2 at three values of mass flux and using HLM1.

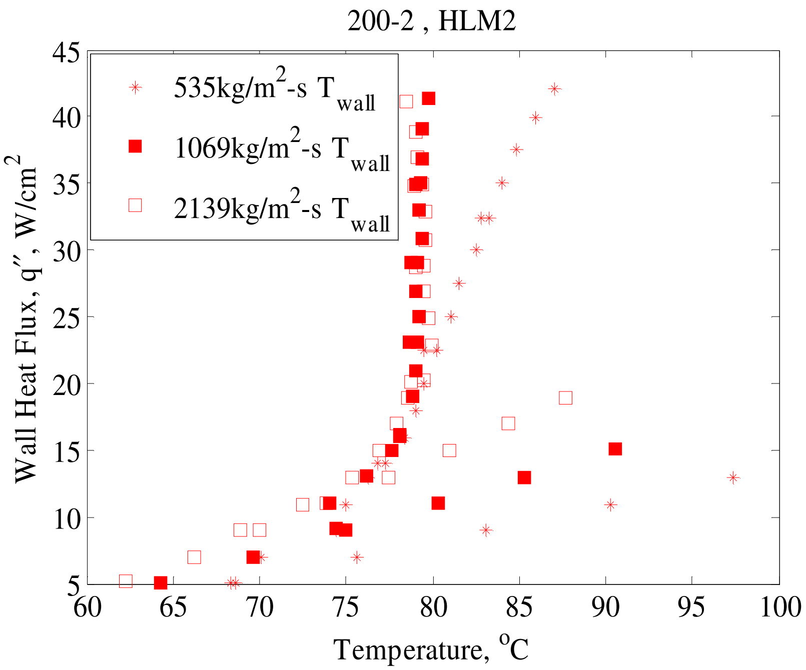

Figure 44: Flow boiling curves for specimen 200-2 at three values of mass flux and using HLM2.

4.2.2 Effect of channel size on boiling curves

In this section of the results, the effects of channel size will be displayed for two different mass fluxes. There are two distinct characteristics that stand out when looking at Figures 45 and 46. The first is that the curve for the 400-6 test section goes to higher heat fluxes than that of the 200-2 test section. The test sections heater pads were designed to accommodate approximately 85W before significant damage to the heater pad ensued. However, during the fabrication process, the deposition of the aluminum on the 200 series test section was inadvertently fabricated to half the thickness required to achieve this value. This resulted in higher current densities in the heaters at lower heat fluxes. To ensure that the heaters did not fail, they were only used up to half their originally intended heat flux values.

The other noticeable difference in the two curves is the much higher surface temperature for the 400-6 test section through out the heat flux range imposed. This is attributed to the reduction of the Nusselt number (Nu) due to an aspect ratio change which if all else where held equal, would lower the heat transfer coefficient, an effect that is compounded by the increase in hydraulic diameter (D_h). Recall that the heat transfer coefficient scales inversely on the hydraulic diameter. With these two factors in effect, the heat transfer coefficient is reduced enough to display a sizable difference in the two curves.

The scenario for a mass flux of 2139 kg/m^2-s for the 400-6 test section was conducted but will not be displayed in this portion do to a discrepancy in the heater resistance values during the test. Data displayed a difference between ascending and descending heat flux that implied the effects of electron migration had occurred.

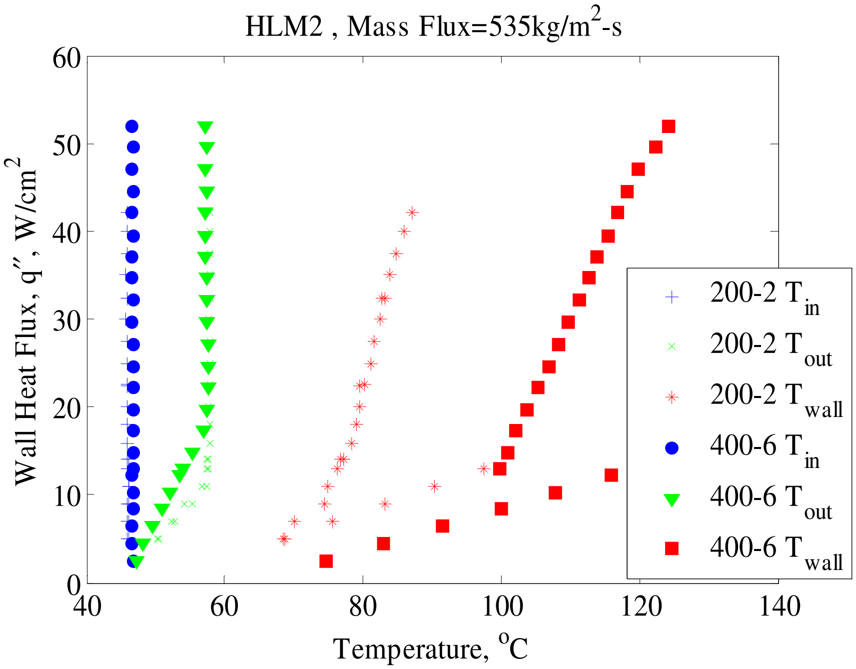

Figure 45: Comparison of channel size at a mass flux of 535 kg/m^2-s using HLM2.

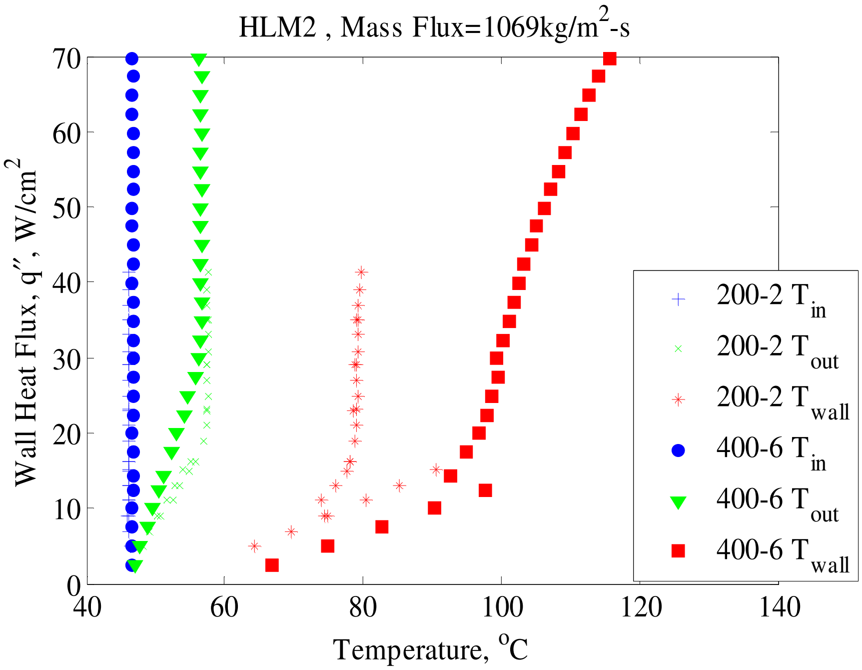

Figure 46: Comparison of channel size at a mass flux of 1069 kg/m^2-s using HLM2.

4.3 ONB and temperature overshoot

An interesting feature of Figures 40-45 is the pronounced appearance of temperature overshoot in the (T_{wall}) curve. This characteristic is introduced in section 1.2 by Figure 2 and its description. A maximum value of 21°C of temperature overshoot was recorded for the case of G = 535 kg /(m^2-s) on the 200-2 test section. As the experiment traverses down in heat flux, the path follows the traditional profile yielding a significant hysteresis in the boiling curves. These results are similar to reports previously described by Bowers and Mudawar [1994] and Lazarek and Black [1981] that were both using a dielectric refrigerant, R-113. Lazarek and Black [1981] reported overshoot values of 35°C in some cases.

Geometrically consistent cavities in the base of the channel (point of highest direct heat application) have the potential to not only produce a repeatable bubbly flow and eliminate potentially unstable slug formation but also positively affect the onset of nucleate boiling (ONB) by lowering the ONB flux and moving the ONB point further upstream. However the data in Figures 40-45 indicate (confirmed with high-speed imaging) that all these vapor generating sites are flooded with the highly-wetting dielectric liquid, inhibiting the early onset of boiling. This characteristic of a highly-wetting fluid causing a delay in ONB, as in this study, are similar to that reported by Bergles and Kandlikar [2005]

As previously mentioned, the data followed a more traditional path while heat flux was decreased. This is defined by a smooth transition back to single phase heat transfer. During what is generally defined as the partial boiling regime, the re-entrant cavities become the dominant vapor generating sites, as seen in Figure 47. This behavior occurred for all three flow rates tested.

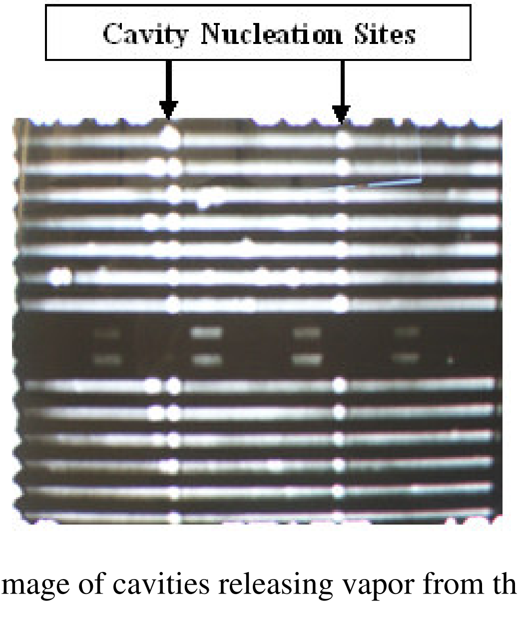

Figure 47: High speed image of cavities releasing vapor from the 200-2 test section.

4.3.1 Effect of flow rate on ONB

Generally speaking, the trend in Figures 43 and 44 is a decreasing value of temperature overshoot with increasing mass flux. This is displayed numerically in Table 7 for the 200-2 test section. A trend of increasing ONB heat flux is also observed with increasing mass flux. Figure 48 illustrates the heat flux at which ONB occurred for four different values of mass flux. This plot shows the expected increase in ONB value as a function of mass flux. These values deviate from those in Figures 43 and 44 due to the manner in which the data were collected. The values in the previous Figures were recorded for purposes of producing general heat transfer characteristics such as the boiling curves shown earlier, and heat transfer coefficients by recording data in increments of 2.5-4W depending on conditions. The data displayed in Figure 44 were collected with a much smaller increment between points to collect more refined information on data such as ONB and transition between flow regimes (which will be discussed later in section 4.6).

Mass Flux (kg/m2-s)	Temperature Overshoot, (°C)
535	21.0
1069	12.9
2138	9.1

Table 7: Tabulated experimental values of temperature overshoot for 200-2 test section.

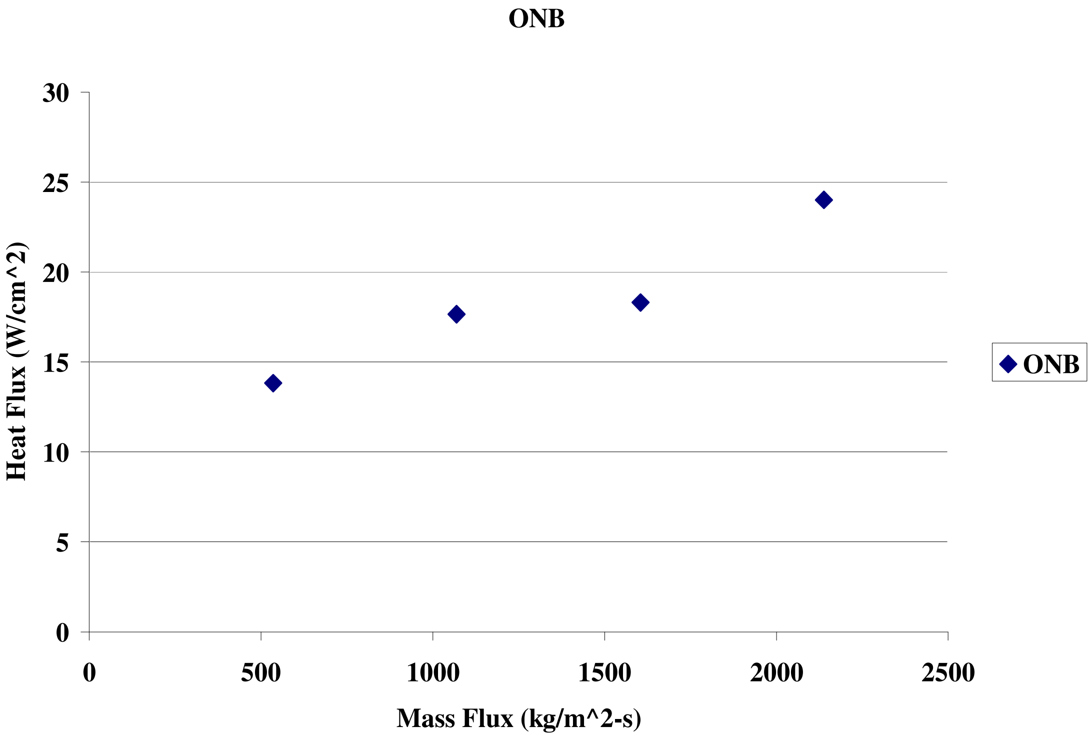

Figure 48: Experimental values of Onset of Nucleate Boiling (ONB) as a function of mass flux for the 200-2 test section.

4.3.2 Effect of gas content on ONB

As previously mentioned in Chapter 1, the dissolved gas content of the working fluid can have a profound effect on the heat transfer capabilities of the fluid. This topic is of particular interest to researchers using dielectrics and refrigerants due to their enormous affinity for dissolved gasses. FC72 at atmospheric conditions can contain as much as 49% dissolved gas by volume.

The effects of dissolved gas in the working fluid typically are an early transition to two-phase flow triggered by the dissolved gas, rather than fluid vapor released from random or purposely placed cavities. This has the desired effect of early ONB and the drastic reduction of temperature overshoot experienced with highly wetting fluids but is believed to decrease the two phase heat transfer coefficient (Steinke and Kandlikar [2003]). It is also extremely detrimental to condenser performance in a self contained two-phase heat sink system and is therefore to be avoided.

As an illustration, Figure 49 illustrates a set of data taken for a mass flux of 2139 kg/m^2-s on the 400-2 test section that was not properly degassed before starting the experiment. It can be seen that the curve lacks the dramatic overshoot seen in previous figures.

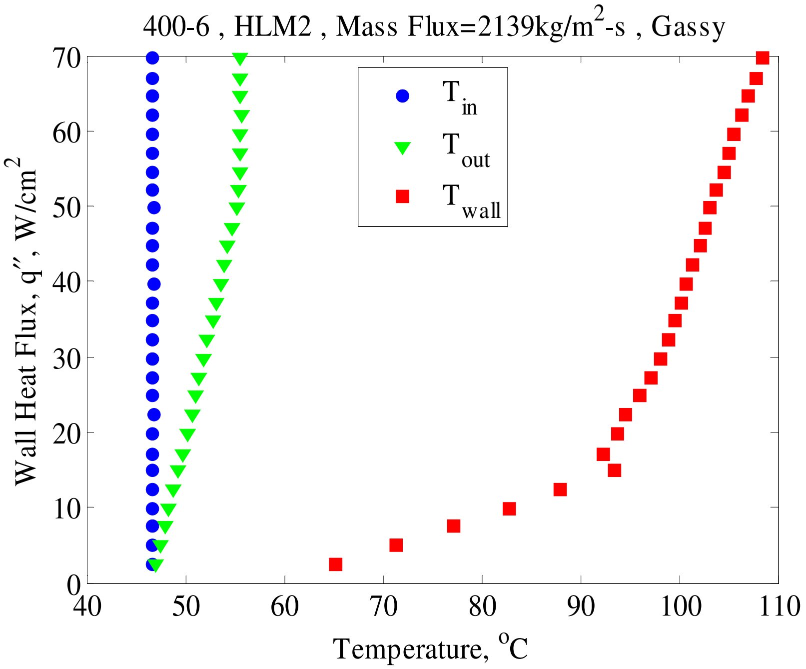

Figure 49: Boiling curve with gassy FC72.

4.4 Heat transfer coefficient

In this section, the quantitative effects of flow rate, heat flux, heat loss method and channel size on the heat transfer coefficient will be depicted. The validity of reported heat transfer coefficients is very important for microchannel work. Accurate measurements of flow rate, pressure, as well as surface and fluid temperatures are crucial to the development of proper predictive correlations and the comparison against existing ones.

4.4.1 Introduction to calculations

Before displaying any results, the means by which the data is reduced will be presented. The basic dimensions of the microchannel array are presented in Figure 50. These notations will be used in the explanation of the heat transfer coefficient calculations.

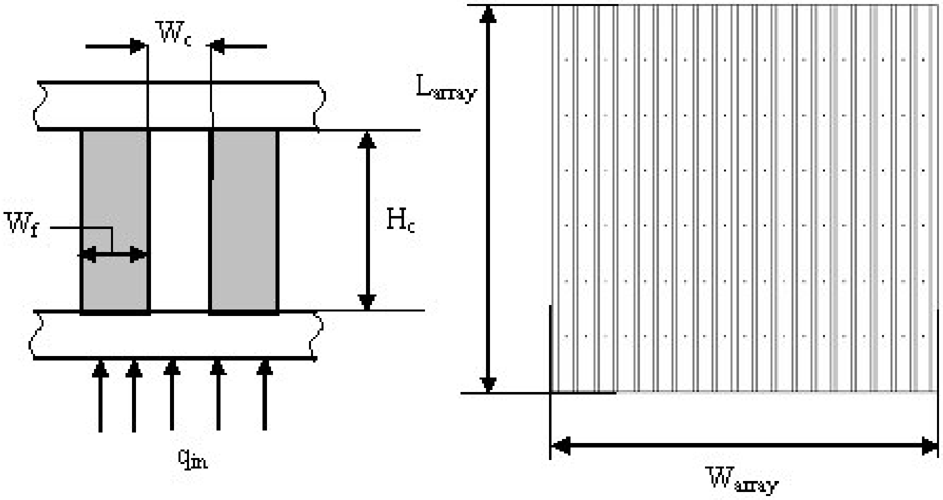

Figure 50: Basic dimensions of microchannel array.

The heat transfer coefficient for every scenario will be plotted against the coinciding exit quality which is calculated as follows.

$$x_e = \frac{q_{wall} - \dot{m}C_p\left(T_{sat} - T_{in}\right)}{\dot{m}h_{fg}} \tag{31}$$

Most applications of flow boiling wherein fluid enters the heated area with a mean fluid temperature below saturation (or some significant amount of sub-cooling) experience some heated length that is exposed purely to single phase convection or sub-cooled nucleate boiling. To quantify differences between this region and the saturated portion of the channel along the axial length of the test section, a single phase or sub-cooled length is calculated as follows.

$$L_{sb} = \frac{\dot{m}C_p\left(T_{sat} - T_{in}\right)}{\left(\frac{q_{wall}}{A_{array}}\right)W_{array}} \tag{32}$$

The heat transferred to the fluid over this sub-cooled portion of the test section is calculated by Equation 33.

$$q_{in} = \frac{q_{wall}}{A_{array}} \cdot N(W_f + W_c) \cdot L_{sb} \tag{33}$$

Using these two values, an iterative bisection method is used coupled with the adiabatic tip fin equation to solve for the average heat transfer coefficient (h_{sb}) for the length of (L_{sb}) as follows.

$$P_{sb} = 2 \cdot L_{sb} \tag{34}$$

$$A_{fb-sb} = W_f \cdot L_{sb} \tag{35}$$

$$A_{cb-sb} = W_c \cdot L_{sb} \tag{36}$$

$$m^2 = \frac{h_{sb}P_{sb}}{k_{si}A_{fb-sb}} \tag{37}$$

$$\Theta_{b-sb} = (T_{wall} - T_{mf}) \tag{38}$$

$$M = \sqrt{h_{sb} P_{sb} k_{si} A_{fb-sb}} \cdot \Theta_{b-sb} \tag{39}$$

$$q_{out} = N(M \tanh(mH_c) + h_{sb} A_{cb-sb} \Theta_{b-sb}) \tag{40}$$

This iterative scheme is continued until the experimentally gathered value of heat input expressed in Equation 33 equals the heat output of the fin array displayed in Equation 40 or ($q_{in} = q_{out}$) based on a tolerance of +/- 1E-5.

The saturated portion of the channel is treated in similar fashion. After the heat transfer coefficient (h_{sb}) for the sub-cooled portion of the channels is calculated, a saturated length is calculated as follows.

$$L_{tp} = L_{array} - L_{sb} \tag{41}$$

$$\Theta_{b-tp} = (T_{wall} - T_{sat}) \tag{42}$$

The temperature difference used for the saturated case is the difference between T_{wall} and T_{sat} as opposed to the sub-cooled case which uses the T_{mf} or the average of the inlet and outlet thermocouples. With these two values tabulated, the exact procedure carried out to calculate the heat transfer coefficient (h_{sb}) for the sub-cooled region is repeated for the saturated length (L_{tp}) to calculate (h_{tp}). A weighted averaging method based on the lengths (L_{sb} and L_{tp}) are used to quantify the average heat transfer coefficient for the entire channel array as seen in Equation 43.

$$h_{avg} = \frac{L_{sb} h_{sb} + L_{tp} h_{tp}}{L_{array}} \tag{43}$$

4.4.2 Effect of flow rate on heat transfer coefficient

Figures 51-55 present the effect of flow rate on the average heat transfer coefficient or the value of (h_{avg}) plotted against exit quality (x_e) for three different values of mass flux. Figures 51-53 also individually present the difference between HLM1 and HLM2 for those flow rates. These data are the ones used to develop the boiling curves presented in section 4.2. Seen in Figures 51-53, the HLM has a tremendous effect on the heat transfer coefficient as it more than doubles it under some conditions. The heat transfer coefficients re-plotted in Figures 54 and 55 show the values of (h_{avg}) for all three flow rates for HLM1 and HLM2. Both of these plots show the effect of an increase in flow rate by the leftward shifting of the curves.

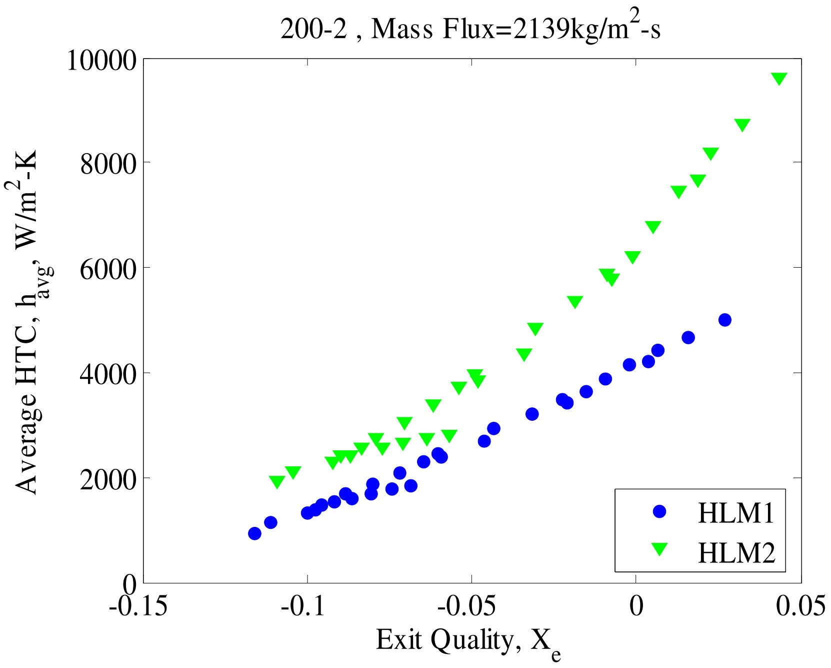

Figure 51: Average heat transfer coefficient for specimen 200-2 at a mass flux of 2139 kg/m^2-s displaying the difference between HLM 1 and 2.

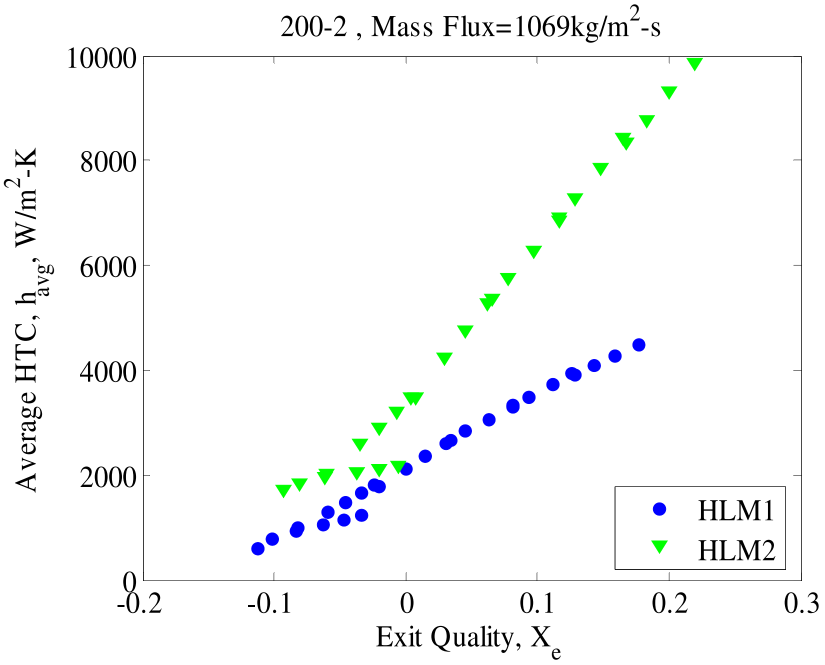

Figure 52: Average heat transfer coefficient for specimen 200-2 at a mass flux of 1069 kg/m^2-s displaying the difference between HLM 1 and 2.

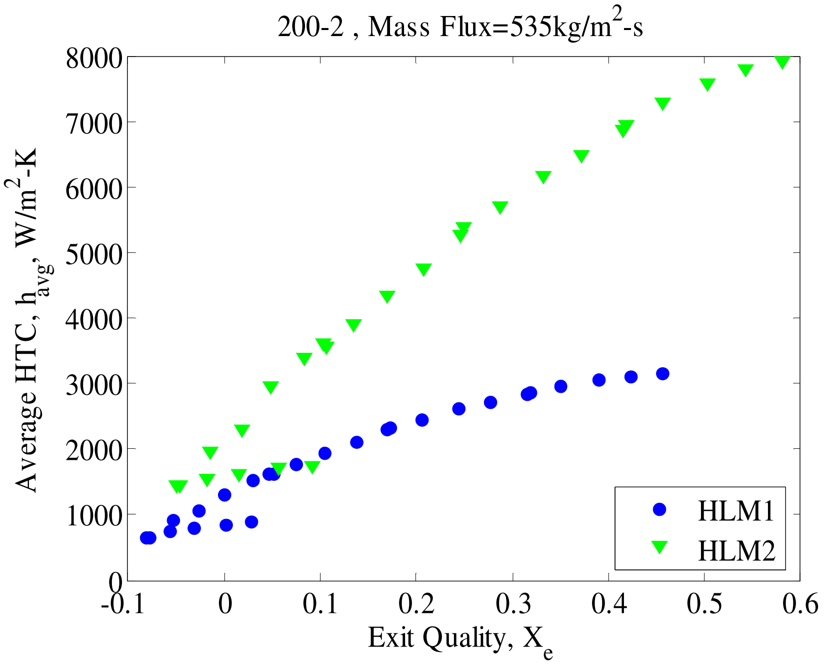

Figure 53: Average heat transfer coefficient for specimen 200-2 at a mass flux of 535 kg/m^2-s displaying the difference between HLM 1 and 2

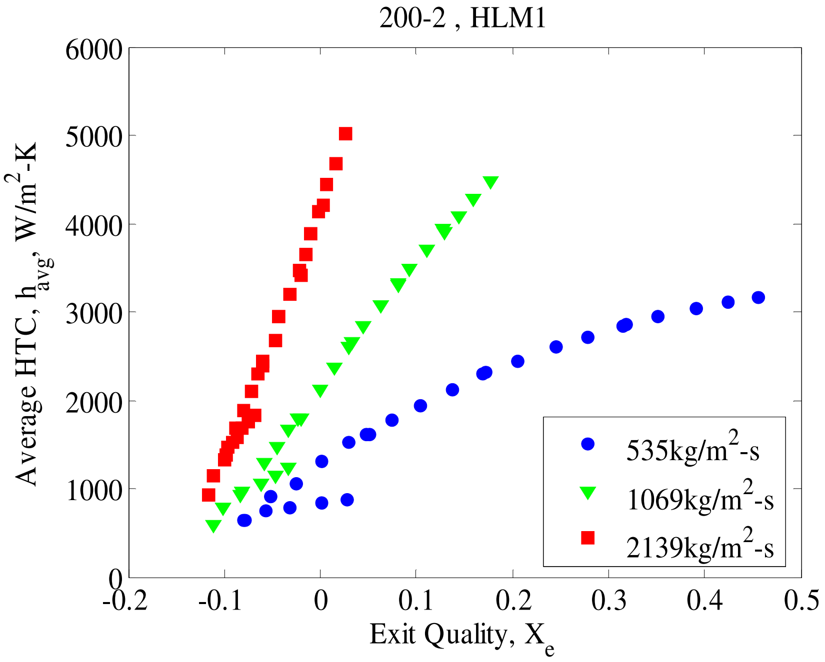

Figure 54: Average heat transfer coefficients for specimen 200-2 at three values of mass flux and using HLM1.

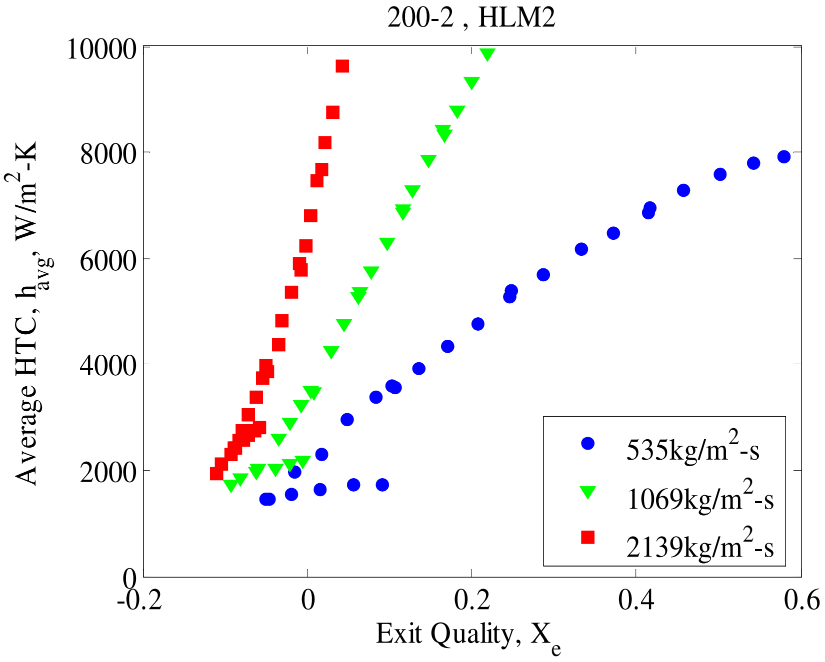

Figure 55: Average heat transfer coefficients for specimen 200-2 at three values of mass flux and using HLM2.

The heat transfer coefficients attainable with dielectrics such as FC72 are much lower than that of water due to the differences of thermal properties. Tran, et al. [1995] reported in a minichannel study, heat transfer coefficients of 11,000W/m^2-K using R-12 and R-113. Hetsroni, et al. [2002] reported in a resent microchannel study, heat transfer coefficients in the range of 6000-10,000 W/m^2-K using a fluid by the name of Vertrel XF that has similar properties to FC72. These properties along with those of water are displayed in Appendix A for comparison. It should be noted that heat transfer coefficients for water under similar conditions are in the range of 40,000W/m^2-K such as those reported by Kosar, et al. [2005].

4.4.3 Effect of channel size on heat transfer coefficient

As previously mentioned in section 4.2, the main difference in thermal performance in test section 400-6 and 200-2 is attributed to the reduction of the Nusselt number (Nu) due to an aspect ratio change which if all else were held equal, would lower the heat transfer coefficient and this effect is compounded by the increase in hydraulic diameter (D_h). With these two factors in effect, the heat transfer coefficient is reduced enough to display a sizable difference in the two curves.

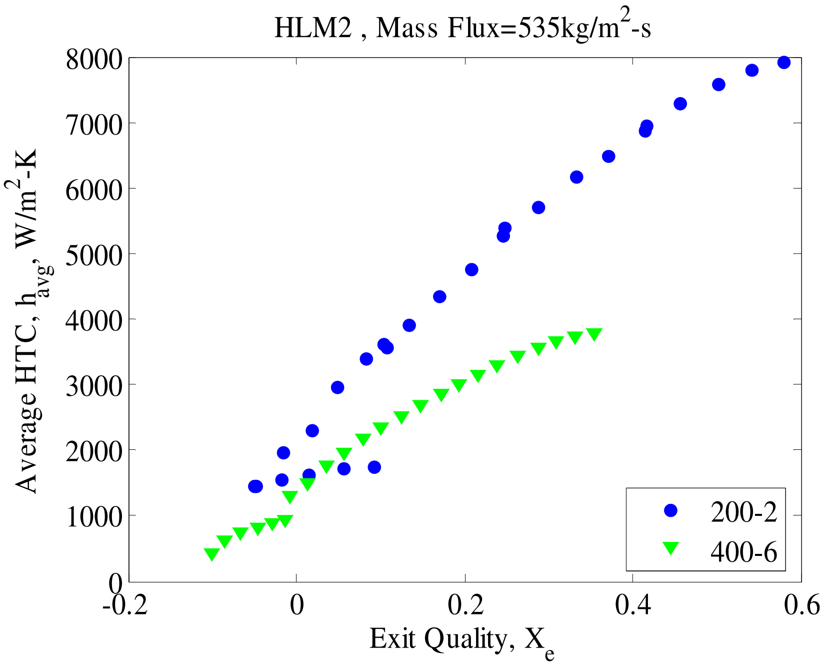

Figure 56: Average heat transfer coefficients for specimens 200-2 and 400-6 at a mass flux of G=535 kg/m^2-s and using HLM2.

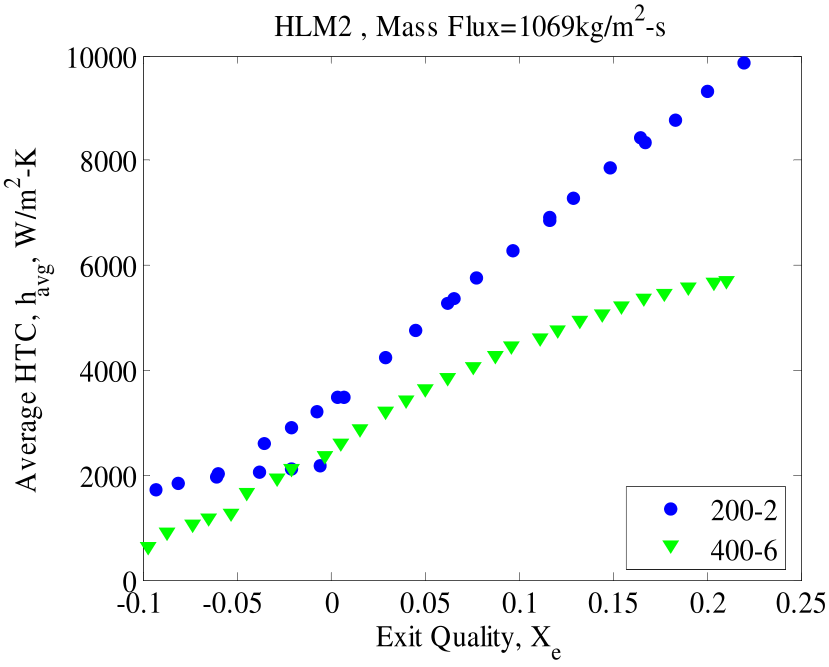

Figure 57: Average heat transfer coefficients for specimens 200-2 and 400-6 at a mass flux of G=1069 kg/m^2-s and using HLM2.

4.4.4 Comparison of data with analytical models

For industry to implement microchannels as a reliable cooling solution to high heat flux applications, reliable two-phase heat transfer correlations have to be developed and evaluated rigorously. As previously mentioned the ability to measure and validate heat transfer data on small scales such as microchannels are difficult by nature. The validity of macrochannel-scale correlations have been tossed back and forth on grounds that many claim that macro-scopic fluid and heat transfer mechanisms are different for micro-scale channels. This portion of the current study will compare the data collected against a few existing correlations both micro- and macro-scale. Most of the correlations chosen and displayed in this section were done on the basis of comparable channel sizes or fluid type. Also all comparisons will be made against experimental data using HLM2.

The definitions of a few dimensionless numbers such as the Reynolds, Weber, Convection and Boiling numbers are shown in Equations 44-47 since they will be used in the description of several correlations.

$$\mathrm{Re} = \frac{GD_h}{\mu_l} \text{ (Ratio of inertial to viscous forces)} \tag{44}$$

$$We_l = \frac{G^2 D_h}{\rho_l \sigma} \text{(Ratio of inertial to surface tension forces)} \tag{45}$$

$$Co = \left(\frac{1-x}{x}\right)^{0.8} \left(\frac{\rho_v}{\rho_l}\right)^{0.5} \text{ (Modified Martinelli parameter)} \tag{46}$$

$$Bo = \frac{q''}{G \cdot h_{fg}} \text{ (A measure of the strength of nucleate boiling)} \tag{47}$$

For conditions of nucleate saturated flow boiling, Warrier, et al. [2002] developed this correlation that is dependent on quality (x) and the boiling number (Bo). This correlation was developed using a test section made of aluminum with five channels with a hydraulic diameter of D_h= 0.75mm. This is somewhat larger in diameter than the current study but the test fluid used was FC84 which is very close to FC72 in heat transfer properties. The mass flux range of G=557-1600 kg/m^2-s tested in that study is also similar to that used in the present study. Warrier, et al [2002] proposed the following:

$$h_{tp} = h_{sp-FD}(1 + 6Bo^{1/16} + f_1(Bo)x_e^{0.65}) \tag{48}$$

$$f_1(Bo) = -5.3[1 - 855Bo] \tag{49}$$

As previously mentioned the correlation by Warrier, et al. [2002] is for conditions of nucleate saturated boiling. As explained in Chapter 1, there are two major mechanisms of flow boiling, ie nucleation or convective dominant heat transfer. This is one of the major ongoing debates in the microchannel field of research. Researchers such as Qu and Mudawar [2003] claim that convective boiling is the dominant mechanism due to any evaporation consuming the volume of the channels and forcing the flow into an annular convective regime. On the other hand researchers such as Kandlikar [2004], state that nucleation is the dominant mechanism of two phase heat transfer in microchannels. Ultimately the mechanism is more likely a strong function of the fluid used and the size of the channels studied.

With this in mind the following two correlations were developed by Balasubramanian and Kandlikar [2004] for conditions of both Nucleate Dominated Boiling (nbd), and Convective Dominated Boiling (cbd). These correlations are an extension to low Reynolds number applications of an existing correlation developed by those researchers for macrochannels. These correlations are functions of the Convection number, Boiling number, quality, and a fluid dependent constant (F_{fl}). The researchers provide a table with values of (F_{fl}) for a variety of fluids but FC72 was not one listed. The researcher suggest the use of the value for water which is $F_{fl}=1$, for fluids that are not listed.

$$h_{tp-nbd} = h_{sp-FD}(0.6683Co^{-0.2}(1-x)^{0.8} + 1058Bo^{0.7}(1-x)^{0.8}F_{fl}) \tag{50}$$

$$h_{tp-cbd} = h_{sp-FD}(1.136Co^{-0.9}(1-x)^{0.8} + 667.2Bo^{0.7}(1-x)^{0.8}F_{fl}) \tag{51}$$

For conditions of nucleate saturated flow boiling, Lazarek and Black [1981] developed a correlation that is dependent on Reynolds (Re) and the boiling number (Bo). This correlation was developed using a test section made of a single stainless steel tube with a hydraulic diameter of D_h= 3.15mm. This is a lot larger in diameter than the current study but the test fluid used was R-113 which is very close to FC72 in heat transfer properties. The mass flux range of G=125-750 kg/m^2-s conducted in that study is also in the test range of the values tested in the current study.

$$h_{tp} = 30\,\mathrm{Re}^{0.857}\,Bo^{0.714}\left(\frac{k_f}{D_h}\right) \tag{52}$$

For conditions of nucleate saturated flow boiling, Tran, et al. [1995] developed a correlation that is dependent on Weber number (We_l) and the boiling number (Bo). This correlation was developed using a test section made of a single tube arrangement with a hydraulic diameter of D_h= 2.4mm for both circular and square channels. The test fluids used were R-12 and R-113 and were delivered over a mass flux range of G=44-832 kg/m^2-s. This correlation showed very good agreement with the current studies data as will be shown in the following section.

$$h_{tp} = (8.4*10^{-5})(Bo^2 We_l)^{0.3}\left(\frac{\rho_l}{\rho_v}\right)^{-0.4} \tag{53}$$

Kosar, et al. [2005] developed a fully empirical correlation that is dependent on heat flux only. This correlation was developed using a test section made of an array of 5 silicon microchannels with a hydraulic diameter of D_h= 227µm. The test fluid used was water and was delivered over a mass flux range of G=28-445 kg/m2-s.

$$h_{tp-nbd} = 1.068(q'')^{0.64} \tag{54}$$

A correlation for conditions of nucleate sub-cooled flow boiling is presented by Shah [1997] that is dependent on the amount of sub-cooling and the boiling number (Bo). This correlation was developed over a wide range of sub-cooling 0-153^{o}C, mass flux of G=55-24166 kg/m^2-s, and fluids such as water, R-11, R-12, R-113, ammonia, and methanol to name a few. This researcher also varied hydraulic diameter of D_h= 2.4-27.1mm for circular stainless steel channels. This correlation showed very good agreement with the data from the current study, as will be shown in the following section.

$$h_{tp} = h_{sp-FD}\left[1+(\psi_o - 1)\frac{T_{wall}-T_{sat}}{T_{wall}-T_{mf}}\right] \tag{55}$$

$$\psi_o = \begin{bmatrix} 230Bo^{0.5} -----Bo > 3\times10^{-5} \\ 1+46Bo^{0.5} ----Bo < 3\times10^{-5} \end{bmatrix} \tag{56}$$

All the previous correlations mentioned feature uniform heating from the entire periphery of the channel except for Kosar, et al. [2005]. The current study has a three-heated-side configuration due to the low thermal conductivity of the top Pyrex glass used to cap the channels and allow for visualization. Due to this effect a correction factor is implemented as described by Shah and London [1978]. This correction factor takes Equations 57 and 58 to calculate the three and four side heated fully developed Nusselt number (Nu_3 and Nu_4) to produce the Nusselt Correction Factor (NCF) seen in Equation 59. Each of the previous correlations are corrected by this factor before comparison with data.

$$Nu_3 = 8.235(1 - 1.883\beta + 3.767\beta^2 - 5.814\beta^3 + 5.361\beta^4 - 2\beta^5) \tag{57}$$

$$Nu_4 = 8.235(1 - 2.042\beta + 3.085\beta^2 - 2.477\beta^3 + 1.058\beta^4 - 0.186\beta^5) \tag{58}$$

$$NCF = \left[\frac{Nu_3}{Nu_4}\right] \tag{59}$$

A graphical correlation comparison has been constructed in Figures 58-69. Figures 58, 61, and 65 are all of the previous saturated correlations compared against the experimental data (h_{tp}) for three different mass fluxes. Following each of the bulk comparisons are a few of the correlations that fit closest to the present data, plotted as the % difference. This is calculated by Equation 60 as follows.

$$\%Difference = \left(\frac{Experimental - Correlation}{Experimental}\right) \times 100 \tag{60}$$

For the case of G=535 kg/m^2-s, the Warrier and Tran correlations showed the best agreement plotted in Figures 59 and 60. For the case of G=1069 kg/m^2-s, the Warrier, Tran and Kandlikar-cbd correlations showed the best agreement plotted in Figures 62-64. For the case of G=2139 kg/m^2-s, the Tran and Kandlikar-nbd correlations showed the best agreement plotted in Figures 66 and 67.

The results of Kandlikar's correlations matching in the fashion of (cbd) for the lower flow rate and the (nbd) for the higher flow rate make qualitative sense. At the lower flow rates, the same heat flux results in a higher quality. This higher quality pushes the system toward an annular flow regime where convective boiling is understood to dominate. At the higher flow rate, lower qualities are achieved and bubble sizes from nucleation sites are smaller due to the inertial force of the higher flow rate promoting more conducive conditions for bubble nucleation dominated flow. Although the Tran correlation was developed for macro and mini channel applications, it matched within 18% for all saturated conditions. For two-phase heat transfer correlations this is well within the region of acceptability.

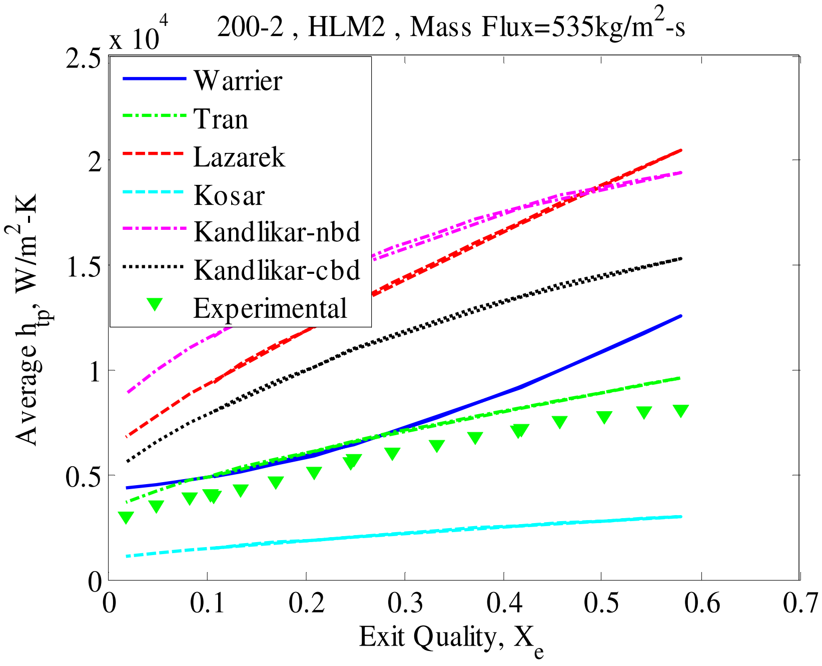

Figure 58: Saturated correlation comparison with experimental data at G=535 kg/m^2-s.

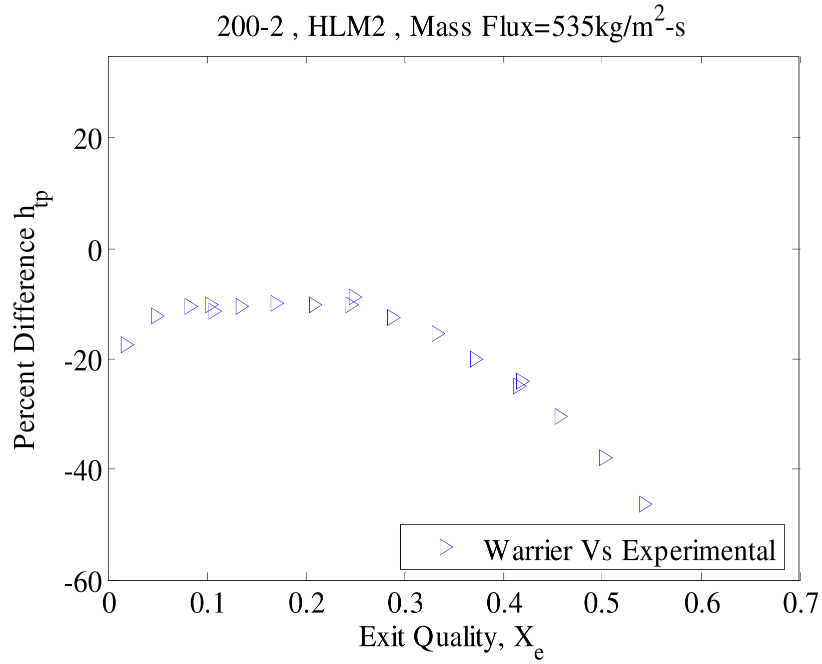

Figure 59: Percent Difference comparison of Warrier and experimental data at G=535 kg/m^2-s.

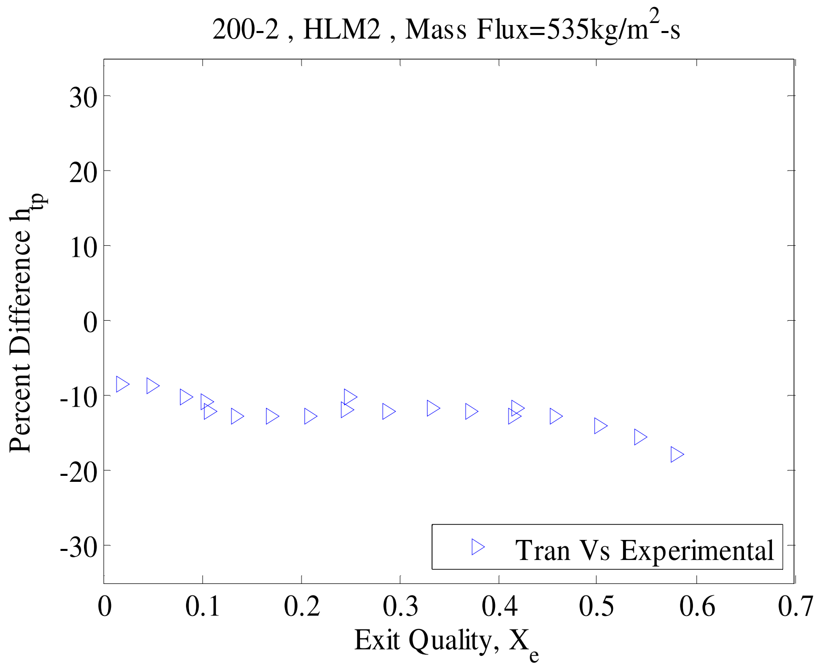

Figure 60: Percent Difference comparison of Tran and experimental at G=535 kg/m^2-s.

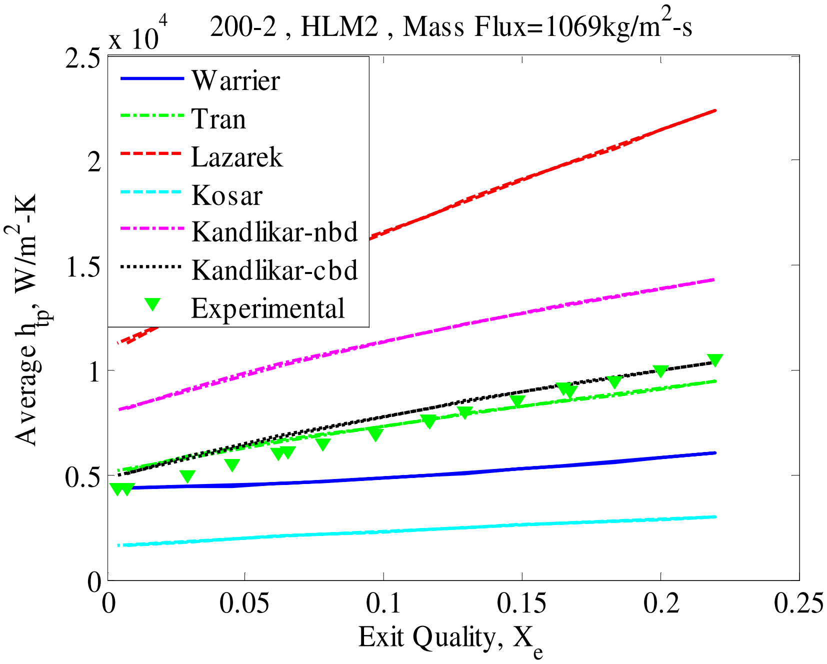

Figure 61: Saturated correlation comparison with experimental data at G=1069 kg/m^2-s.

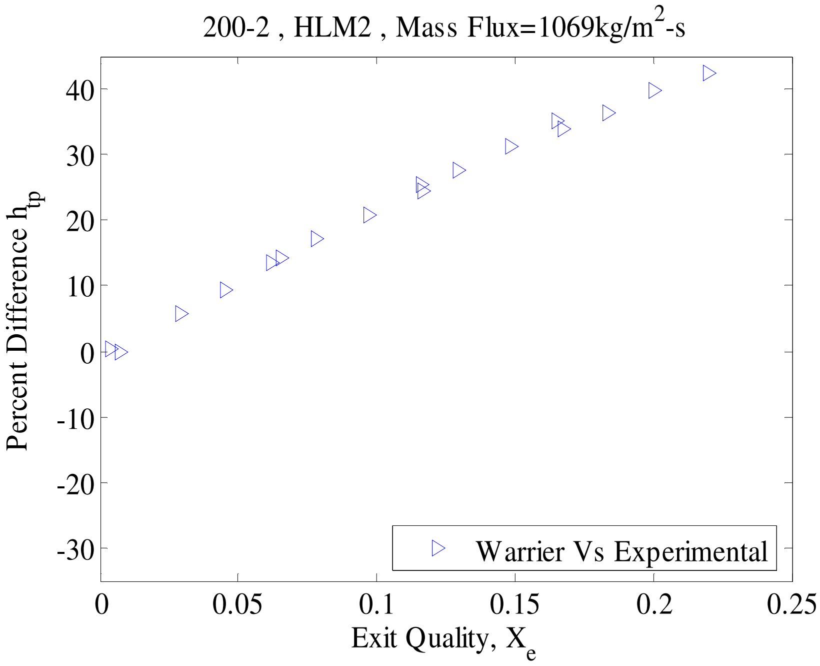

Figure 62: Percent Difference comparison of Warrier and experimental at G=1069 kg/m^2-s.

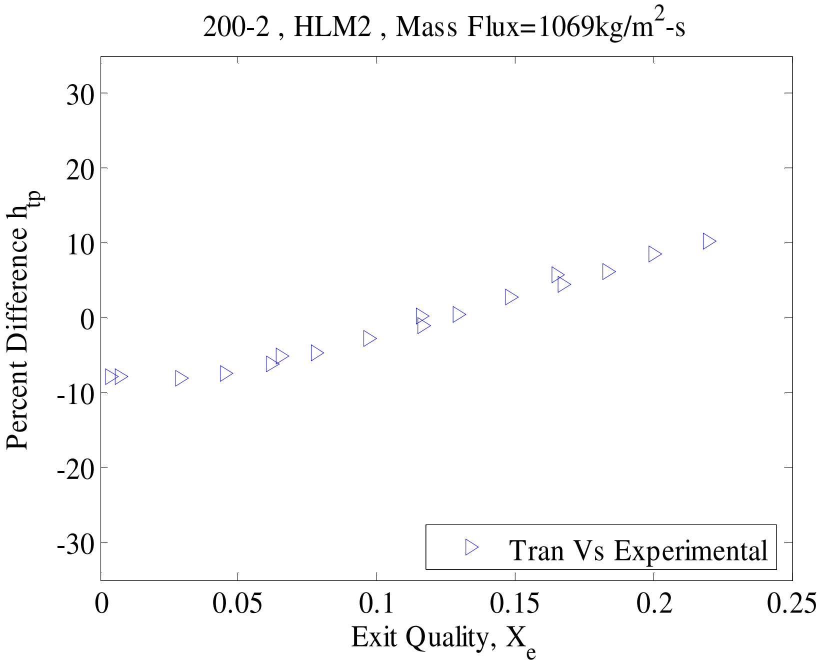

Figure 63: Percent Difference comparison of Tran and experimental at G=1069 kg/m^2-s.

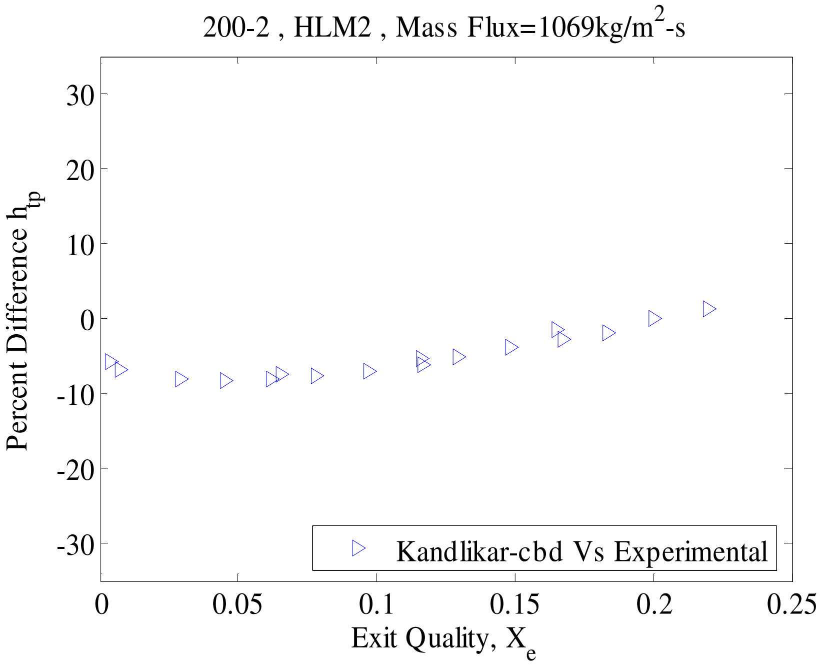

Figure 64: Percent Difference comparison of Kandlikar-cbd and experimental at G=1069 kg/m^2-s.

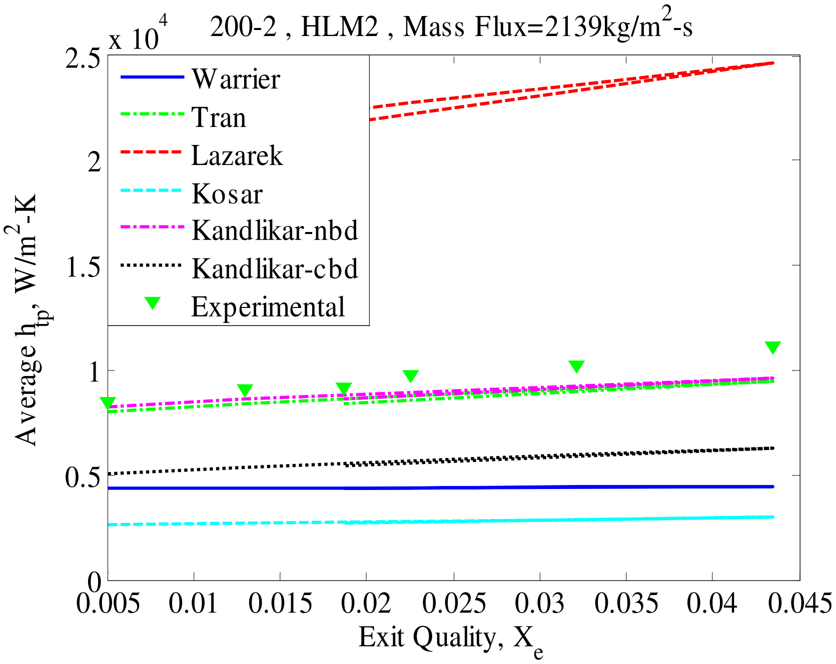

Figure 65: Saturated correlation comparison with experimental data at G=2139 kg/m^2-s.

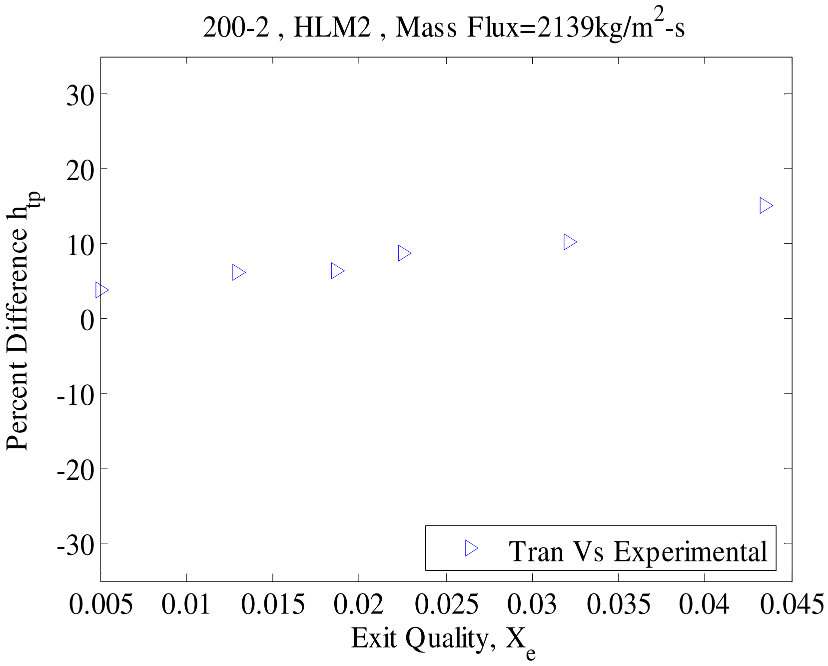

Figure 66: Percent Difference comparison of Tran and experimental at G=2139 kg/m^2-s.

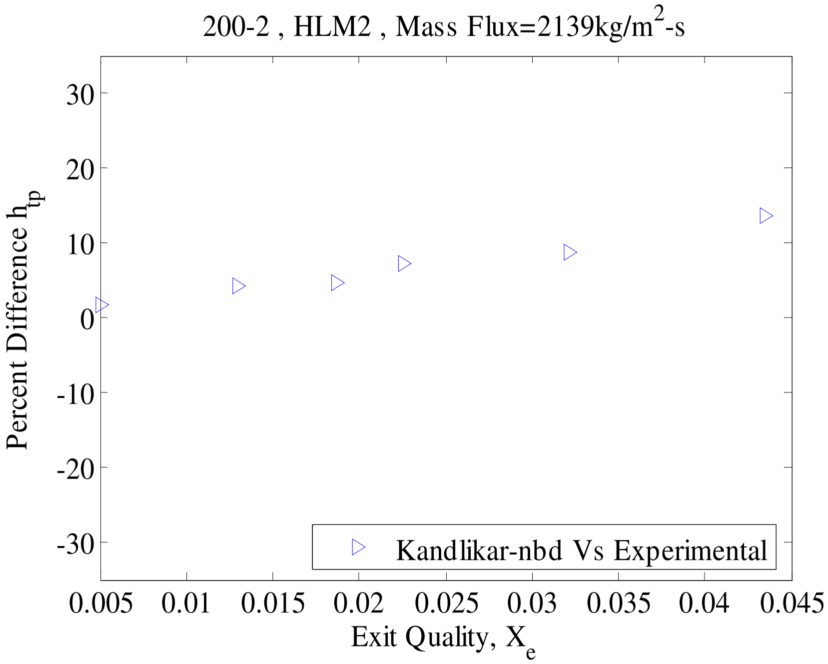

Figure 67: Percent Difference comparison of Kandlikar-nbd and experimental at G=2139 kg/m^2-s.

Unlike the rest of the correlations which dealt with the saturated portion of the channels, the Shah correlation is specifically for sub-cooled nucleation conditions. A graphical correlation comparison has been constructed in Figures 68. The current studies experimental data (h_{sb}) for the sub-cooled portion of the experiments are plotted against quality and show close comparison with that of the Shah correlation. Only the highest flow rate is compared for this due to the lack of sub-cooled data at the lower flow rates since saturated conditions develop very close to the inlet at lower flow rates. As seen in Figure 69 the Percent Difference never exceeds 15% which is very good. The Shah correlation was also developed for mini to macro scale channels as the Tran correlation but both showed good agreement for microchannel scale systems.

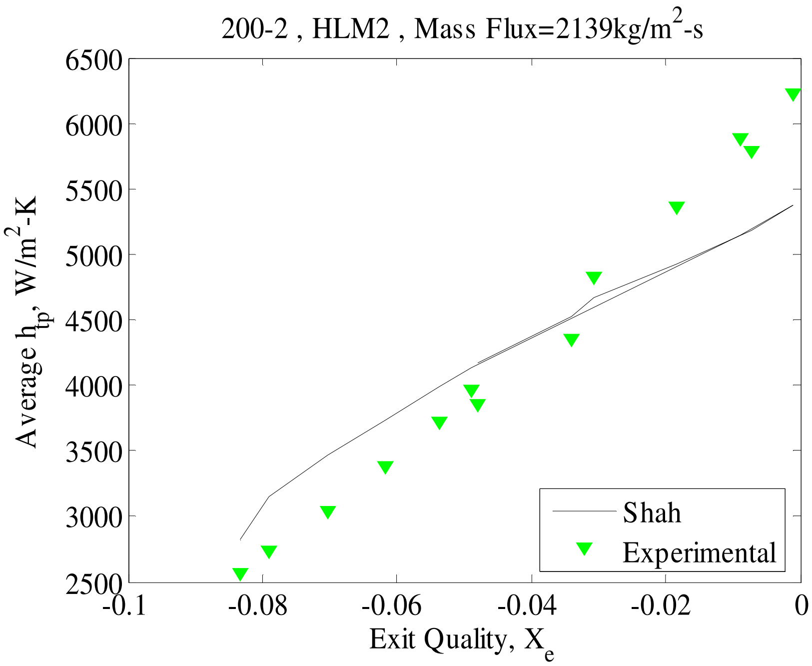

Figure 68: Sub-cooled correlation comparison with experimental data at G=2139 kg/m^2-s.

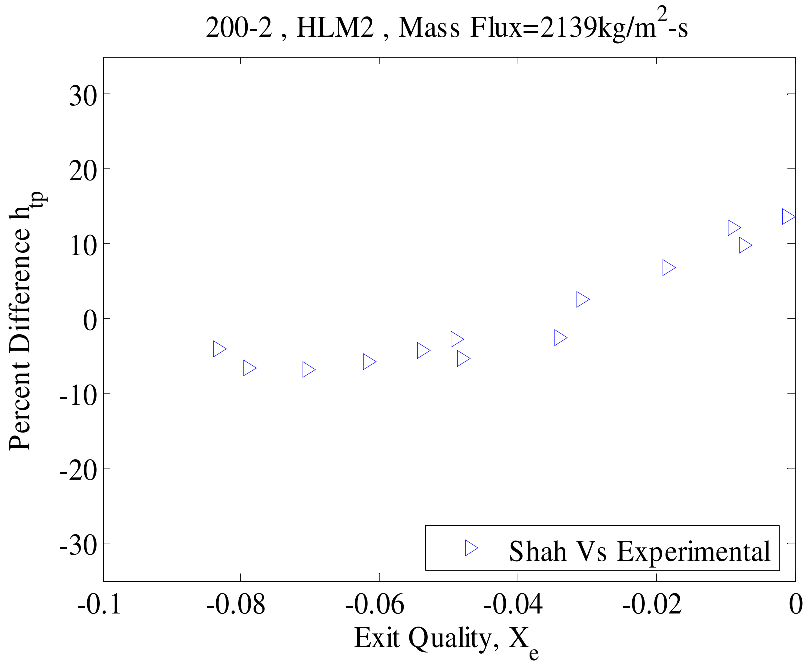

Figure 69: Percent Difference comparison of Shah and experimental at G=2139 kg/m^2-s.

4.5 Heat loss method justification and temperature sensor data

Quantifying heat losses are very important for a study such as this. As previously displayed in section 4.2 and 4.4, the heat loss quantification method can make a tremendous difference in the displayed output performance of the test section in question. Because the logic used to develop HLM2 over HLM1 does not necessarily make it correct, the current study has attempted to justify one or the other by additional means. By using the data collected from the test set up consisting of the temperature of the heater pad, the in-channel temperature sensors, heat input, and calculated heat transfer coefficient, an attempt has been made to validate one of the two heat loss methods.

4.5.1 In-Channel temperature sensors

As previously mentioned, the dielectric property of the fluid FC72, which is used in this study made sensor signal retrieval possible from the in-channel sensors. Figure 70 displays data of the inlet and outlet thermocouples, one of the in-flow temperature sensors, as well as the calculated surface temperature of the silicon, T_{wall}. All of these are plotted against the effective heat applied, q_{wall}.

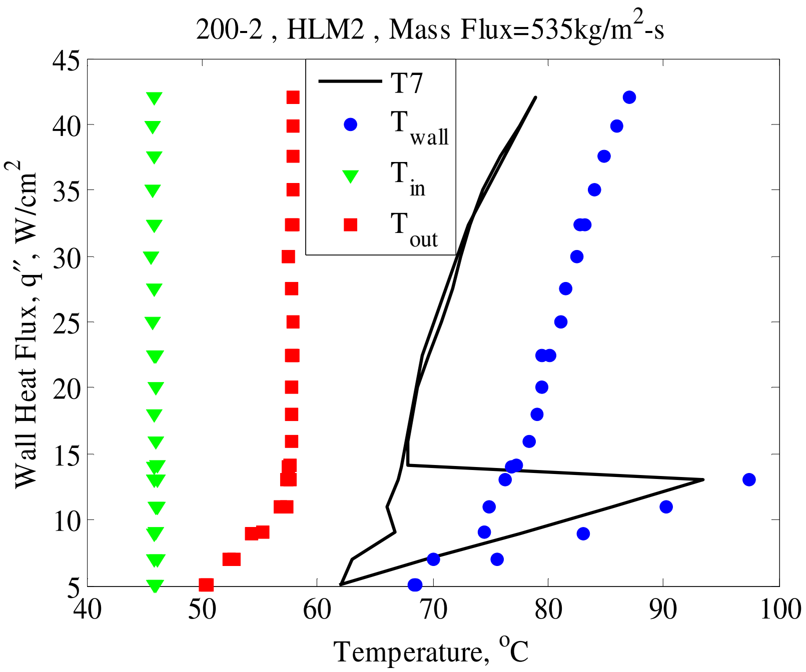

Figure 70: In-channel sensor curve for 200-2 test section and G=535 kg/m^2-s.

The in-channel sensor plotted here represents the third sensor in series along the axial length of column 2 depicted in Figure 71. As previously mentioned in the fabrication section of this thesis, the temperature sensors were an attempt to monitor the fluid temperature along the length of the channel. The sensors are located on a low thermal conductivity substrate (Pyrex) in order to minimize conduction effects through the silicon microchannel array. Testing quickly revealed that some conduction effects through the microchannel walls are present. The first and most obvious indication of this is that the sensor values do not fall between the inlet and outlet thermocouples curves, but rather between the outlet thermocouple and the extrapolated silicon surface temperature (T_{wall}). The second indication of this effect is that the sensor plotted show signs of temperature overshoot much like the (T_{wall}) curve.

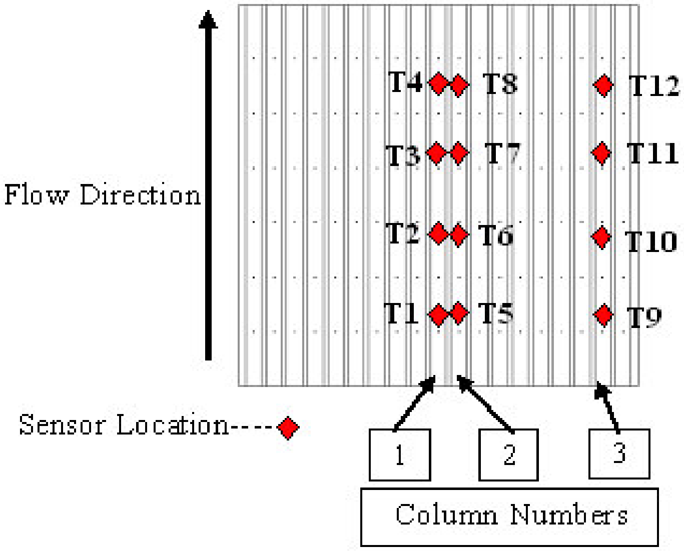

Figure 71: Temperature sensor notation and location for multi-channel test sections.

4.5.2 FEA confirmation of silicon and in-channel sensor temperatures

As previously mentioned, the current study has attempted to validate the choice of a HLM by additional efforts. This is performed by means of an FEA model constructed in ALGOR. First a dimensionally accurate model of the 200-2 test section is configured for a single channel. The value of q_{wall} is applied to the bottom boundary in heat flux form based on which HLM is being analyzed. The second input is the experimentally quantified average heat transfer coefficient h_{avg}, which is applied to the channel walls and is also HLM dependent. The code is run and the values of the channel wall temperature, T_{wall} and the temperature of Pyrex where the sensors are located, T_s are collected. The

FEA output is displayed in Figure 72 that show boundary conditions and locations of collected values of T_{wall} and T_s.

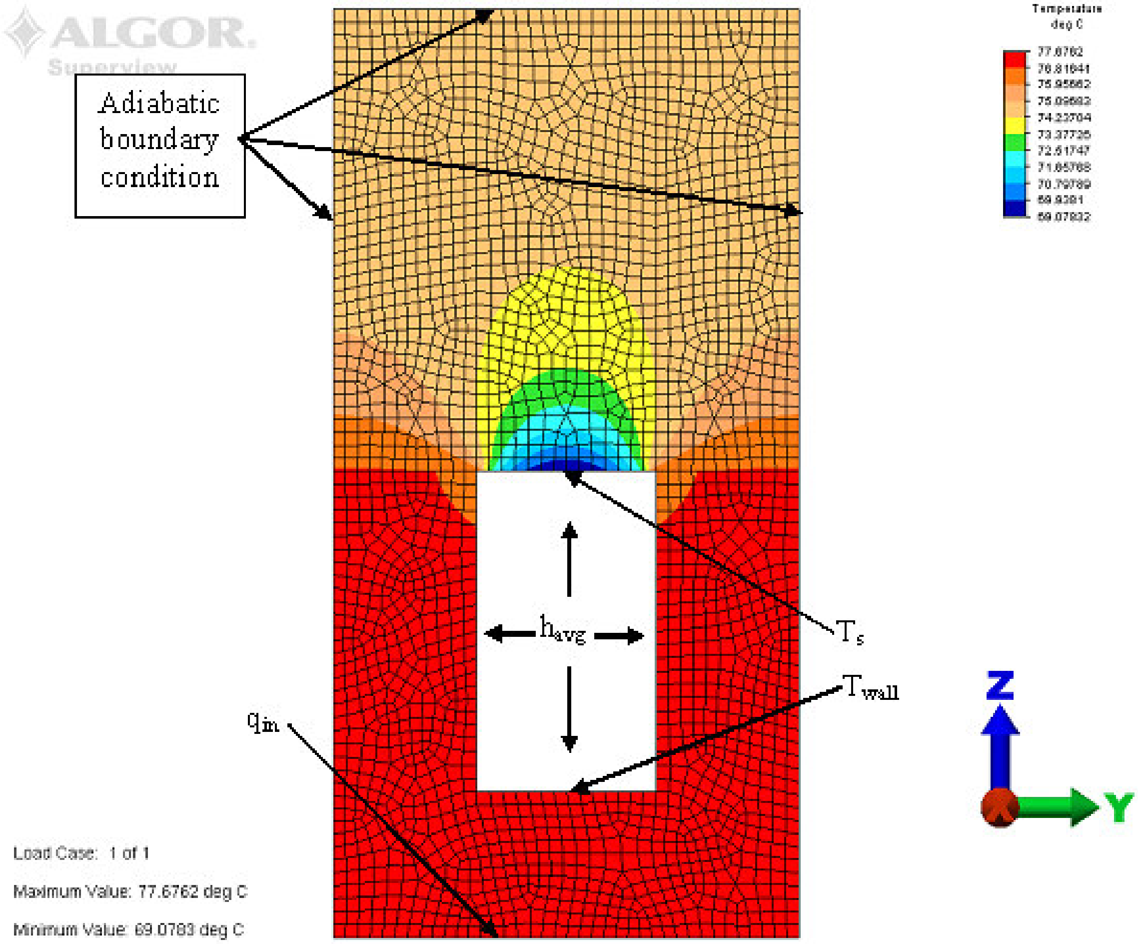

Figure 72: ALGOR FEA output for heat loss method confirmation.

In Tables 8 and 9 the results of this analysis are displayed for four data points. This analysis was conducted on the 200-2 test section at a mass flux of G=1069 kg/m^2-s. The four data points are the same for both HLM1 and HLM2 in terms of heat applied to the test section. The differences lie in how much heat is carried away by the fluid and where the losses occur. Also the four points were strategically picked to have one point of single phase heat transfer, two points of saturated flow boiling and one point of subcooled flow boiling.

The experimental values of T_s and T_{wall} are both average values due to the use of an average heat transfer coefficient. $\Delta T_s = T_s - T_{sat}$ and $\Delta T_{wall} = T_{wall} - T_{sat}$. As can be seen in Tables 8 and 9 the percent difference of the FEA output temperature and the experimental values are evaluated and the average percent difference is displayed at the bottom of the tables. The difference between HLM1 and HLM2 for the evaluation of ΔT_{wall} is not that drastic, showing a mean difference for HLM1 of 14.6% and 11.4% difference for HLM2. This was expected simply due to the fact that the experimental values of T_{wall} for both HLM1 and HLM2 are used in the calculation of the average heat transfer coefficient that is put into the FEA model, revealing similar results.

The key to this entire technique is the values of the in-channel temperature sensors. Having an independent variable to match up with the code provides a quantitative method to compare the two heat loss methods. As seen in Table 8 and 9 the difference between HLM1 and HLM2 for the evaluation of T_s is substantial, showing a mean difference for HLM1 of 101.9% and 11% difference for HLM2. This helps identify HLM2 as being more realistic.

Heat Loss Method 1			
Code Inputs			
q wall (W)	h avg (W/m^2-K)	T inf (deg C)	
9.8433	1147	49.5	Single Phase
10.052	1471.8	49.3	Two-Phase Subcooled
19.376	2610.8	56.6	Two-Phase Saturated
36.464	4478.3	56.6	Two-Phase Saturated

Code Outputs					
ΔTs (FEA)	ΔTs (Real)	%diff	ΔTwall(FEA)	ΔTwall(Real)	%diff
30.1	18.6	61.6	34.4	42.9	19.8
21.6	11.1	94.9	25.9	33.1	21.6
28.9	12.3	134.0	36.7	39.4	7.0
27.9	12.8	117.2	41.1	45.7	10.1
	Mean	**101.9**		**Mean**	**14.6**

Table 8: Comparison of FEA and experimental results for HLM1, 200-2 test section and G=1069 kg/m^2-s.

Heat Loss Method 2			
Code Inputs			
q wall (W)	h avg (W/m^2-K)	T inf (deg C)	
9.8433	1147	49.5	Single Phase
10.052	1471.8	49.3	Two-Phase Subcooled
19.376	2610.8	56.6	Two-Phase Saturated
36.464	4478.3	56.6	Two-Phase Saturated

Code Outputs					
ΔTs(FEA)	ΔTs (Real)	%diff	ΔTwall(FEA)	ΔTwall(Real)	%diff
17.6	18.5	4.4	23.0	28.7	19.8
10.4	11.1	6.1	15.6	19.5	20.4
14.3	12.3	15.6	22.3	22.6	1.3
10.5	12.8	17.9	22.2	23.1	4.0
	Mean	**11.0**		**Mean**	**11.4**

Table 9: Comparison of FEA and experimental results for HLM2, 200-2 test section and G=1069 kg/m^2-s.

4.5.3 Results of Temperature sensors

As shown in Figure 70 the in-channel temperature sensors did not give use axial fluid temperature as previously hoped but some Pyrex surface temperature that tracks the silicon surface temperature qualitatively due to conduction effects from the fin portions of the channels. The following section will discuss the qualitative interpretation of the data collected from the in-channel sensors. Figure 71 gives the spatial locations of the sensors and their assigned notation.

The data presented in this section was collected from the 200-2 test section at mass fluxes of G=535, 1069, and 2139 kg/m^2-s. It is also important to mention that the data from sensors T1-T4 will not be presented due to a power lead failure. Also the data from sensors T9-T12 will not be presented because channel to channel interaction will not be discussed in this thesis. Therefore the only data presented is for sensors T5-T8.

Figures 73-75 show data from sensors T5-T8 plotted along with T_{wall} for three different values of mass flux. An obvious characteristic of all three plots is at a given heat flux in the single phase portion of the curve that the sensors show an increase in temperature in the axial direction, as expected. Once boiling is initiated in the channels, the values of all the sensors collapse back to a minimal difference due to the drastic increase in heat transfer coefficient. The qualitative differences in these three plots are deduced once two-phase heat transfer is initiated.

For the case of the highest mass flux shown in Figure 73, the sensors display an almost perfectly vertical path indicating a continual substantial increase in heat transfer coefficient for the range of heat flux applied. The case of the medium mass flux in Figure 74, the sensors displays a slight curvature in the positive direction indicating a slight diminishing returns effect in terms of the heat transfer coefficient. The case of the lowest mass flux in Figure 75, the sensors display the same trend as Figure 74 but on a much more profound magnitude. This plot clearly indicates a decreasing heat transfer coefficient in the axial direction which matches similar reports made by Qu and Mudawar [2003]. This may be attributed to the high values of quality experienced during these low flow rates which reached values close to 0.6. Figures 76-79 are of the exact same data but each sensor is plotted individually and all three flow rates are display on each plot.

Because the in-channel sensors are located on the Pyrex and not the heated surface, it would be quite difficult to extract local heat transfer coefficients from the given data. This design of in-channel sensor could be easily altered for this purpose by replacing the Pyrex cover with a silicon substrate. By performing a silicon-to-silicon bond operation and heating the specimen from both sides, local surface temperature measurements from the heated surface could be attained at the expense of visualization.

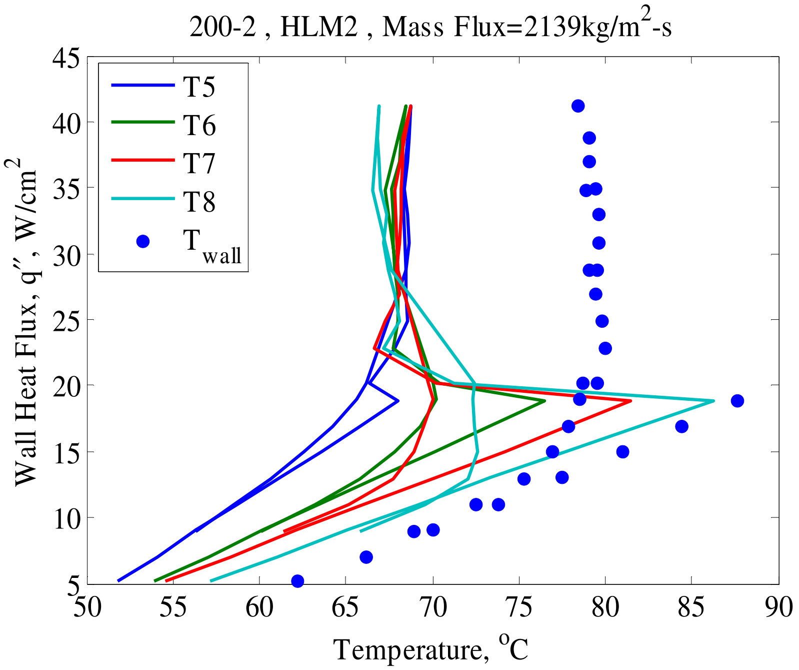

Figure 73: In-channel temperature sensors T5-T8 for a mass flux of G=2139 kg/m^2-s for the 200-2 tests section.

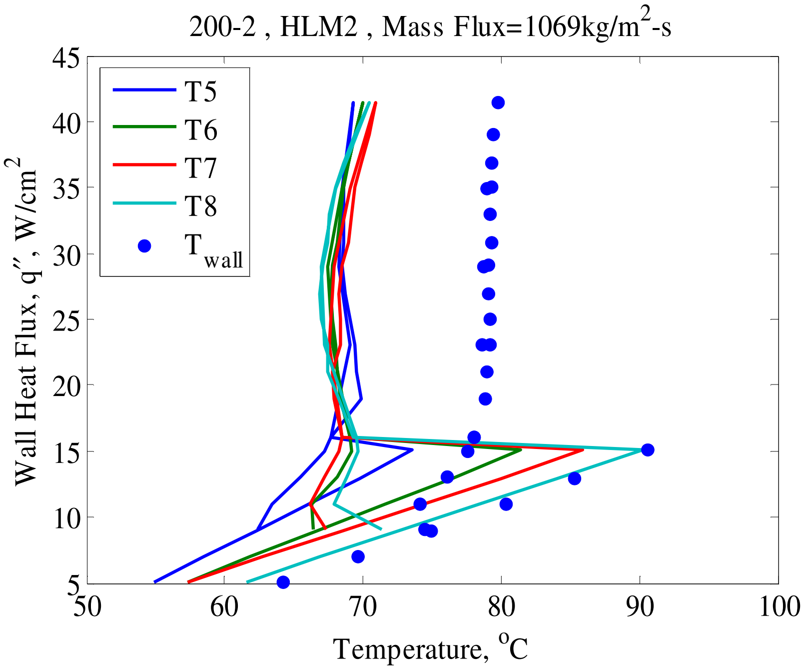

Figure 74: In-channel temperature sensors T5-T8 for a mass flux of G=1069 kg/m^2-s for the 200-2 tests section.

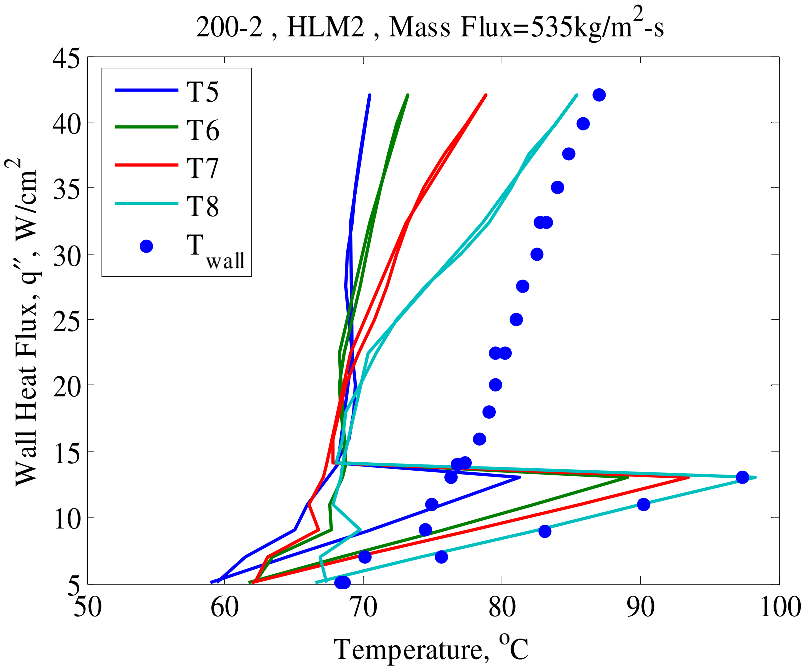

Figure 75: In-channel temperature sensors T5-T8 for a mass flux of G=535 kg/m^2-s for the 200-2 tests section.

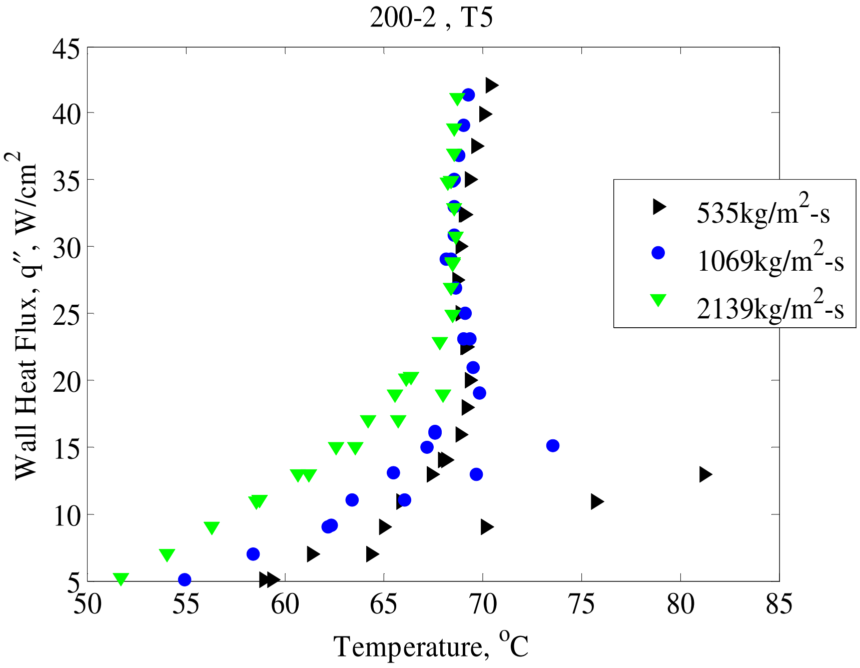

Figure 76: In-channel temperature sensor T5 for three values of mass flux for the 200-2 tests section.

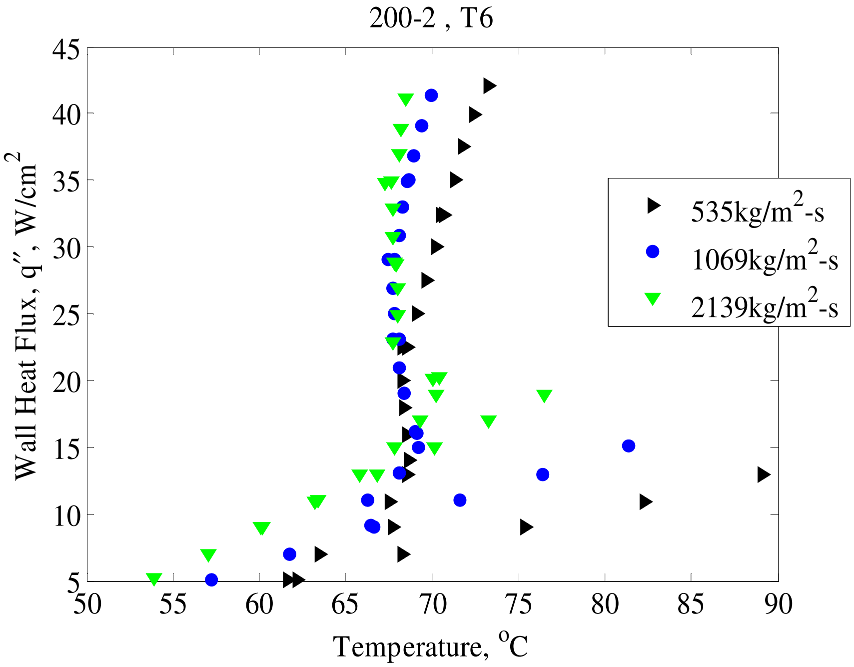

Figure 77: In-channel temperature sensor T6 for three values of mass flux for the 200-2 tests section.

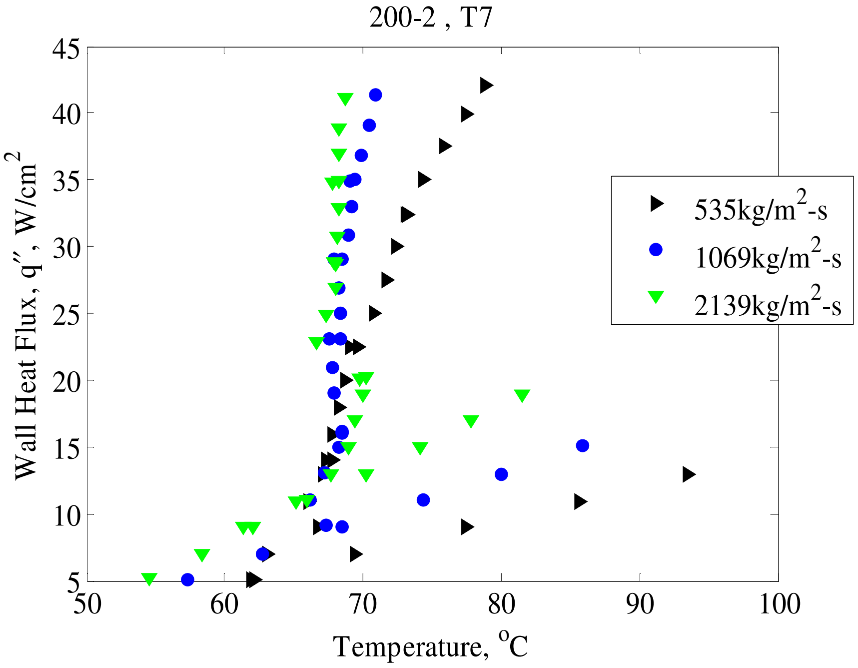

Figure 78: In-channel temperature sensor T7 for three values of mass flux for the 200-2 tests section.

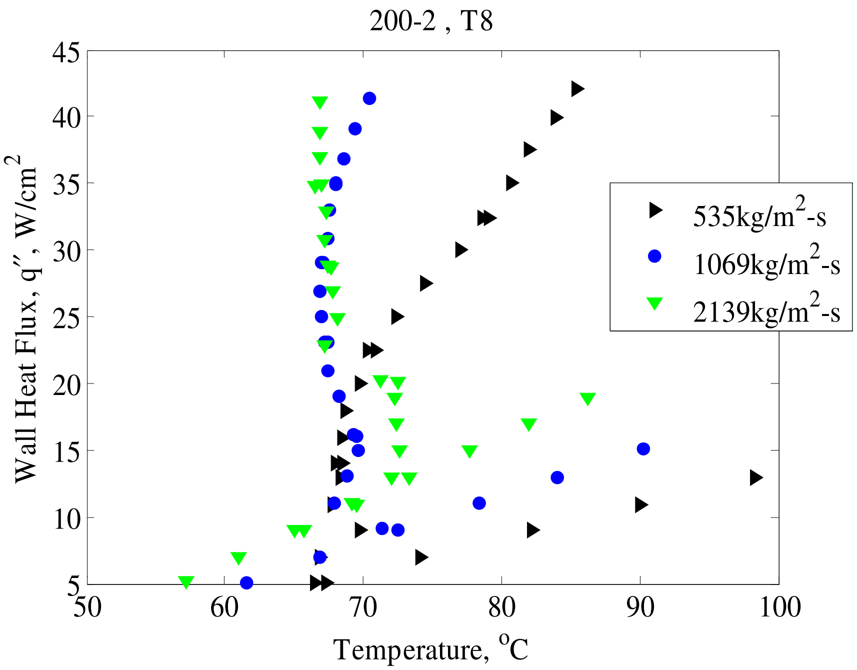

Figure 79: In-channel temperature sensor T8 for three values of mass flux for the 200-2 tests section.

4.6 Discussion of flow instabilities

The stability of two phase flow in microchannels is essential for the reliable cooling of high heat flux applications. As mentioned in Chapter 1, several researchers have tackled this problem from several standpoints. There are two boiling mechanisums in two-phase heat transfer. One type is convective boiling where the quality is high enough to induce annular flow. This mechanism transports heat from the heated surface to the vapor core across a thin evaporative film that lines the channel walls. The second mechanism is nucleation boiling where by random imperfections in the heated surface serve as vapor generating sites both these nucleation mechanisms are difficult to predict from a global standpoint and serve to add to the complexity of the system.

The mechanism leading to the instability of the system is the rapid expansion of vapor in the channel causing tremendous acceleration of the flow. This acceleration increases the pressure drop causing the flow to back up in the channels into the up stream compressible volume. Depending on the type of flow delivery system, whether constant flow rate or constant pressure drop, these fluctuations can be quite severe and last for tens of seconds. Many researchers like Balasubramanian and Kandlikar [2004], have claimed to dampen if not eliminate these effects by placing a control valve directly up stream of the test section to reduce the compressible volume that the instability sees.

The current study has sought to alleviate one of these instability-causing mechanisms by placing geometrically consistent vapor generating sites in the base of the channels, the point of highest heat application. By generating vapor from spatially consistent locations it may serve to reduce some of the thermal transients and add some consistency to the vapor generation process. The cavities may also serve to sustain two-phase flow in the bubbly flow regime and postpone the advent of slug formations. This section will attempt to characterize regions of the stability and instability of the current microchannel test sections with respect to flow rate and channel size. For further information on this topic see [Jones [2006]] a companion thesis which covers this in much more detail.

4.6.1 Effect of flow rate on stability

The exact locations of two phase transition points for four different flow rates at a constant sub-cooling of 10^{o}C were recorded. The data gathered for each flow rate were Onset of Nucleate Boiling (ONB) displayed in section 4.3, transition from stable to unstable flow and q_{snuff}, the point at which all vapor generation is snuffed out. Unstable flow is defined as large fluctuations in flow and pressure drop that are typically accompanied by flow reversals into the inlet plenum. Very small random fluctuations from channel-to-channel interaction are present throughout all flow rates and all values of heat flux and are viewed as insignificant in comparison. These channel-to-channel fluctuations are also thought to have no substantial effect on the heat transfer performance of the test sections.

An interesting series of occurrences were noticed specifically at high flow rates. The stability of a test section at a given flow rate could be split up into three main sections that are best visualized by traversing down the boiling curve.

1. Unconditionally stable flow during saturated exit conditions.
2. At lower heat flux, as soon as the exit temperature becomes sub-cooled, an unstable regime is established, noted by large scale pressure fluctuations.
3. At a lower value of heat flux, but still in the sub-cooled boiling region, the flow transitions back into a stable two phase flow regime which continues as heat flux decreases until all nucleation activity is snuffed out.

Figures 80 and 81 display these stability transition points in two different graphical methods. Figure 80 shows the actual points of saturation, unstable to stable transition and the q_{snuff} or single phase transition. Since every data point encountered above the saturation point was stable, the focus of the two figures is on the growth of the sub-cooled stable region with flow rate. Figure 81 illustrates the growth of the stable sub-cooled region with flow rate quite well along with the diminishing extent of the unstable sub-cooled region.

It is believed that the cavities placed in the channels for this study cause the large regions of stability seen throughout a wide range of conditions. All data was taken with a throttling valve in line but turned all the way open. Hetsroni, et al. [2002] conducted experiments on a silicon heat sink capped by Pyrex in a similar fashion to the current studies. The working fluid in that study was Vertrel XF which is very similar in properties to FC72 that can be view in a table in Appendix A. The channels in that study had no cavities and large scale instabilities were reported well into the saturation flow region. High-speed photography confirmed that the cavities serve as stable nucleation sites releasing vapor bubbles at a constant and uniform rate.

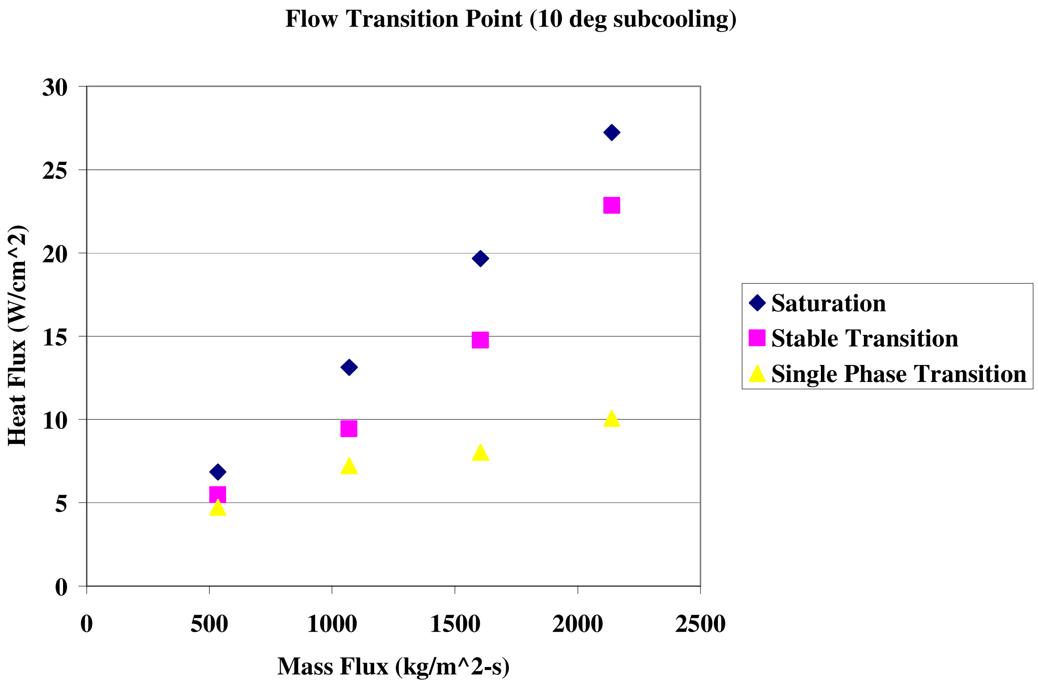

Figure 80: Stability transition points for four values of mass flux for test section 200-2.

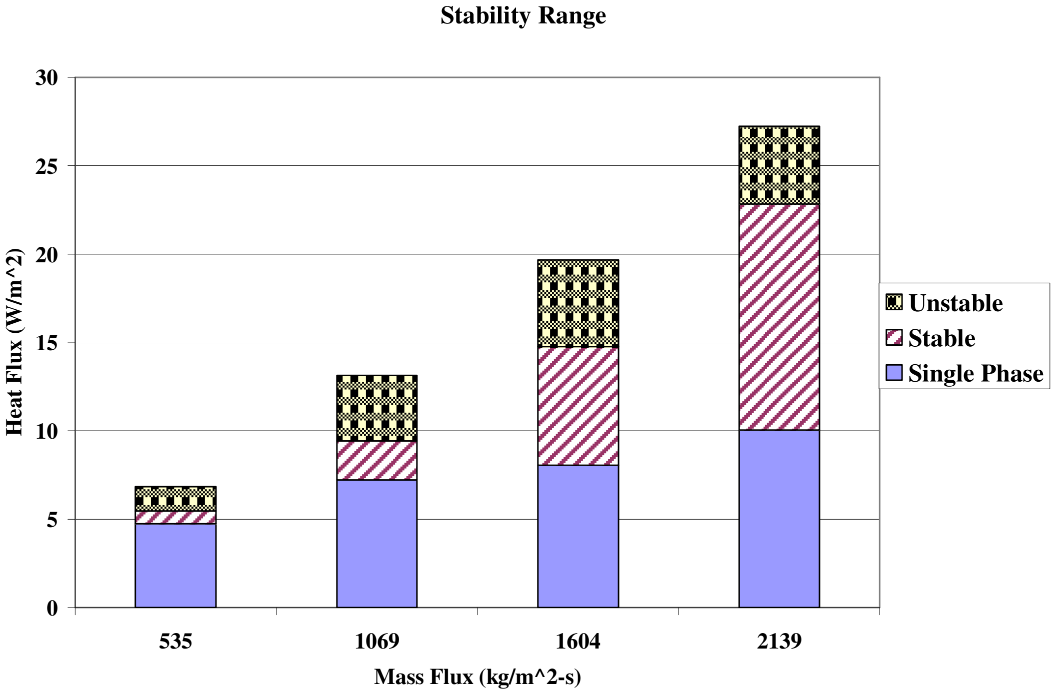

Figure 81: Stability region growth for four values of mass flux for test section 200-2.

4.6.2 Effect of channel size on stability

Another interesting variable that effected stability was the channel size of the test section. When conducting test on the 400-6 test section the same regions were encountered, only larger in range. Figure 82 displays the difference in the ranges of the stable and unstable regions of flow when comparing the 200-2 test section to the 400-6 test section. The growth of the stable sub-cooled range for the larger channels is attributed to the additional volume for the vapor to expand without engulfing the entire channel. Another interesting point to be made is that the single phase transition of q_{snuff} shows that it is minimally affected by the flow rate.

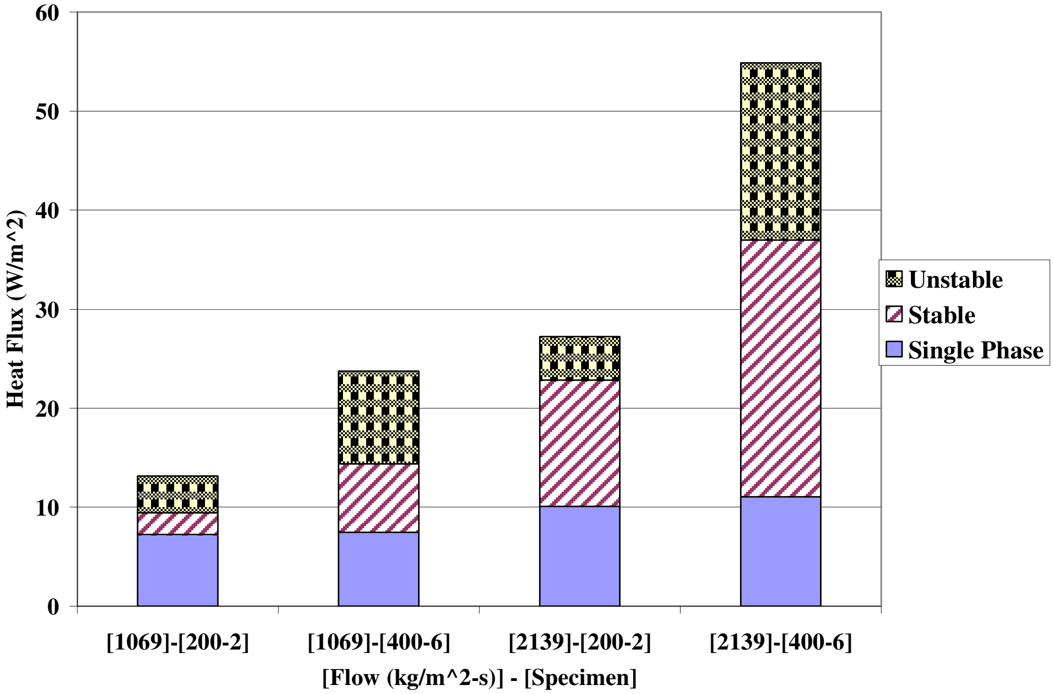

Figure 82: Stability region growth for 10oC of sub-cooling and two values of mass flux for test section 200-2 and 400-6.

4.6.3 Visual depiction of instabilities

As previously mentioned the instabilities are indicated by large scale fluctuations in flow and pressure drop. These regions were filmed by a high speed camera at 400fps were the stable regions for sub-cooled and saturated exit conditions. A limited amount of footage was filmed at 10,000fps but will not be presented in this thesis. For further information on these images see [Jones [2006]] a companion thesis.

Figure 83 shows still frames from the 400-6 test sections for conditions of stable saturated and stable sub-cooled exit conditions. With this camera and lighting configuration the vapor shows up as the regions of white. A distinct difference in the saturated and sub-cooled pictures in Figure 83 is the difference of size in the vapor plums exiting the test sections. While the vapor for the saturated case continues to exit the test section on its way to the condenser, the vapor frpm the sub-cooled case condenses and collapses directly after exiting the microchannel array.

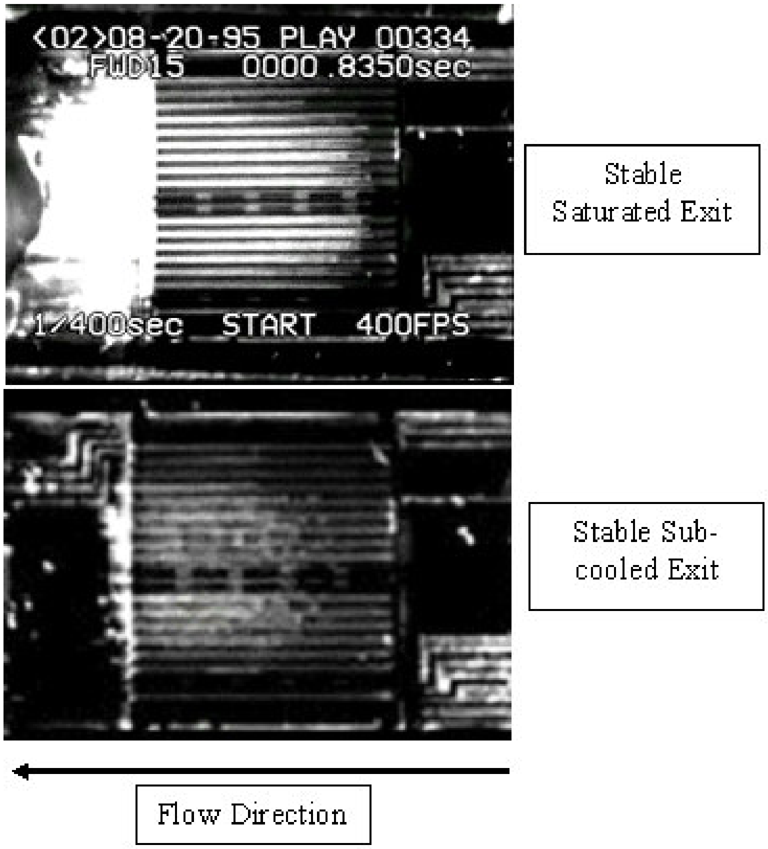

Figure 83: Pictorial depiction of stable sub-cooled and saturated exit conditions for test section 400-6 at G=2139 kg/m^2-s.

Figure 84 gives a sequenced pictorial representation of one full cycle of the unstable action seen in this study where frame 1 and 12 are the same points in the cycle. These images were recorded for the 200-2 test section at a mass flux of G=535 kg/m^2-s at sub-cooled exit conditions due to the visual magnitude of the fluctuation being greater at the lower flow rates. As can be seen from the images in Figures 83 and 84, a wide range of visual conditions were encountered during the current study.

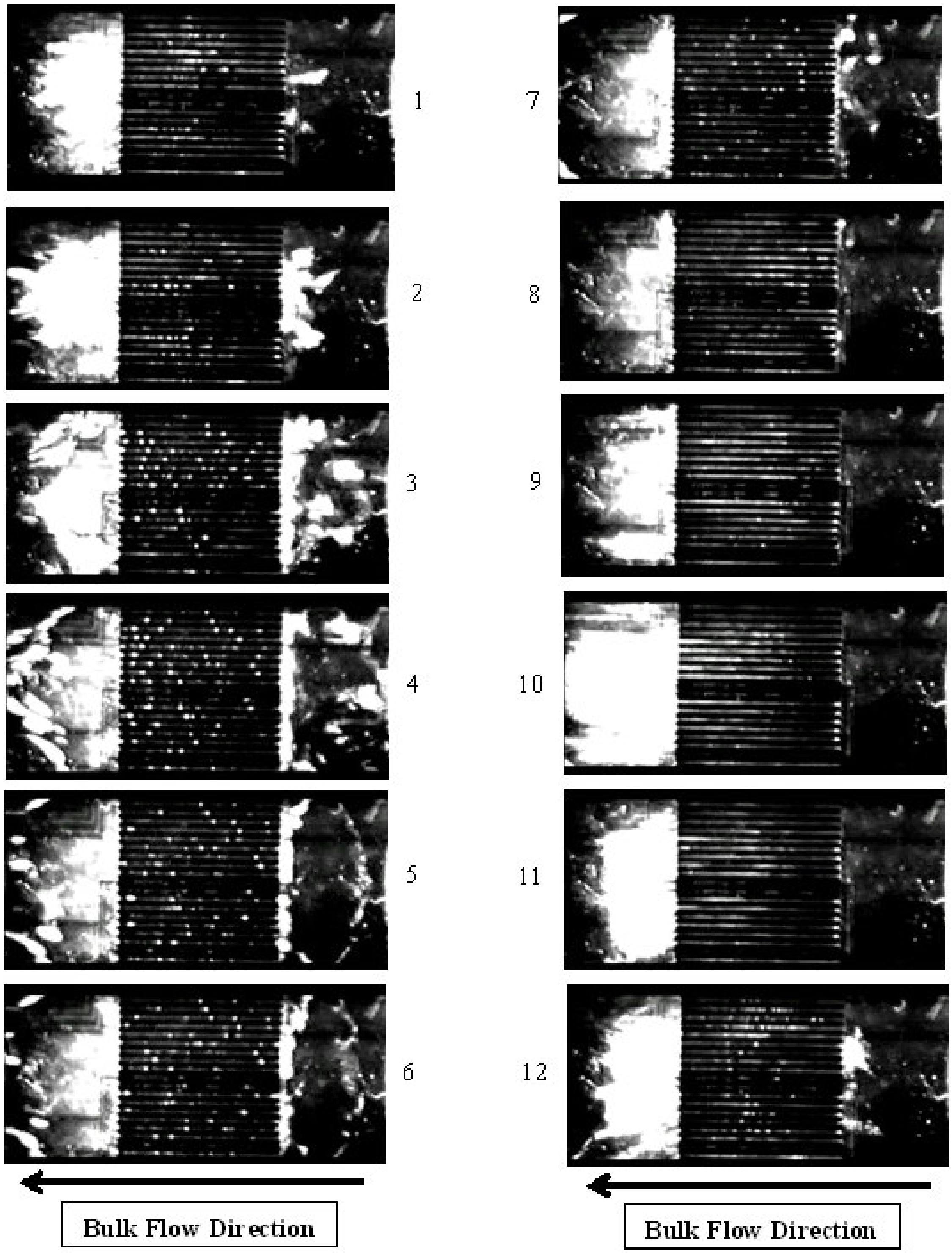

Figure 84: Numbered sequential display of large scale flow fluctuations.

4.7 Frequency analysis of instabilities

There are several was to graphically display the instabilities in this study. This section is dedicated to this purpose. Using the data from the pressure sensors located at the inlet and outlet as well as the in-channel temperature sensors, this study will attempt to shed some light on the characteristics of the instabilities.

4.7.1 Pressure drop compared by channel size

The pressure drop plots displayed in Figure 85 show the expected behavior of an increase in pressure drop at a given heat flux value for a smaller diameter test section as opposed to the larger. These plots also show the gradual decrease in pressure drop as a function of heat flux due the reduction of viscosity for the single phase portion of the curves. Another noticeable trait is the sharp change in the slopes of both curves approximately half way up the two-phase portion. As indicated on both curves, these are the regions of instability for both the 200-2 and 400-6 test sections at this given mass flux.

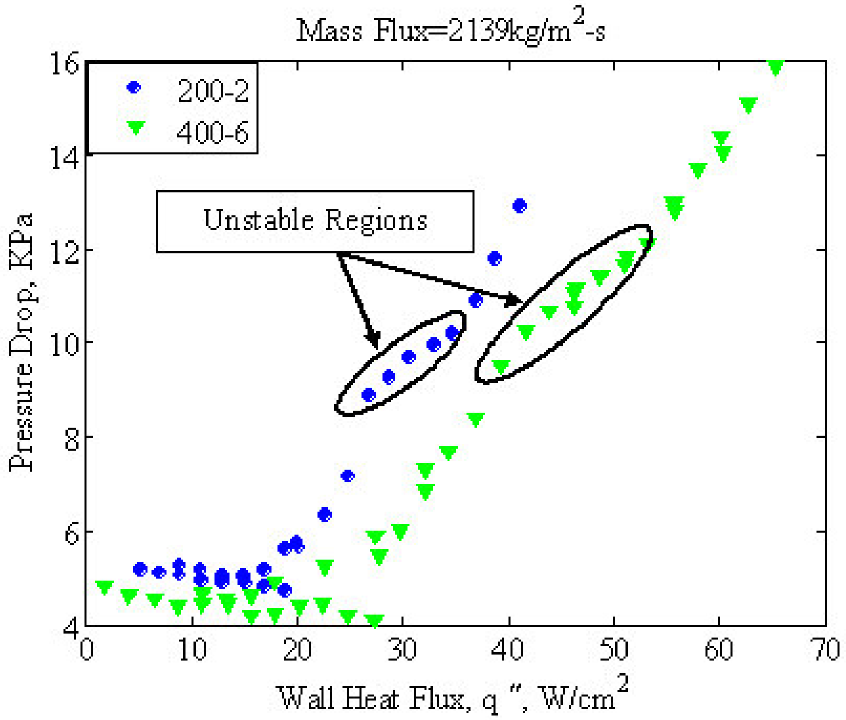

Figure 85: Two phase pressure drop for test sections 200-2 and 400-6.

4.7.2 Pressure drop versus temperature sensor signal

Large scale pressure and flow fluctuations have been reported to cause analogous surface temperature fluctuations. The current study has sought to make more use of the in-channel temperature sensors by comparing their transient values during unstable regions against those of the pressure sensors. This analysis consists of plotting the data from the pressure sensors and the in-channel temperature sensors against time as seen in Figure 86. Looking at the data in this form can provide the maximum and minimum of the fluctuations of both variables. Then by subjecting these data to a Fast Fourier Transform (FFT) analysis and plotting in the frequency domain as seen in Figure 87, it can be deduced if the fluctuation in both sensors is at the same frequency.

During the analysis for the 200-2 test section, a range of dominant frequencies were encountered at different values of heat flux. To demonstrate that the temperature fluctuations track the pressure fluctuations the data is presented at two different values of heat flux, which were characterized by two different dominant frequencies.

Figures 86 and 87 are characterized by an 8.7Hz fluctuation that can be seen in both the pressure signal as well as the in-channel temperature sensor signal displayed in the frequency domain in Figure 87. These data were recorded at a heat applied q_{wall} of 26.4W that resulted in a temperature fluctuation of approximately 4°C. Figures 88 and 89 are characterized by a 13.5Hz fluctuation that can be seen in both the pressure signal as well as the in-channel temperature sensor signal displayed in the frequency domain in Figure 89. These data were recorded at a heat applied (q_{wall}) of 22.5W, and imposed a temperature fluctuation of approximately 3°C.

By comparing the data of these two scenarios it can be deduced that one set of conditions are dominated by a low frequency, large amplitude oscillation and the other by a higher frequency, smaller amplitude oscillation. It can also be speculated that the temperature fluctuations of the silicon surface are much greater than that of the in-channel sensors due to the drastic differences in the thermal conductivities of the two substrates. During thermal transients' situations such as the drastic change in heat transfer coefficient as seen during flow oscillations, a low thermal conductivity substrate such as Pyrex can provide a damping effect on the magnitude of the fluctuation.

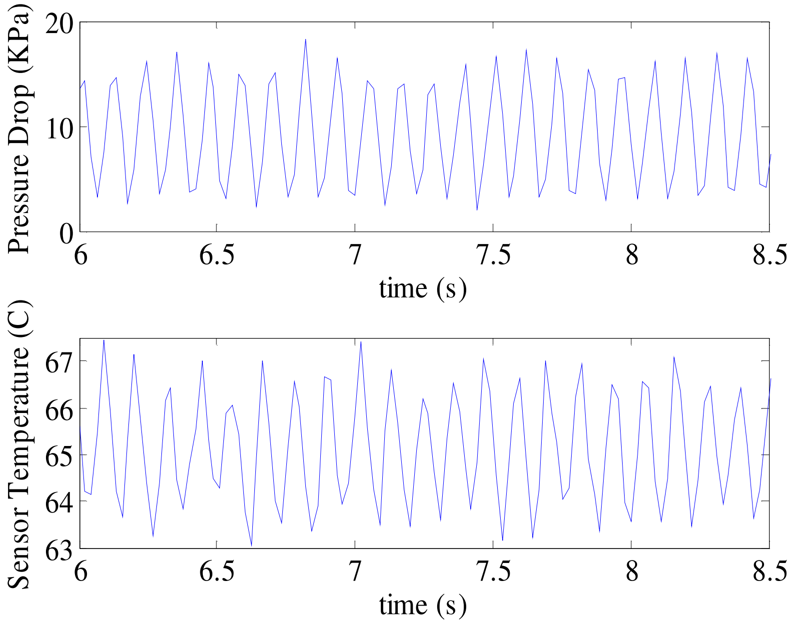

Figure 86: Magnitudes of pressure and in-channel temperature sensor fluctuations with time, G=2139 kg/m^2-s, 200-2, q_{wall}=26.44W.

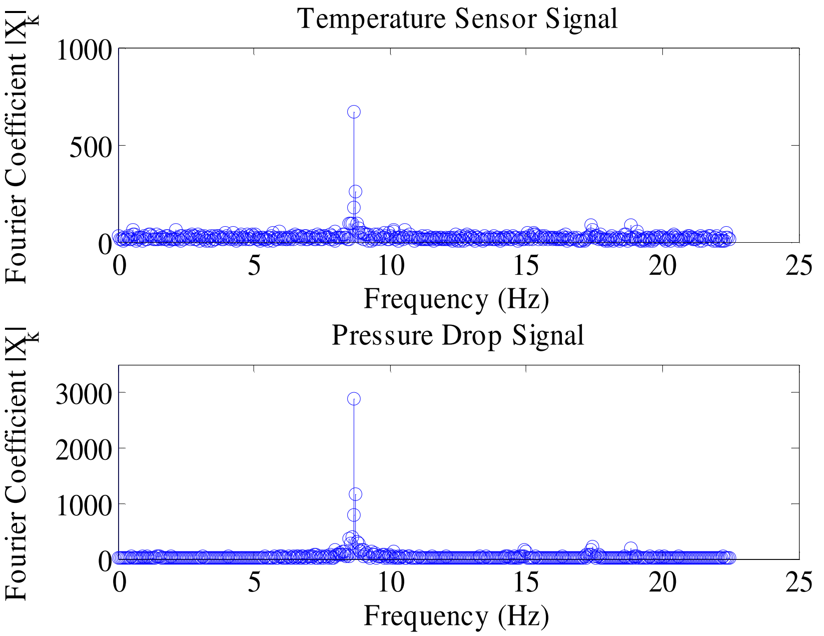

Figure 87: Magnitudes of FFT Coefficient for the pressure and in-channel temperature sensor fluctuations, G=2139 kg/m^2-s, 200-2, q_{wall}=26.44W.

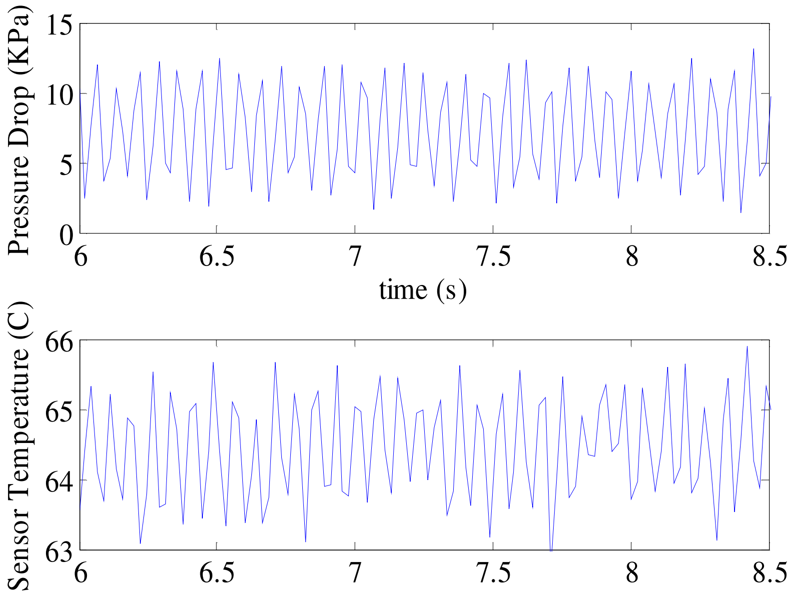

Figure 88: Magnitudes of pressure and in-channel temperature sensor fluctuations with time, G=2139 kg/m^2-s, 200-2, q_{wall}=22.5W.

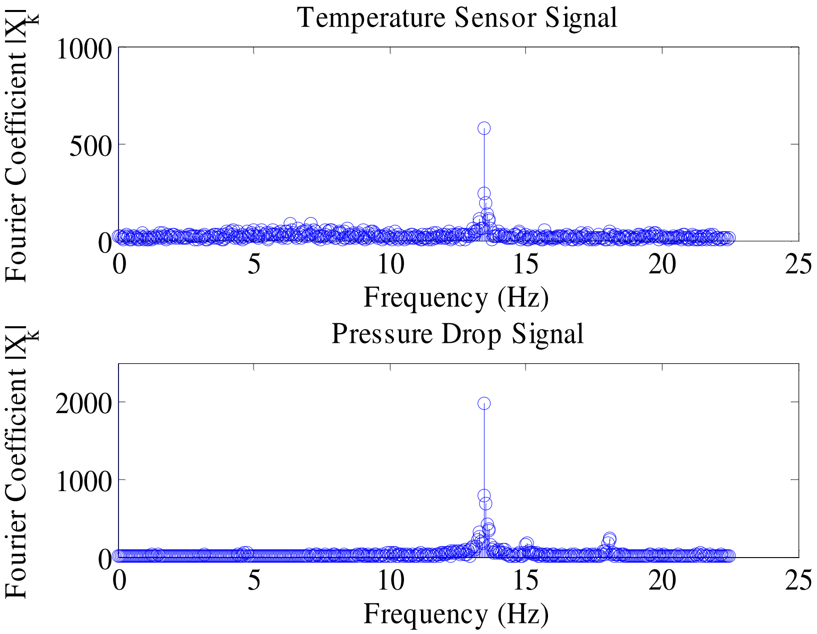

Figure 89: Magnitudes of FFT Coefficient for the pressure and in-channel temperature sensor fluctuations, G=2139 kg/m^2-s, 200-2, q_{wall}=22.5W.

4.7.3 Dominant Frequency by flow rate

As mentioned in the previous analysis, the dominant frequency of the unstable oscillation changed at a given flow rate for different values of heat flux. A limited amount of data is available for this portion of the analysis due to insufficient amounts of data collected in the unstable range at the lower flow rates. Therefore only data from the mass fluxes of 1069 and 2139 kg/m^2-s will be displayed. Figure 90 shows the dominant frequency data for the 200-6 and 200-2 test sections.

The data for 200-2 at 2139 kg/m^2-s, portray a gradual increase from 8-9Hz in frequency as heat flux decreases. This continues until the transition to stable sub-cooled exit conditions where the frequency increases dramatically directly before the transition point. This same trend can also be seen for the 200-2 test section at 1069 kg/m^2-s but is supported by a smaller set of data. Figure 90 also shows the dominant frequency data for the 200-6 test section. The data for 200-6 at both values of mass flux portray a gradual increase as well but are constantly lower than the frequencies of the 200-2 test section.

Figure 91 displays the dominant frequencies for a mass flux of 2139 kg/m^2-s for three test sections. The dominant frequency curve for the 400-6 test section shows a gradual increase in frequency as heat flux decreases, and like the 200-6 test section, shows no sign of spiking before transition. Throughout all the experimentation of the 6 cavity arrangements, both 400-6 and 200-6, the high frequency transition was never observed as seen in the 200-2 configuration. Additional analysis of this spike in frequency at the onset of the stable sub-cooled flow regime is warranted.

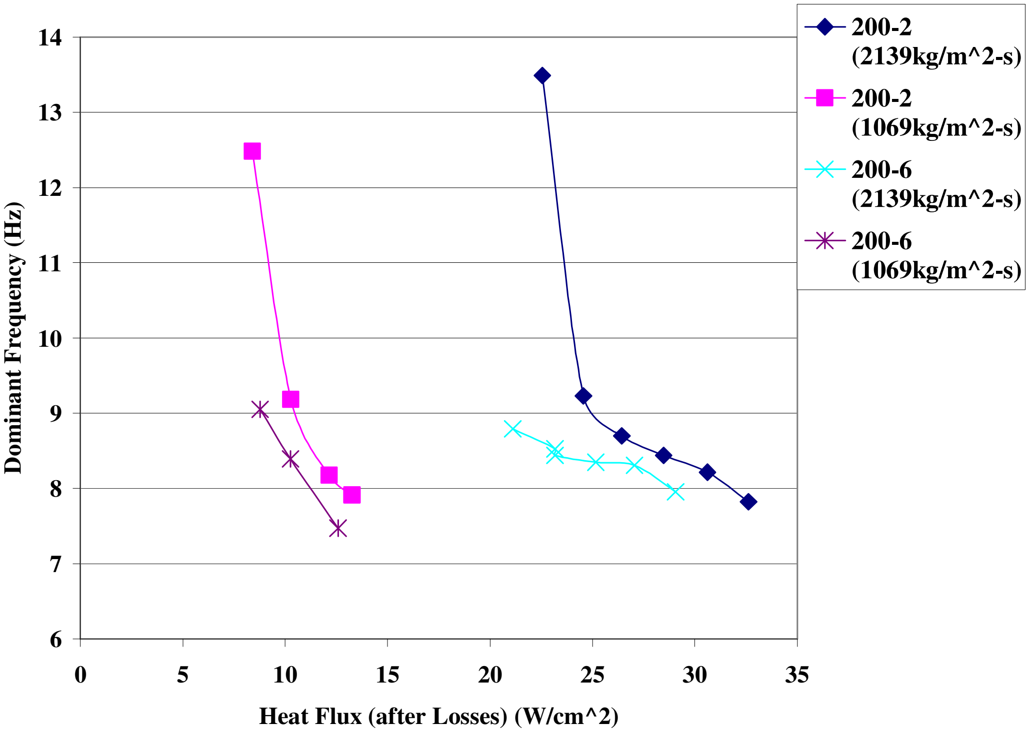

Figure 90: Dominant frequency for 200-2 and 200-6 test sections.

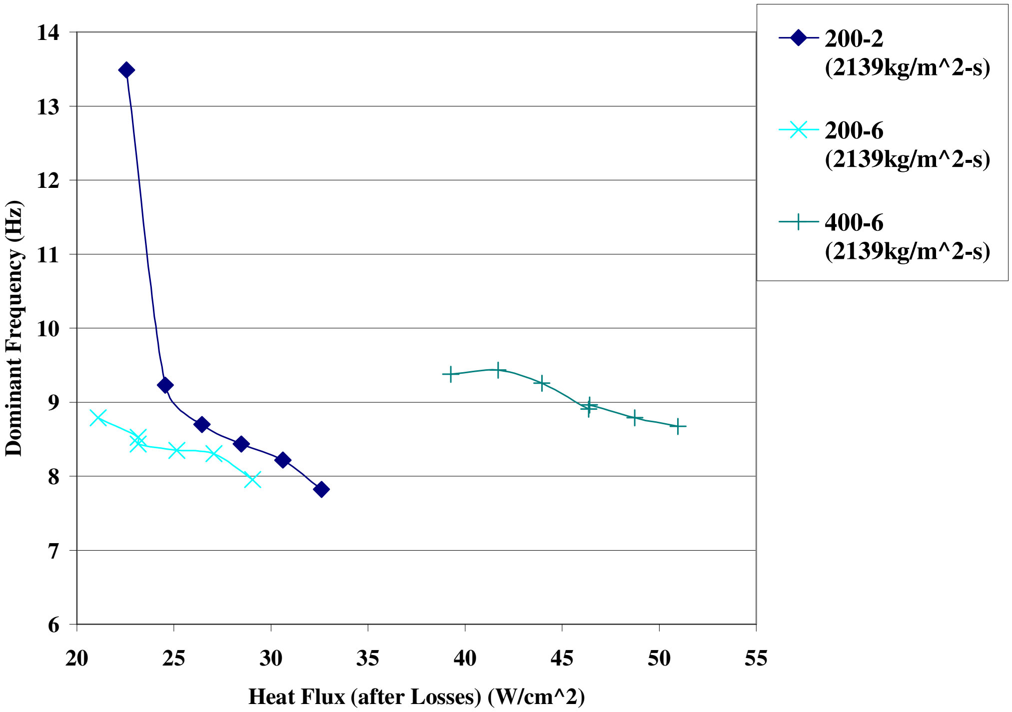

Figure 91: Dominant frequency for 200-2, 200-6, and 400-6 test sections.

CHAPTER 5: CONCLUSIONS

The present study is centered on the design, fabrication and testing of cavity assisted microchannel arrays. Eight microchannel test sections with pyramidal vapor generating cavities etched in the base of the channels were successfully fabricated with various channel configurations and dimensions. These test sections are outfitted with a wide variety of features such as the ability to measure in-channel surface temperatures, provide localized as well as uniform heat flux to the microchannel array, and a transparent cover for visualization purposes. The successful testing of two of the eight test sections [200-2, 400-6] were evaluated for their thermal performance in this thesis. In addition to the data collected by the sensors used, an optical study was performed to characterize different flow situations.

From the boiling curves evaluated, temperature overshoot or boiling curve hysteresis values were collected for three flow rates. A maximum overshoot value of 21^{o}C was recorded and a trend of decreasing overshoot value with increasing flow rate was observed. This leads the researchers to believe the ability of the cavities to prematurely trigger ONB was snuffed out by the highly wetting nature of the working fluid FC72.

The average heat transfer coefficient was tabulated and displayed to have a maximum value of 9900W/m^{2}-K at a mass flux of 1069 kg/m2-s. The two phase heat transfer coefficient was also compared against several existing correlations. A correlation developed by Shah [1997] for sub-cooled nucleate boiling showed good agreement with the experimental data. Also a correlation developed by Tran, et al. [1995] for saturated nucleate boiling showed good agreement with the experimental data. Both correlations for sub-cooled and saturated conditions were developed for mini to macro channel size conditions but showed a deviation of less than 18% from the current studies experimental data, a value that is considered excellent for two-phase studies.

Two separate methods for evaluating heat loss were developed and compared for their effect on the reported thermal performance of the test sections. Using an FEA model along with dependent and independent variables associated with both methods of loss, the HLM2 appears to be more correct.

Ranges of flow stability are mapped out and are found to be a function of both flow rate and channel size. Trend of increasing stability range for the sub-cooled stable region are observed for an increasing flow rate as well as increasing hydraulic diameter. The wide range of stable conditions observed by this study is believed to be caused by the stable, consistent vapor generation from the pyramidal cavities etched in the base of the channels.

Transient data was collected during the unstable potions of the flow. This data was analyzed to confirm the direct relationship of in-channel temperature fluctuations with pressure drop fluctuations by plotting data from both sensors at two different unstable conditions and matching the dominant frequencies. This analysis reveals a maximum temperature fluctuation of +/- 4^{o}C for the in-channel surface of the Pyrex lid. This magnitude can only be amplified when reference to the temperature oscillation of the silicon due to the drastic differences in the thermal conductivity.

REFERENCES

Balasubramanian, P., and Kandlikar, S. G., 2005, “Experimental Study of Flow Patterns, Pressure Drop, and Flow Instabilities in Parallel Rectangular Minichannels,” Heat Transfer Engineering, Vol. 26(3), pp. 20-27.

Bergles, A. E., and Kandlikar, S. G., 2005, “On the Nature of Critical Heat Flux in Microchannels,” Journal of Heat Transfer, Vol. 127, pp. 101-107.

Bowers, M.B., and Mudawar, I., 1994, “High Flux Boiling in Low Flow Rate, Low Pressure Drop Mini-channel and Micro-channel Heat Sinks,” International Journal of Heat and Mass Transfer, Vol. 37, pp321-332.

Figliola, R. S., Beasley, D. E., Theory and Design for Mechanical Measurements. Third Edition. New York; John Wiley & Sons, Inc., c2000, pp. 289-292.

Hetsroni, G., Mosyak, A., and Segal, Z., 2001, “Non-Uniform Temperature Distribution in Electronic Devices Cooled by Flow in Parallel Microchannels,” IEEE Transactions on Components and Packaging Technologies, Vol 24, No. 1, pp.16-23.

Hetsroni, G., Mosyak, A., Segal, Z., and Ziskind, G., 2002, “A uniform temperature heat sink for cooling of electronic devices,” International Journal of Heat and Mass Transfer, Vol. 45 pp. 3275-3286.

Hetsroni, G., Mosyak, A., Segal, Z., and Pogrebnyak, E., 2003, “Two-phase flow patterns in parallel micro-channels,” International Journal of Multiphase Flow, Vol. 29 pp. 341-360.

Jakaboski, B. E., Joshi, Y., and Rightley, M., 2004, Forced Convection in a Microchannel Heat Sink Using Carbon Nanotubes for Heat Transfer Enhancement, Proceedings of IMECE-2004-60876

Jiang, L., Wong, M., and Zohar, Y., 1999, “Phase Change in MicroChannel Heat Sinks with Integrated Temperature Sensors,” Journal of Microelectromechanical Systems, Vol. 8(4), pp. 358-365.

Jiang, L., Mikkelsen, J-M. K., Huber, D., Yao, S., Zhang, L., Zhou, P., Maveety, J. G., Prasher, R., Santiago, J. G., Kenny, T. W., and Goodson, K. E., 2002, “Closed-Loop Electroosmotic Microchannel Cooling System for VLSI Circuits,” IEEE Transactions on Components and Packaging Technologies, Vol. 25(3), pp. 347-355.

Kramer, T. A., Flynn, R. D., Fogg, D. W., Wang, E. N., Hidrovo, C. H., and Goodson, K. E., 2004, Microchannel Experimental Structure for Measuring Temperature Fields During Convective Boiling, Proceedings of IMECE-2004-61936

Kandlikar, S. G., 2002, “Fundamental Issues Related to Flow Boiling in Minichannels and Microchannels,” Experimental Thermal and Fluid Science, Vol 26, pp. 389-407.

Kandlikar, S. G., and Grande, W. J., 2003, “Evolution of Microchannel Flow Passages – Thermohydraulic Performance and Fabrication Technology,” Heat Transfer Engineering, Vol. 24(1), pp. 3-17.

Kandlikar, S. G., and Balasubramanian, P., 2004, “An Extension of the Flow Boiling Correlation to Transition, Laminar, and Deep Laminar Flows in Minichannels and Microchannels,” Heat Transfer Engineering, Vol. 25(3), pp. 86-93.

Kandlikar, S. G., 2004, “Heat Transfer Mechanisms During Flow Boiling in Microchannels,” Journal of Heat Transfer, Vol. 126, pp. 8-16

Kosar, A., Kuo, C.-J., and Peles, Y., 2005a, “Boiling heat transfer in rectangular microchannels with reentrant cavities,” International Journal of Heat and Mass Transfer, Vol. 48, pp. 4867-4886.

Kosar, A., Kuo, C.-J., and Peles, Y., 2005b, “Reduced Pressure Boiling Heat Transfer in Rectangular Microchannels With Interconnected Reentrant Cavities,” Journal of Heat Transfer, Vol. 127, pp. 1106-1114.

Kuo, C.-J., Kosar, A., Jensen, M. K., and Peles, Y., 2005c, Boiling in enhanced surface microchannels, Proceedings of IMECE2005-82846.

Lazarek, G. M., and Black, S. H., 1981, “Evaporative Heat Transfer, Pressure Drop and Critical Heat Flux in a Small Vertical Tube With R-113,” International Journal of Heat and Mass Transfer, Vol. 25(7), pp. 945-960.

Lee, H. J., and Lee, S. Y., 2001, “Heat transfer correlation for boiling flows in small rectangular horizontal channels with low aspect ratios,” International Journal of Multiphase Flow, Vol. 27, pp. 2043-2062.

Liu, D., and Garimella, S. V., 2003, Analysis and Optimization of the Thermal Performance of Microchannel Heat Sinks, Proceedings of IPack2003-35260

Liu, D., Lee, P.-S., and Garimella, S. V., 2005, “Prediction of the Onset of Nucleate Boiling in Microchannel Flow,” International Journal of Heat and Mass Transfer, Vol. 48, pp. 5134-5149.

Liu, D., and Garimella, S. V., 2005, Flow Boiling in Microchannel Heat Sink, Proceedings of IMECE2005-79555
Mishima, K., and Hibiki, T., 1996, “Some Characteristics of Air-Water Two-Phase Flow in Small Diameter Vertical Tubes,” International Journal of Multiphase Flow, Vol. 22, pp 703-712

Mukherjee, S., and Mudawar, I., 2003 “Pumpless Loop for Narrow Channel and Micro-Channel Boiling,” Journal of Electronic Packaging, Vol. 125, pp 431-441.

Murthy, S., Joshi, Y., and Nakayama, W., 2004 “Two-Phase Heat Spreaders Utilizing Microfabricated Boiling Enhancement Structures,” Heat Transfer Engineering, Vol. 25, pp 26-36

Nimkar, N. D., Bhavnani, S. H., Ellis, C. D., and Jaeger, R. C., 2004a “Development of an anodically-bonded test surface to obtain fundamental liquid immersion thermal management data for electronic devices ,” Sensors and Actuators A, Vol. 113(2), pp 212-217

Nimkar, N. D., Bhavnani, S. H., and Jaeger, R. C., 2004b Nucleation Char. Of a structured surface in a dielectric coolant in the absence of spreading effects, Proceedings of ITherm2004- pp. 82-89

Park, H., Pak, J. J., Son, S. Y., Lim, G., and Song, I., 2003 “Fabrication of a microchannel integrated with inner sensors and the analysis of its laminar flow characteristics,” Sensors and Actuators A, Vol. 103, pp 317-329

Prasher, R., Mahajan, R., and Chiu, C., 2006 “Thermal Management of High Performance Silicon Devices,” Tutorials Keynotes and Panels of ITherm 2006

Qu, W., and Mudawar, I., 2002, “Prediction and measurement of incipient boiling heat flux in micro-channel heat sinks,” International Journal of Heat and Mass Transfer, Vol. 45, pp. 3933-3945

Qu, W., and Mudawar, I., 2003a, “Measurement and Prediction of Pressure Drop in Two-Phase Microchannel Heat Sinks,” International Journal of Heat and Mass Transfer, Vol. 46, pp. 2737-2753

Qu, W., and Mudawar, I., 2003b, “Flow Boiling Heat Transfer in Two-Phase Microchannel Heat Sinks – I. Experimental Investigation and Assessment of Correlation Methods,” International Journal of Heat and Mass Transfer, Vol. 46, pp. 2755-2771

Qu, W., and Mudawar, I., 2003c, "Flow Boiling Heat Transfer in Two-Phase Microchannel Heat Sinks – II. Annular Two-Phase Flow Model," International Journal of Heat and Mass Transfer, Vol. 46, pp. 2773-2784.

Qu, W., and Mudawar, I., 2003d, "Thermal Design Methodology for High-Heat-Flux Single-Phase and Two-Phase Micro-Channel Heat Sinks," IEEE Transactions on Components and Packaging Technologies, Vol. 26(3), pp. 598-609.
Shah, M. M., 1977, "A General Correlation for Heat Transfer During Subcooled Boiling in Pipes and Annuli," ASHRAE Trans., Vol. 83, pp. 202-217.

Shah, R. K., and London, A. L., Advances in Heat Transfer. Supplement 1. New York; Academic Press, Inc., c1978

Singhal, V., Liu, D., and Garimella, S. V., 2003, Analysis of Pumping Requirements for Microchannel Cooling Systems, Proceedings of IPack2003-35237

Steinke, M. E., and Kandlikar, S. G., 2003, "Control and Effect of Dissolved Air in Water during Flow Boiling in Microchannels," International Journal of Heat and Mass Transfer, Vol. 46

Thome, J. R., 2004, "Boiling in Microchannels: a Review of Experiment and Theory," International Journal of Heat and Fluid Flow, Vol. 25. pp. 128-139

Tran, T. N., Wambsganss, M. W., and France, D. M., 1995, "Small Circular and Rectangular Channel Boiling with two Refrigerants," International Journal of Multiphase Flow, Vol. 22(3), pp. 485-498.

Tuckerman, D. B., and Pease, R. F. W., 1981, "High-Performance Heat Sinking for VLSI," IEEE Electron Device Letters, Vol. EDL-2(5). pp. 126-129

Upadhya, G., Zhou, P., Hom, J., Goodson, K., and Munch, M., 2004, "Electro-Kinetic microchannel cooling system for servers," Proceedings of IEEE-2004

Warrier, G. R., Dhir, V. K., and Momoda, L. A., 2002, "Heat transfer and pressure drop in narrow rectangular channels," Experimental Thermal and Fluid Science, Vol. 26. pp. 53-64.

Webb, R. L., 2003, Effect of manifold design on flow distribution in parallel micro-channels, Proceedings of IPACK2003-35251

Wu, H. Y., and Cheng, P., 2003a, "Liquid/Two-Phase/Vapor Alternating Flow During Boiling in Microchannels at High Heat Flux," Int. Comm. Heat and Mass Transfer, Vol. 30. No 3. pp. 295-302.

Wu, H. Y., and Cheng, P., 2003b, “Visualization and Measurements of Periodic Boiling in Silicon Microchannels,” International Journal of Heat and Mass Transfer, Vol. 46, pp. 2603-2614

Zhang, L., Koo, J.-M., Jiang, L., Asheghi, M., Goodson, K., Santiago, J. G., and Kenny, T. W., 2004, “Measurements and Modeling of Two-Phase Flow in Microchannels with Nearly Constant Heat Flux Boundary Conditions,” Journal of Microelectromechanical Systems, Vol. 11(1), pp. 12-19.

APPENDICES

APPENDIX A

FC 72 PROPERTIES COMPARISON

The properties listed come from two sources. The FC-72 properties are provided by 3M, and properties for Vertrel XF came from Hetsroni [2002].

Properties	FC 72	Vertrel XF	Water
Saturation Temperature, (^{o}C)	56.6	52	100
Liquid Density, (kg/m3)	1619.73	1520	958.3
Surface Tension, (mN/m)	8.27	14.1	58.91
Dynamic Viscosity, (µN-s/m2)	453.7	670	277.5
Specific Heat (J/kg-oK)	1098.4	1130	4220
Latent Heat of Vaporization, (kJ/kg)	84.51	130	2256.7
Thermal Conductivity, (mW/m-oK)	52.1	71.0	679

Table 10: Comparison of FC-72, Vertrel XF, and Water properties.

The properties listed in Table 10 are for basic comparison of two dielectrics spoken about in the current study compared against those for water. The typical characteristics of these fluids are low atmospheric boiling points, low thermal conductivity, low surface tensions, and low latent heat values. The only two of these properties that are truly desired is that they are dielectric and the low boiling points. These two properties could possible be attained using water but not without extremely low pressures and deionization, both of which are costly to maintain.

APPENDIX B

FABRICATION DETAILS

I. Silicon Preparation:

Starting with 4" silicon wafer 500microns thick, double sided polished and crystal orientation of <100>.

1. Cavity Etch: [bottom side of wafer]

- H_2SO_4 +H_2O_2 (2:1) Piranha Clean-----(5min)
    1. may be replaced with Acetone/Methanol, Dehydration bake then Matrix run(AMDM clean)
        - Acetone/Methanol followed by DI rinse
        - Dehydration bake –(20min)—(120deg)
        - Matrix run (3-4 min)
- Rinse DI water -----(5min) and dry with N_2
- Oxidation Furnace -----8000A Oxide over entire wafer-----(2hrs)-----(~1050degC Wet)
- AMDM clean
- HMDS run-----(15)min
- Put Blue Dicing tape on channel side
- Apply Photoresist (5214)-----(3000rpm)-----(30sec)
- Soft Bake-----(90degC)-----(30min)

- Expose Cavity Mask [dark field mask]-----(6sec)
- Developer(400K): water -----(1:2)-----(30sec)
- Rinse DI water-----(1min), dry with N2
- Patch edges, holes, and round plenum corners with paint brush and Photoresist
- Soft Bake-----(90degC)-----(30min)
- Matrix de-scum-----------(10sec)
- Buffered Oxide Etch (BOE) -----(10min or until hydrophobic)
- Remove Blue Dicing tape
- Strip Photoresist with Matrix Run—(4-5 min)
- Quick Buffered Oxide Etch (BOE) -----(30 sec)
- DI Rinse and leave in water until you are ready for TMAH.
- (TMAH) Etch
- Mix one part of 25 % w/w TMAH in two parts of D.I water.

The mixture was heated in a beaker to 80°C. A condenser was used to maintain the pH of the solution by condensing the vapors. A magnetic stirrer maintained a uniform temperature and kept the solution circulating. The circulation also helped in keeping the etch surface free of the hydrogen bubbles evolved during the reaction with silicon.

Ammonium peroxydisulphate (APODS) was added to the solution every 20 minutes. The amount of APODS added depended on the quantity of the solution prepared. One gram of APODS was dissolved in 10 ml. of D.I water for every one liter of the solution. APODS was added to absorb the hydrogen liberated in the reaction.

Etch Rate: Approximately 50 μm in one hour at 80°C. The rate was a function of temperature and the age of the solution. (Nitesh, et al. [2004])

- Rinse DI water -----(5min) and dry with N2

2. Lead Clearance Etch [top side of wafer]

- AMDM clean
- HMDS run-----(15)min
- Put Blue Dicing tape on Cavity side
- Apply Photoresist (5214) -----(3000rpm)-----(30sec)
- Soft Bake-----(90degC)-----(30min)
- Align to Cavity Mask and Expose Clearance Mask [dark field mask] -----(6sec)
- Developer(400K): water -----(1:2)-----(30sec)
- Rinse DI water-----(1min), dry with N2
- Patch edges and holes with Photoresist
- Soft Bake -----(90degC)-----(30min)
- Matrix de-scum-------(13sec)
- Buffered Oxide Etch (BOE) -----(10min or until hydrophobic)
- Rinse DI water-----(1min), dry with N2
- Remove Blue Dicing tape
- Bond wafer to dummy wafer by painting PR around edges
- Soft Bake -----(90degC)-----(30min)
- Matrix de-scum-------(13sec)

- Quick Buffered Oxide Etch (BOE) -----(30 sec)
- Rinse DI water-----(1min), dry with N2
- STS etch [plasma]-----(3cycles = 5microns)
- Soak in acetone to release the two wafers

3. Channel and Plenum Etch [top of wafer]

- 300T Stripper -----(80 degC)-----(20min)
- Put Blue Dicing tape on Cavity side
- Buffered Oxide Etch (BOE) of the channel side -----(10min)
- Rinse DI water-----(1min), dry with N2
- Remove Blue Dicing tape
- AMDM clean
- H2SO4 +H2O2 (2:1) Piranha Clean-----(10min)
- Dehydration bake –(30min)—(120deg)
- HMDS run-----(4.5)min
- Put Blue Dicing tape on Cavity side
- Apply Photoresist [1045PR let it set for a minute before spinning]-----(800-400rpm)-----(30sec)
- Soft Bake[in Convection Oven]-----(90degC)-----(30min)
- Tape Off undesired Channels and Plenums
- Align to Clearance Mask and Cavity Mask, then Expose Channel Mask [dark field mask] -----(6 - 10sec exposures)
- Developer(400K): water -----(1:2)-----(2min)
- Rinse DI water-----(1min), dry with N2

- Remove Blue Dicing tape
- Patch edges, holes, and round the plenum corners with Photoresist (1045)
- Soft Bake on hot plate starting at 50degC to 90degC in increments of 10deg for 10min per increment
- Matrix de-scum-----------(10sec)
- STS etch [plasma]-----(400microns)-----(160min)
- Perform O2 clean on STS prier to use
- rotate 90 deg every 75 cycles for even etch across the wafer
- When it breaks through the plenums
- Backing wafer
- AMDM clean
- HMDS run-----(4.5)min
- Apply strips of blue tape for plenum breathing holes.
- Apply Photoresist [1045PR]-----(1000-500rpm)-----(30sec)
- Press wafers together firmly
- Set in 40degC condition for 2-3 days
- Continue STS cycles in small increments until cavities break through
- Continues STS cycles with painting cavities that have reached tolerance in between cycles
- Soak in acetone to release the two wafers may take up to 2 days but if done properly will release with no effort.
- 300T Stripper -----(80 degC)-----(20min)

II. 4” Glass Preparation:

Starting with 4” Pyrex 7740 500micron thick, double sided polished.

1. Aluminum deposition for Heaters
   - H_2SO_4 +H_2O_2 (2:1) Piranha Clean-----(5min)
   - Replace with AMDM clean
   - Caution (Thermal Shock)
   - Rinse DI water -----(10min) and dry with N_2
   - Dehydration oven-----(120degC)-----(30min)
   - E-beam Machine-----(2micron)-----aluminum
   - AMDM clean
   - HMDS run-----(10)min
   - Apply Photoresist(5214) -----(3000rpm)-----(30sec)
   - Soft Bake-----(90degC)-----(30min)
   - Expose Heater Mask [light field mask] -----(6sec)
   - Developer(400K) : water -----(1:2)-----(30sec)
   - Rinse DI water-----(1min), dry with N_2
   - Flood expose entire specimen-----(10sec)
   - Bake-----(120degC)-----(20min)
   - Matrix de-scum-----------(10sec)
   - Phosphoric Aluminum Etch (PAE)-----(~35min)
   - Strip Photoresist with matrix run
2. Cut 5mm (200mil)off two opposing sides with diamond saw for access to Si during bonding

III. 5” Glass Preparation:

Starting with 5” Pyrex 7740 500micron thick, double sided polished.

1. Aluminum Deposition for Temperature Sensors

- AMDM clean
- H_2SO_4 +H_2O_2 (2:1) Piranha Clean-----(5min)
- Caution (Thermal Shock)
- Rinse DI water -----(5min) and dry with N_2
- Dehydration oven-----(120degC)-----(30min)
- Apply Photoresist(2035)-----(3000rpm)-----(30sec)
- Bake(hot plate with clean backing wafer)-----(110degC)-----(1min)
- Flood Expose Temp Sensor Mask [light field mask] -----(12sec)
- Bake(hot plate with clean backing wafer)-----(110degC)-----(1min)
- Developer(300MIF)-----(2min,15sec)
- Rinse DI water-----(1min), dry with N_2
- E-beam Machine-----(.4micron)-----aluminum
- Lift off process using 300T Stripper (80degC)-----(4-5 hours)
- AMDM clean
- Paint pattern with photoresist
- Soft Bake----(90degC)---(30min)
- Phosphoric Aluminum Etch (PAE)-----(~20min)
- Rinse DI water -----(5min) and dry with N_2

2. Have holes drilled for inlet and outlet Plenum

- AM clean both the specimen and a glass base

- glue together using photoresist
- Soft Bake-----(90degC)-----(30min)
- Drill 3/8” holes
- Soak in acetone to release the two

IV. Anodic Bonding:

1. Cleaning Silicon:

- BOE[Total Wafer]-------(10min)
- AZ300T Stripper ------(80deg)-----(30min)
- Particle pick
- BOE-------(2-3min)
- DI Rinse (leave in water until next step)------(2min)
- 511 Etch------(50deg)-----(1min)
- Acetone/Methanol/Propanol clean
- Matrix on backing wafer each side---------(1min)

2. Cleaning Glass

- AZ300T stripper ------(80deg)-----(30min)
- Particle pick
- Acetone/Methanol/Propanol clean
- Matrix on backing wafer ---------(1min)

3. Aligning the three pieces

- 4” glass wafer faces down with the aluminum heaters on the bottom.
- Si is aligned to this with the cavities on the bottom

- 5” glass wafer faces down with the aluminum leads on the bottom and is laid directly on the Si wafer.
- Use dental glue activated by UV light to achieve adhesion between Si and glass.

4. Bonding

- Aluminum foil wrapped over ceramic tile for bottom contact
- Aluminum weight used for top contact
- Place 5” wafer down first as to have access to the Si.
- Place probes on Si and attach contacts for top and bottom glass
- Heat-----(400degC)-----(600-700V)
- V Saw the Specimen in two:

APPENDIX C

CAVITY MOUTH SIZE MEASURMENTS

The cavity mouth sizes were each measured during the fabrication process to ensure repeatability between test sections. The following is the actual measurements in microns (µm) for each test section and a computed mean, maximum, minimum, and standard deviation. The spatial orientation of these tables is the same as Figure 71.

Left Side Top---------->Bottom

Channel #							Single Channel
1	**19.2**	**18.24**	**18.24**	**18.24**	**21.1**	**19.2**	

Channel #							Multi Channel	
1	**20.1**	**21.6**	**21.6**	**23.5**	**22**	**22**		
2	**22.1**	**24**	**19.2**	**20.1**	**17.3**	**19.2**		
3	**21.6**	**23**	**22.5**	**24**	**24**	**21.6**		
4	**19.68**	**19.2**	**18.2**	**24**	**19.2**	**19.7**		
5	**17.7**	**19.2**	**21.2**	**20.6**	**18.2**	**17.3**		
6	**18.24**	**19.2**	**20.1**	**19.6**	**19.7**	**17.2**		
7	**17.2**	**19.2**	**17.6**	**19.2**	**17.3**	**19.2**		
8	**17.7**	**18.72**	**17.7**	**18.7**	**18.2**	**17.2**		
9	**19.2**	**17.2**	**18.2**	**22.5**	**21.6**	**17.7**		
10	**17.7**	**18.2**	**17.2**	**20.1**	**18.7**	**17.2**		
11	**16.3**	**20.6**	**19.2**	**20.1**	**17.7**	**17.2**		
12	**20.6**	**18.7**	**19.2**	**17.7**	**18.7**	**19.2**		
13	**17.7**	**19.6**	**18.7**	**20.1**	**19.2**	**17.2**		
14	**17.7**	**19.6**	**18.7**	**19.7**	**20.1**	**19.2**		
15	**19.2**	**20.6**	**20.1**	**22.5**	**23**	**19.6**	Max	25.4
16	**20.6**	**20.6**	**24.5**	**24.9**	**23**	**25.4**	Min	16.3
17	**20.1**	**23**	**19.2**	**19.2**	**19.2**	**20.6**	Mean	20.00633
18	**24**	**19.7**	**22.5**	**23.5**	**24.5**	**24**	Count	120
19	**19.6**	**19.6**	**24**	**21.6**	**22**	**22.5**	STDEV	2.123924

Right Side

Table 11: Cavity measurements for test section 400-6

Left Side Top---------->Bottom

Channel #							Single Channel
1	**19.2**	**25.5**					

Channel #							Multi Channel	
1	**19.2**	**17.6**						
2	**19.6**	**21.1**						
3	**22.5**	**21.1**						
4	**18.2**	**19.6**						
5	**20.6**	**18.2**						
6	**20.1**	**20.6**						
7	**20.1**	**18.7**						
8	**17.7**	**19.2**						
9	**18.7**	**20.6**						
10	**18.2**	**19.2**						
11	**19.2**	**19.6**						
12	**20.6**	**18.2**						
13	**18.7**	**17.2**						
14	**17.2**	**19.6**						
15	**23**	**21.6**					Max	25.5
16	**20.1**	**19.6**					Min	17.2
17	**17.2**	**17.7**					Mean	19.64
18	**20.6**	**21.6**					Count	40
19	**19.2**	**19.2**					STDEV	1.679702

Right Side

Table 12: Cavity measurements for test section 400-2

Left Side Top---------->Bottom

Single Channel

Channel #						
1	**20.6**	**18.2**	**18.2**		**19.6**	**19.6**

Multi Channel

Channel #						
1	**21.6**	**17.7**	**21.6**	**22.5**	**21.6**	**20.1**
2	**19.6**	**19.2**	**19.6**	**18.2**	**19.2**	**19.6**
3	**18.7**	**21.1**	**19.6**	**19.6**	**17.2**	**18.2**
4	**17.2**	**24**	**21.6**	**18.7**	**21.6**	**22.1**
5	**19.6**	**21.1**	**18.2**	**21.6**	**19.6**	**19.2**
6	**21.1**	**19.6**	**19.2**	**19.6**	**20.1**	**18.2**
7	**20.6**	**19.2**	**20.1**	**20.1**	**19.6**	**21.6**
8	**20.6**	**19.6**	**21.6**	**21.1**	**21.6**	**20.1**
9	**22.1**	**20.6**	**21.1**	**19.2**	**20.1**	**21.1**
10	**18.7**	**24**	**21.6**	**20.1**	**17.7**	**18.7**
11	**17.2**	**21.1**	**22.5**	**20.1**	**21.1**	**21.1**
12	**20.1**	**17.7**	**21.1**	**22.1**	**19.2**	**18.2**
13	**19.2**	**20.1**	**24**	**21.1**	**19.2**	**18.7**
14	**18.2**	**21.6**	**17.2**	**24**	**20.6**	**20.6**
15	**19.6**	**18.2**	**24**	**19.2**	**18.7**	**19.6**
16	**19.2**	**19.2**	**20.6**	**20.6**	**25.9**	**18.7**
17	**23**	**21.6**	**26.4**	**24**	**25.4**	
18	**21.6**	**17.7**	**19.2**	**19.2**	**28.8**	**10**
19	**28.3**	**24**	**17.7**	**17.2**	**24**	**19.2**

Max	28.8
Min	10
Mean	20.34746
Count	118
STDEV	2.379208

Right Side

Table 13: Cavity measurements for test section 200-6

Left Side Top---------->Bottom

Single Channel

Channel #						
1	**20.6**	**20.6**				

Multi Channel

Channel #						
1	**20.6**	**22.5**				
2	**20.6**	**17.7**				
3	**19.2**	**18.7**				
4	**22.1**	**20.6**				
5	**17.2**	**18.2**				
6	**17.2**	**21.6**				
7	**21.1**	**21.6**				
8	**21.1**	**21.1**				
9	**22.1**	**17.7**				
10	**22.5**	**19.2**				
11	**18.7**	**22.1**				
12	**19.6**	**22.1**				
13	**19.6**	**19.6**				
14	**17.2**	**21.6**				
15	**18.7**	**17.7**				
16	**22.5**	**20.6**				
17	**22.5**	**17.7**				
18	**19.6**	**19.6**				
19	**22.1**	**21.6**				

Max	22.5
Min	17.2
Mean	20.1725
Count	40
STDEV	1.709969

Right Side

Table 14: Cavity measurements for test section 200-2

APPENDIX D

UNCERTAINTY OF MEASUREMENTS

- Current measurements for heaters
  - HP Multimeter 34401A specifications, based on the ranges of use.
    - Range ~ 1amp
    - $U_I = \pm 1.1 mA$
- Voltage measurement for heaters
  - National Instruments DAQ board specifications, based on the ranges of use.
    - Range ~ 10V
    - $U_{V-DAQ} = \pm 4.303 mV$
  - A set of LT1990 Op-amps were used to condition the voltage before entering the DAQ system. Based on the ranges of use and the Op-amp specifications.
    - Range ~10V
    - $U_{V-Op} = \pm 60.0 mV$

- Total heater voltage uncertainty is presented as follows.
    - $U_{V-total} = \sqrt{U_{V-DAQ}{}^2 + U_{V-Op}{}^2}$
        - $U_{V-total} = \pm 60.154 mV$
- Total uncertainty of the input power that is calculated by ($P_{in} = VI$) is as follows.
    - The uncertainty for a single resistors power input is given by the following equation.
    - $U_{P/resistor} = \sqrt{\left(\frac{\partial P}{\partial V} U_{V-total}\right)^2 + \left(\frac{\partial P}{\partial I} U_{V-Op}\right)^2}$
        - Current Range ~ 1amp
        - Voltage Range ~ 10V
        - $U_{P/resistor} = \pm 0.061151 W$
    - The uncertainty of all the heaters in series is as follows
    - $U_{P-total} = \sqrt{7(U_{P/resistor})^2}$
        - 7 heaters in series
        - $U_{P-total} = \pm 0.16179 W$ or 0.404% of full scale.
- The Uncertainties of the thermocouples are gathered by curve fitting their data against a calibrated thermistor and finding the uncertainty of the data about the curve fit. This procedure was performed while the thermoucouples were connected to the DAQ system which combines the uncertainties of the DAQ system and the thermocouples.

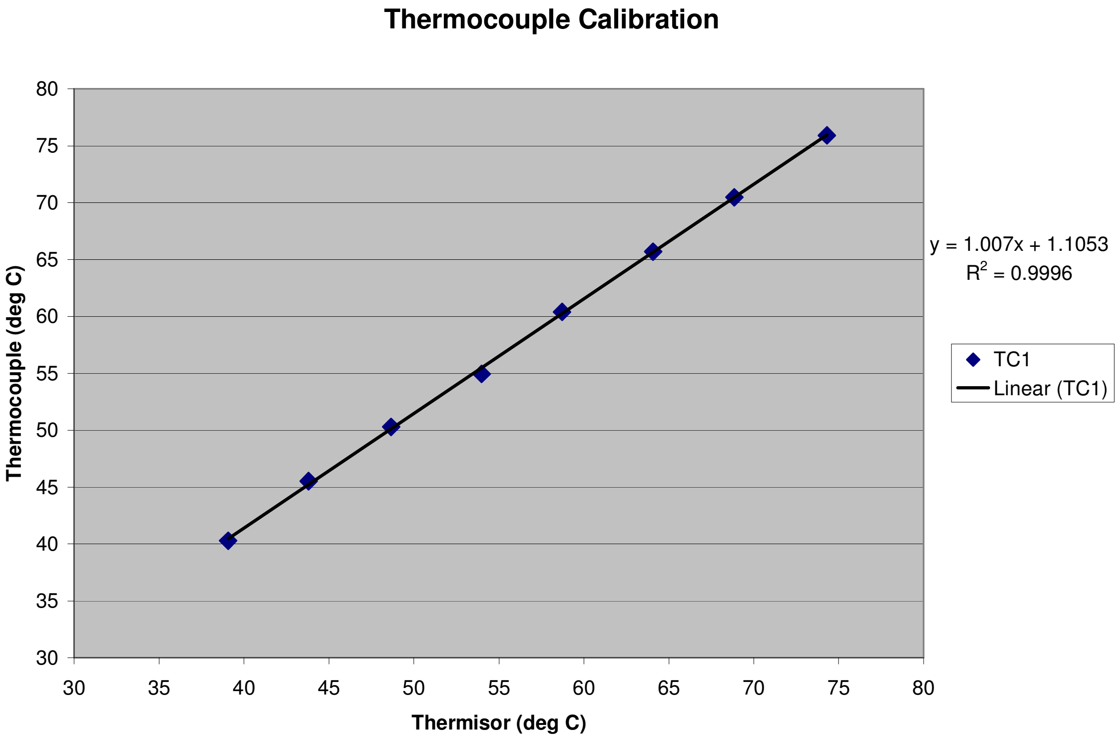

Figure 92: Calibration curve for the inlet thermocouple.

- The equations needed for this procedure are as follows
  - Linear Fit from plot: $Y(x_i) = mx_i + b$
  - Variance: $S^2 = \sum_{i-1}^{n} (y_i - y(x_i))^2$
  - Standard Deviation: $S_{x/y} = \sqrt{\frac{S^2}{n-2}}$
  - Uncertainty: $U = t(\alpha / \nu) \cdot S_{x/y}$
- The level of confidence (α) is held at 95%, (n) is the number of data points, the value of (ν) is the number of data points (n) minus 2, and

$t(\alpha/\nu)$ is attained from the student-t distribution chart out of Figliola and Beasley [2000].

- This analysis gave the following maximum uncertainty for the inlet and outlet thermocouples.
    - $U_{thermocouple} = \pm 0.655^{o} C$

- The uncertainties of the pressure sensors are gathered by curve fitting their data against a dead weight tester and finding the uncertainty of the data about the curve fit. This procedure, unlike that of the thermocouples, was not attached to the DAQ system during the calibration. Therefore the uncertainties of the DAQ will have to be factored in.

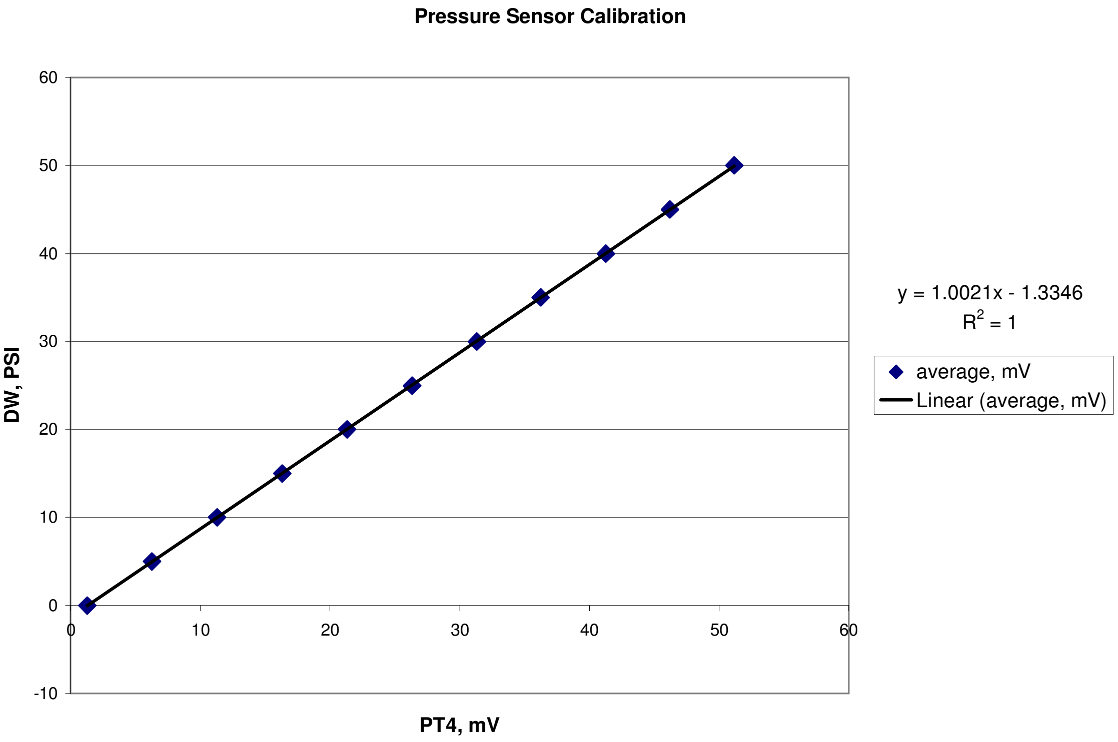

Figure 93: Calibration curve for the inlet Pressure sensor.

  - The equations needed for this portion of the procedure are exactly the same as those used for the thermocouple analysis.
  - This portion of the uncertainty is given in mili-Volts as seen below.
    - $U_{V-pressure} = \pm 0.0914mV$
  - National Instruments DAQ board specifications, based on the ranges of use.
    - Range ~ 100mV
    - $U_{V-DAQ} = \pm 0.326mV$
  - The total voltage uncertainty of the pressure sensors are given as follows.
    - $U_{V-total-pressure} = \sqrt{U_{V-DAQ}{}^2 + U_{V-\Pr essure}{}^2}$
    - $U_{V-total-pressure} = \pm 0.3385mV$
    - For the given sensors, 1mV=6.894KPa, and a maximum range of 689.4KPa. Therefore the uncertainty in KPa is as follows
    - $U_{pressure} = \pm 2.334KPa$ or 0.339% of full scale.
- The Micropump Gear Pump used was calibrated for flow rate purposes based on the calibration directions by its manual. Due to the pump curve for this particular model being flat, the flow was calibrated under atmospheric conditions. After calibration of the pump a few test runs were performed to check its values and these are displayed as follows.

	Digital Read Out (ml/min)	Graduated Cylinder(ml/min)	%Error
1	50	49.75	-0.50
2	50	49.65	-0.75
3	100	101.5	1.47
4	100	101.25	1.23
5	200	202.5	1.23
6	200	202	0.99
		Maximum % Error	**1.47**

Table 15: Percent Errors evaluated at different Flow rates.

- The Uncertainties of the in-channel sensors are gathered by curve fitting their data against the average of the calibrated inlet and outlet thermocouples and finding the uncertainty of the data about the curve fit. This procedure was performed while the in-channel sensors were connected to the DAQ system which combines the uncertainties of the DAQ system in with the fit.

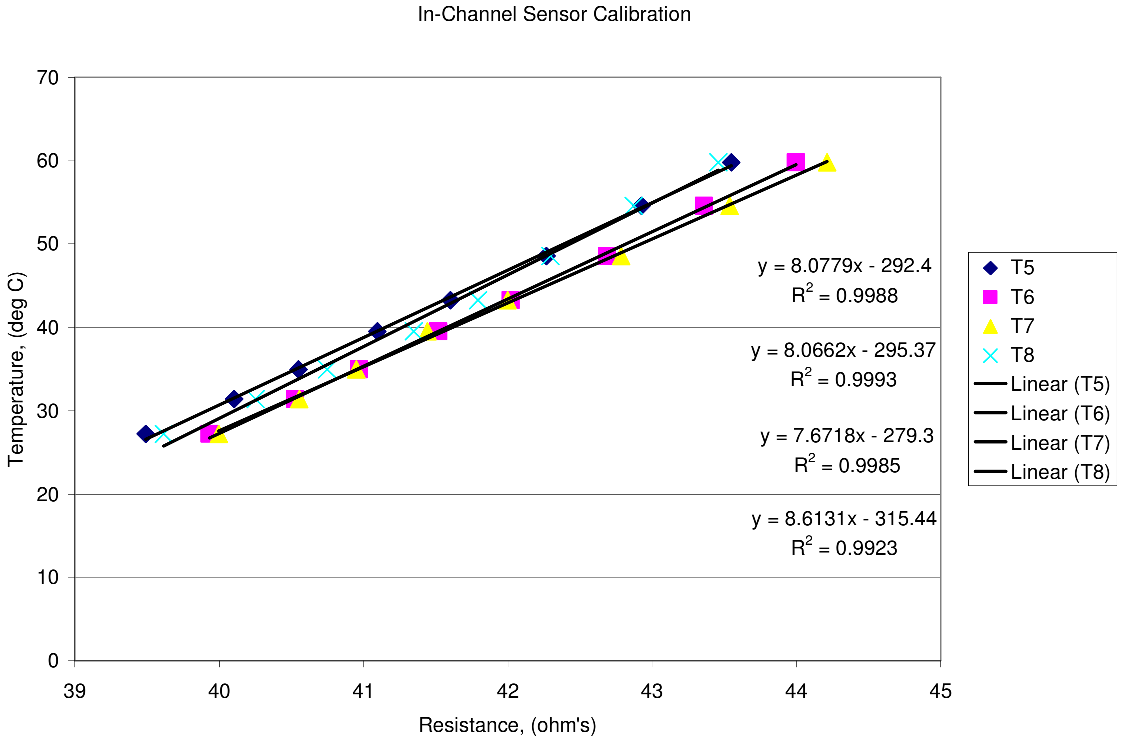

Figure 94: Calibration curves for the in-channel temperature sensors.

- The equations needed for this portion of the procedure are exactly the same as those used for the thermocouple analysis. The uncertainties of the sensors T5-T8 which are discussed in this thesis are presented below.

Sensor	Uncertainty (deg C)
T5	1.03
T6	0.81
T7	1.15
T8	2.63

Table 16: Uncertainty for in-channel sensors T5-T8 for the 200-2 test section.